LOW TEMPERATURE PHYSICS VOLUME 26, NUMBER 4 APRIL 2000

QUANTUM LIQUIDS AND QUANTUM CRYSTALS

The role of normal processes in the thermal conductivity of solid deuterium

O. A. Korolyuk,* B. Ya. Gorodilov, A. I. Krivchikov, and V. V. Dudkin

B. I. Verkin Physicotechnical Institute for Low Temperature Physics, National Academy of Sciences of Ukraine, Lenin prospect, 47, 61164 Kharkov, Ukraine

(Submitted October 18, 1999; revised November 19, 1999)
Fiz. Nizk. Temp. **26**, 323–329 (April 2000)

The thermal conductivity of orthodeuterium crystals containing a neon impurity is investigated in the temperature interval 1.8–17 K. The results of the measurements are described in the framework of the relaxation-time model with allowance for phonon–phonon scattering processes. The intensity of the normal scattering processes for deuterium are determined. The existing theoretical models are used to estimate the intensity of the phonon scattering processes for a number of cryocrystals. The calculated intensity of the normal processes is compared to the experimental result. © *2000 American Institute of Physics.* [S1063-777X(00)00104-3]

INTRODUCTION

It is known that phonon–phonon scattering processes which conserve quasimomentum (normal or N processes) do not contribute to the thermal resistance of a crystal.[1] At the same time, in certain cases they can play a significant role in the formation of the thermal resistance. The pioneering works in the field of research on the influence of N processes on the thermal conductivity in the relaxation-time approximation were the studies by Guyer and Krumhansl[2] and Callaway.[3] The Callaway model has proved to be more convenient to use and is now widely employed. Although it was originally proposed in a rather crude approximation, more recent studies (in particular, Refs. 4 and 5) have shown that the model is also applicable to a more accurate analysis of this question.

In redistributing the energy of the phonon subsystem, N processes, depending on their intensity, give rise to unusual effects in the thermal conductivity of crystals, especially when their intensity is comparable to that of the resistive processes. Then the influence of N processes on the value and behavior of the thermal conductivity becomes more appreciable, so that one can determine their intensity quite reliably from data on the thermal conductivity[5] and from experiments on second sound.

Up until now the determination of the intensity of N processes from heat conduction experiments has been done only for the cryocrystals ^{3}He, ^{4}He (Refs. 6–8), p-H_2 (Refs. 5 and 9), and Ne (Ref. 10).

In this paper we investigate the influence of normal phonon–phonon processes on the thermal conductivity of solid orthodeuterium containing a neon impurity.

EXPERIMENT

We measured the thermal conductivity of pure o-D_2 and two samples of o-D_2 containing a Ne impurity of $c=0.05\%$ in the temperature interval 1.8–17 K by a steady-state two-dimensional method. The crystals were grown in a stainless steel ampoule with an inner diameter of 4.6 mm and a length of 38 mm.[11]

In the experiment we used gaseous deuterium with a 99.59% isotopic impurity. The concentration of chemical impurities in the dry gas was less than 0.01%. Prior to preparation of the sample an ortho-to-para conversion of the deuterium was carried out by contact with an $Fe(OH)_3$ catalyst at a temperature close to 20 K. As a result, the p-D_2 concentration reached $c=2\%$. The chemical purity of the Ne (of natural isotopic composition) was 99.99%. The gaseous mixture of orthodeuterium and neon was prepared in a glass vessel at room temperature. The relative error in the determination of the neon concentration in the mixture was not over 5%.

To ensure a uniform distribution of the neon impurity in the sample the latter was crystallized from the gas phase, with the gas pressure held constant at a value corresponding to the vapor pressure of deuterium near the triple point (17 kPa).

The pure sample 1 and the doped sample 3 were grown at a rate of 0.13 mm/min, annealed for 3 h, and then cooled to the temperature of the measurements. The rate of cooling was chosen so that the gradient over the sample did not exceed 0.3 K. The procedure used to prepare samples 1 and 3 made it possible to obtain reproducible results on the temperature dependence and values of the thermal conductivity. The other doped sample 2 was grown at a rate of 0.26 mm/min.

The curves of the temperature dependence of the thermal conductivities of the samples studied are shown in Fig. 1. After the measurements, sample 3 was remelted, and it was found that its thermal conductivity was completely the same before and after the melting.

NORMAL PROCESSES AND THERMAL CONDUCTIVITY

Let us consider the physical model that will be used to analyze the experimental data.

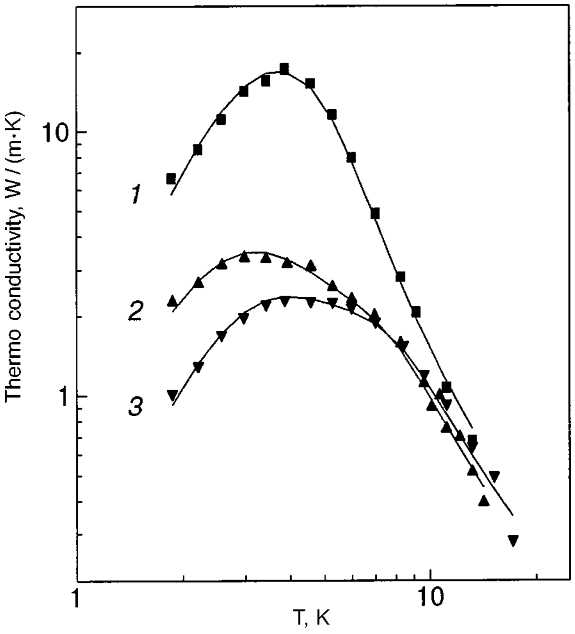

FIG. 1. Temperature dependence of the thermal conductivity of samples of o-D_2 without a Ne impurity (*1*), of o-D_2+0.0502% Ne (*2*), and of o-D_2 +0.048% Ne (*3*). Samples 1 and 3 (curves *1*,*3*) were grown at a rate of 0.13 mm/min and annealed, sample 2 (curve *2*) was grown at 0.26 mm/min without annealing. The solid curves correspond to a calculation by the Callaway formula.[3]

Normal phonon–phonon interaction processes have been examined most thoroughly by Herring,[12] according to whom the relaxation rate of N processes for acoustical phonons in the low-temperature region can be represented in the form

$$\tau_N^{-1} \propto \omega^n T^{5-n},$$

where $n=2$ for crystals of high symmetry (cubic and hcp).

In the most recent papers (e.g., Ref. 4) the relaxation times for phonons with longitudinal and transverse polarization in various types of scattering processes ($l \leftrightarrow l+t$, $l \leftrightarrow t+t$, etc.) have been refined, and their frequency dependence and temperature dependence have been obtained.

Since the thermal conductivity experiments have only been able to establish the value of τ_N averaged over the phonon polarizations, in the study of normal processes the difference between the longitudinal and transverse phonons is usually neglected. In what follows we shall use the standard expression for the relaxation rate of N processes:

$$\tau_N^{-1} = B_N \omega^2 T^3. \tag{1}$$

In Ref. 5, in an analysis of the results on the thermal conductivity of neon in parahydrogen, the term corresponding to the scattering of phonons with transverse polarization ($\tau_N^{-1} \sim \omega T^4$) was taken into account, but it was shown in Ref. 9 that for hydrogen with a neon and argon impurity the contribution of this term is several orders of magnitude smaller.

The Callaway model[3] takes into account the influence of normal phonon–phonon scattering processes in the approximation of a Debye phonon spectrum, and the thermal conductivity of the crystal was written in the form of two terms:

$$K(T) = G T^3 (I_1 + I_2^2 / I_3), \tag{2}$$

where

$$I_1 = \int_0^{\Theta/T} \tau_C f(x)\,dx; \quad I_2 = \int_0^{\Theta/T} \frac{\tau_C}{\tau_N} f(x)\,dx;$$

$$I_3 = \int_0^{\Theta/T} \frac{\tau_C}{\tau_N \tau_R} f(x)\,dx; \quad G = k^4/(2/\pi^2 s \hbar^3);$$

$$f(x) = x^4 e^x/(e^x - 1)^2; \quad x = \hbar\omega/kT;$$

Θ is the Debye temperature, k is Boltzmann's constant, s is the speed of sound, τ_R, τ_N, and τ_C are, respectively, the relaxation times of resistive scattering processes and of N processes and the combined relaxation time

$$\tau_C^{-1} = \tau_R^{-1} + \tau_N^{-1}.$$

For normal processes we obtain, after introducing the variable x defined above,

$$\tau_N^{-1} = A_N x^2 T^5. \tag{3}$$

In the analysis of the experimental data we took into account the following resistive processes: umklapp (U) processes, and the scattering of phonons on grain boundaries and impurities:

$$\tau_R^{-1} = \tau_U^{-1} + \tau_B^{-1} + \tau_I^{-1}. \tag{4}$$

The U processes are determined by the properties of the deuterium crystal and at low concentrations are practically independent of the presence of impurity molecules:[1]

$$\tau_U^{-1} = A_U x^2 T^3 \exp(-E/T),$$

where E is the phonon threshold energy above which umklapp processes can arise.

Scattering on grain boundaries is determined by the characteristic mean free path L of the phonons and the sound velocity s:[1]

$$\tau_B^{-1} = s/L.$$

The inverse relaxation time for the scattering of phonons by a heavy isotopic impurity has a resonant character and is given by the expression[5]

$$\tau_I^{-1} = \frac{1.5\pi c \varepsilon^2 \omega (\omega/\omega_D)^3}{(1-\omega^2/\omega_0^2)^2 + 2.25\pi^2 \varepsilon^2 (\omega/\omega_D)^6},$$

where c is the impurity concentration, $\varepsilon = \Delta M/M$ (the mass defect), ΔM is the mass difference of the impurity and host molecules, ω_D is the Debye frequency, ω_0 is the quasilocal frequency, which in the Debye approximation is $\omega_0 = \omega_D/(3\varepsilon)^{1/2}$.

Besides the purely mass-related effect, the incorporation of an impurity in a crystal also alters the interaction force and causes a distortion of the lattice around the impurity center. In addition to the mass defect, Clemens[13] introduced an effective parameter taking into account the local change in the force constants $\Delta\varphi/\varphi$ and the local lattice distortion $\Delta\delta/\delta$, which has the following form:

$$\Gamma = \varepsilon^2 + 2(\Delta\varphi/\varphi - 6.4\gamma\Delta\delta/\delta)^2, \tag{5}$$

where γ is the Grüneisen constant.

For the case of neon in deuterium the lattice distortion can be estimated as $\Delta\delta/\delta \approx (V_{D_2} - V_{Ne})/3V_{D_2} \approx 0.098$, since the molar volumes of deuterium and neon are V_{D_2}

$=19.91\,\mathrm{cm}^3$/mole and $V_{\mathrm{Ne}}=14.07\,\mathrm{cm}^3$/mole, respectively. The first term in parentheses in Eq. (5) is small compared to the second and will be neglected. We emphasize that this is a crude model approximation. However, there is reason to think that this approximation is valid at low temperatures. If one takes $\gamma\approx 2$,[14] the correction to ε^2 due to local variation of the force constants and the lattice distortion will be approximately equal to 3.1, if it is assumed that the interaction potentials of the neon and deuterium are practically equal. Thus the correction under discussion is smaller than the mass defect $\varepsilon^2=16$. In our analysis of the results we shall neglect the contribution due to the lattice distortion.

DISCUSSION

The results for pure o-D_2 agree with the data of Ref. 15. There is complete agreement as to the temperature position of the maximum of the thermal conductivity, although the value of the thermal conductivity obtained in the present study is somewhat lower. This is probably due to the fact that the crystals in Ref. 15 were grown in a glass cell having a larger diameter, which made for a higher quality of the crystals. This is also indicated by the size of the crystalline grains (1 mm) in Ref. 15.

The low-temperature thermal conductivities of crystals containing a neon impurity differ significantly (Fig. 1). For $T<6$ K the thermal conductivity of the sample grown at the lower rate (curve *3*) is lower than that of the sample grown at the faster rate (curve *2*). In the region $T\gtrsim 10$ K the curves have different slopes, and they intersect. These features are clearly related to the defect structure of the crystals grown under different conditions. The influence of the sample preparation procedures on the defect structure will not be discussed in this paper.

The experimental temperature dependences of the thermal conductivity were described by the Callaway formula. A value of 111.5 K[16] was used for the Debye temperature of deuterium in the calculations. The agreement between the theory and experiment, both for pure orthodeuterium and for a deuterium–neon mixture, can be improved somewhat by taking into account the contribution of relaxation on isotopic impurities contained in the initial deuterium gas ($\tau^{-1}=Dx^4T^4$ with $D=299.5\,\mathrm{s}^{-1}\mathrm{K}^{-4}$). This is not surprising, since the concentration of isotopic impurities in the initial gas was 0.041% and, in addition, around 2% of the molecules in the crystal had nonzero angular momentum. The argument of the exponential function for phonon–phonon U processes ($E=37.1$ K) was also obtained from the data for pure orthodeuterium. The intensity of normal processes (A_N) was determined by fitting the data for crystals containing impurities, which yielded a value $(5.0\pm0.5)\times10^4\,\mathrm{s}^{-1}\mathrm{K}^{-5}$.

TABLE I. Parameters of the phonon scattering processes as obtained from a fitting of the Callaway formula to the experimental temperature dependences of the thermal conductivity for the different samples: U processes (A_U,E), N processes (A_N), and scattering on grain boundaries (L_B is the phonon mean free path). In the calculations a value $s=1202.8$ m/s (Ref. 17) was used for the speed of sound in deuterium.

Sample No.	c_{Ne}, 10^{-4}	L_B, 10^{-5} m	A_U, $10^7\,\mathrm{s}^{-1}\,\mathrm{K}^{-3}$	E, K	A_N, $10^4\,s^{-1}\,\mathrm{K}^{-5}$
1	0	3.76	4.56	37.1	5.0±0.5
2	5.02	1.88	6.89	37.1	5.0±0.5
3	4.8	0.66	5.73	37.1	5.0±0.5

The values obtained for the parameters of the scattering processes are listed in Table I. The results of the fitting are shown by the solid curves in Fig. 1. The mean free path for the scattering of phonons by grain boundaries was about 3.5 times larger for crystal 2, which was grown at the higher rate, than for the other doped crystal 3. As we see from Fig. 1, the experimental points for curve *3* are systematically higher than for curve *2* in the region $T>10$ K, where one would expect the results to agree. The difference is apparently due to the defect structure of the crystals and, as a result, the different predominant orientation of the crystal with respect to the heat flux.[11]

Figure 2 shows the calculated change in the behavior of the thermal conductivity as a function of the intensity of the normal processes. The middle curve is the result of a fitting for sample 2. For the other two curves the intensity of the normal processes was changed by 3 orders of magnitude (decreased for curve *1* and increased for curve *3*). The contributions to the thermal conductivity from the terms in the Callaway formula (1) vary as a function of the intensity. For example, for curve *1* the thermal conductivity is determined exclusively by the first term, while for curve *3* it is determined by the second (the so-called ''Ziman limit'').

The data accumulated in recent years permits one to compare the intensities of N processes in quantum crystals and neon as inferred from measurements of the thermal conductivity. For a numerical estimate we used the ideas set forth in Refs. 4 and 5. In the general case the relaxation rate of N processes can be written as

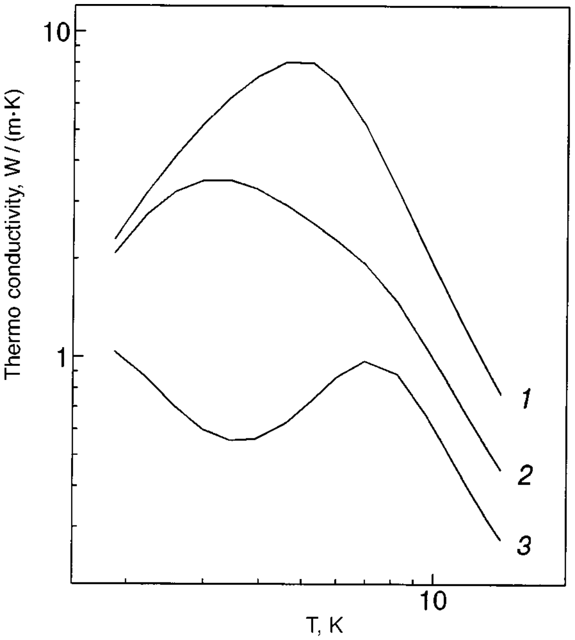

FIG. 2. Calculated temperature dependence of the thermal conductivity of orthodeuterium at various intensities of the normal processes, A_N, $\mathrm{s}^{-1}\mathrm{K}^{-5}$: 50 (*1*), 5×10^4 (*2*), 5×10^7 (*3*) (the parameters of the other scattering processes remained unchanged; see Table I). The calculation was done using the Callaway formula.

$$\tau_N^{-1}=b\left(\frac{\omega}{\omega_D}\right)^n\left(\frac{T}{\theta}\right)^{5-n}, \tag{6}$$

$$b\cong\frac{16\pi^3}{735\sqrt{3}}\frac{\gamma^2a^3\hbar}{M}\left(\frac{k\Theta}{\hbar s_t}\right)^5,$$

where a is the distance between nearest neighbors, and s_t is the transverse velocity of sound. After substituting expression (6) for the intensity of normal processes into expression (3) and expressing the coefficient in terms of the characteristic parameters of the crystal, we obtain

$$A_N\approx 991.6\hbar N_A^{5/3}\frac{\gamma^2}{\mu V^{2/3}\Theta^5}, \tag{7}$$

where μ is the molar mass, V is the molar volume, and N_A is Avogadro's number. It is seen from formula (7) that the intensity of normal processes depends on the physical parameters characterizing the specific substance. Table II shows a comparison of the intensities A_N of the normal processes obtained for different crystals from thermal conductivity experiments[6–10,18] and the values calculated using the above formula.

Let us now separate out the dependence on the Debye temperature in formula (7), eliminating the dependence on the molar weight, molar volume, and Grüneisen constant ($A_N\mu V^{2/3}/\gamma^2$), and compare the results with the analogous quantities obtained from experiments on the thermal conductivity of different crystals.[6–10,18] Figure 3 shows a logarithmic plot of this dependence. We see that the intensities of the N processes in different experiments, except for the results on HD,[18] agree with the calculated formula $\tau_N^{-1}\propto\Theta^{-5}$. The intensity of the N processes for HD is significantly lower than the value suggested by the estimating formula. The reason is that in Ref. 18 this parameter was determined from the low-temperature part (below the maximum) of the thermal conductivity curve, making it difficult to interpret the results reliably enough. For Ne the intensity of the N processes[10] is somewhat too high; this may be due to the different representation of the N processes in that paper ($\tau_N^{-1}\equiv B_Nx^2T^4$).

Making use of the fact that the calculated intensities of the N processes agree with those obtained from experiment, we calculated the parameters of the N processes for several very simple molecular crystals. The results of the calculations are presented in Table III. The calculated values for classical rare-gas crystals (see Table III) are only slightly different from the intensity of the N processes for isotopes of hydrogen (see Table II). It should be kept in mind that the influence of normal processes on the thermal conductivity depends on the relative intensities of the normal and resistive processes. The contribution of N processes is unimportant when the relaxation time of the N processes is significantly shorter than that of the resistive processes.

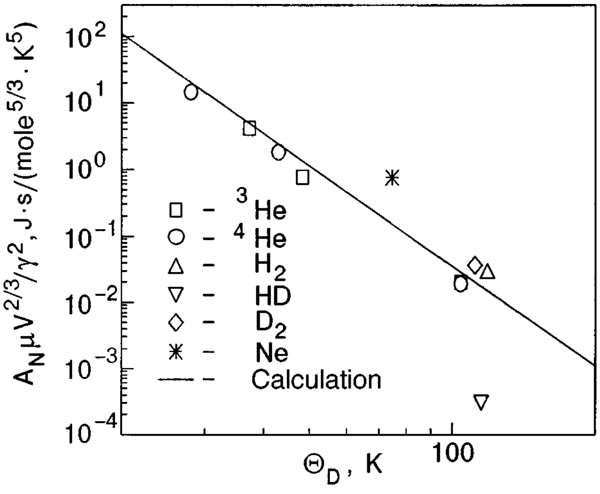

FIG. 3. Intensity of the N processes for various substances, normalized by the molecular weight, molar volume, and Grüneisen constant ($A_N\mu V^{2/3}/\gamma^2$), as a function of the Debye temperature. The symbols are the experimental results of Refs. 6–10, 18, and the present study (Table II); the line was calculated according to formula (7).

CONCLUSION

Because the parameters of the Lennard-Jones potential for neon are close to those for deuterium, one can treat a neon impurity in orthodeuterium as quasi-isotopic. Since, as a result of the large mass ratio ($M_{\mathrm{Ne}}/M_{\mathrm{D}_2}=5$) the scattering of phonons by the heavy isotopic impurity is predominant over the other scattering processes, the role of the normal processes is manifested quite clearly.

Let us state the main results:

TABLE II. Comparison of the calculated and experimentally obtained values of the intensity of normal phonon–phonon processes ($\tau_N^{-1}=A_Nx^2T^5$). The Debye temperature Θ and molar volume V for the isotopes of H_2 and Ne are taken from Refs. 16 and 14, respectively, and the Grüneisen parameters γ for He, the hydrogens, and Ne were calculated using the data of Refs. 19, 16, and 20, respectively.

				A_N, s^{-1} K^{-5}			
Substance	γ	V, cm^3/	Θ, K	Calculation	Experiment	$A_N\mu V^{2/3}/\gamma^2$ $\frac{\mathrm{J\cdot s}}{\mathrm{mole}^{5/3}\,\mathrm{K}^5}$	Source
^{3}He	2.70	19.5	37.3	2.09×10^7	1.37×10^7	4.080	Ref. 6
^{3}He	2.52	17.6	48.2	5.40×10^6	2.40×10^6	0.767	Ref. 6
^{3}He	2.03	12.6	104	9.36×10^4	5.10×10^4	0.0201	Ref. 6
^{4}He	2.79	20.4	28	6.80×10^7	3.81×10^7	14.6	Ref. 8
^{4}He	2.49	17.3	43	7.08×10^6	4.2×10^6	1.81	Ref. 8
^{4}He	1.94	11.65	104	6.76×10^4	3.49×10^4	0.0190	Ref. 8
H_2	2.00	23.16	118.5	4.73×10^4	6.7×10^4	0.0272	Ref. 9
HD	2.00	20.95	115	3.92×10^4	586	3.34×10^4	Ref. 18
D_2	2.00	19.91	111.5	3.55×10^4	5.0×10^4	0.0367	Present study
Ne	2.60	13.53	74.6	1.16×10^5	4.5×10^5(s^{-1} K^{-4})	0.756	Ref. 10

TABLE III. Intensities A_N of normal phonon–phonon interaction processes (calculation) for several substances ($\tau_N^{-1}=A_N x^2 T^5$). The values of the Debye temperature and molar volume were taken from Ref. 16 for the isotopes of H_2, from Ref. 21 for CH_4, and from Ref. 14 for Ar, Kr, and Xe, and the Grüneisen parameter was taken from Ref. 14 for H_2, from Ref. 22 for CH_4, and from Ref. 20 for Ar, Kr, and Xe.

Substance	γ	V, cm^3/mole	Θ, K	A_N, s^{-1} K^{-5}
HT	2	20.48	107	4.28×10^4
DT	2	19.34	106.8	3.59×10^4
T_2	2	18.82	102.2	3.8×10^4
CH_4	2	32.75	144	1.77×10^3
Ar	2.2	22.57	93.3	9.62×103
Kr	2.6	27.13	71.7	2.11×10^4
Xe	2.3	34.55	64	1.59×10^4

— We have analyzed the influence of N processes on the thermal conductivity of the investigated crystals and have for the first time determined the intensity of N processes in solid D_2.

— We have compared the published data on the intensity of N processes, obtained from the results of thermal conductivity measurements, for isotopes of helium, hydrogen, and neon.

— On the basis of the theory set forth in Refs. 4 and 5, we have calculated the intensities of N processes for crystals in which the corresponding values are known from experiments,[6–10,18] and we have made a comparison.

— We have used the formulas given here to estimate the intensities of N processes for several of the simplest cryocrystals.

We have shown that for all of the substances considered, including quantum crystals, the intensity of normal phonon–phonon processes at low temperatures can be described in a unified way in terms of the characteristic parameters of the crystals. The proposed approach creates the impression that the zero-point vibrations do not affect the intensity of the normal processes. It must be kept in mind, however, that all of the parameters appearing in the formula for the intensity of normal processes depend to some degree on the energy of the zero-point vibrations of the particles, and for this reason the dependence of the N processes on the quantum-mechanical characteristics of the crystal is not clear-cut.

In closing, the authors express their gratitude to T. N. Antsygina for kindly providing the formula for estimating the intensity of normal processes and for helpful consultations and to Prof. V. G. Manzheliĭ for interest in and support of this study and for a valuable discussion.

*E-mail: korolyuk@ilt.kharkov.ua

---

[1] R. Berman, *Thermal Conductivity in Solids*, Clarendon Press, Oxford (1976).

[2] R. A. Guyer and I. A. Krumhansl, Phys. Rev. **148**, 766, 778 (1966).

[3] J. Callaway, Phys. Rev. **122**, 787 (1961).

[4] T. N. Antsygina and V. A. Slyusarev, Fiz. Nizk. Temp. **19**, 494 (1993) [Low Temp. Phys. **19**, 348 (1993)].

[5] T. N. Antsygina, B. Ya. Gorodilov, N. N. Zholonko, A. I. Krivchikov, V. G. Manzheliĭ, and V. A. Slyusarev, Fiz. Nizk. Temp. **18**, 417 (1992) [Sov. J. Low Temp. Phys. **18**, 283 (1992)].

[6] R. Berman and C. R. Day, Phys. Lett. A **33**, 329 (1970).

[7] R. Berman, C. L. Bounds, and S. J. Rogers, Proc. R. Soc. London **289**, 66 (1965).

[8] R. Berman, C. L. Bounds, C. R. Day, and H. H. Sample, Phys. Lett. A **26**, 185 (1968).

[9] B. Ya. Gorodilov, A. I. Krivchikov, V. G. Manzheliĭ, and N. N. Zholonko, Fiz. Nizk. Temp. **20**, 78 (1994) [Low Temp. Phys. **20**, 66 (1994)].

[10] R. M. Kimber and S. J. Rogers, J. Phys. C **6**, 2279 (1973).

[11] O. A. Korolyuk, B. Ya. Gorodilov, A. I. Krivchikov, A. S. Pirogov, and V. V. Dudkin, J. Low Temp. Phys. **111**, 515 (1998).

[12] C. Herring, Phys. Rev. **95**, 954 (1954).

[13] G. P. Srivastava, *The Physics of Phonons*, Adam Hilger, Bristol/Philadelphia/New York (1990).

[14] V. G. Manzhelii and Yu. A. Freiman, *Physics of Cryocrystals* [in English], edited by M. L. Klein and A. A. Maradudin, AIP Press, Woodbury, New York (1996).

[15] B. Ya. Gorodilov, I. N. Krupskiĭ, V. G. Manzheliĭ, and O. A. Korolyuk, Fiz. Nizk. Temp. **7**, 424 (1981) [Sov. J. Low Temp. Phys. **7**, 208 (1981)].

[16] M. I. Bagatskiĭ, I. Ya. Minchina, V. G. Manzheliĭ, P. I. Muromtsev, A. I. Krivchikov, and V. S. Parbuzin, Fiz. Nizk. Temp. **16**, 1009 (1990) [Sov. J. Low Temp. Phys. **16**, 589 (1990)].

[17] *Properties of Condensed Phases of Hydrogen and Oxygen (Handbook)* [in Russian], Naukova Dumka, Kiev (1984).

[18] K. S. Dubey, J. Phys. Chem. Solids **39**, 699 (1978).

[19] W. R. Gardner, J. K. Hoffer, and N. E. Phillips, Phys. Rev. A **7**, 1029 (1973).

[20] M. L. Klein and J. A. Venables (eds.), *Rare Gas Solids II*, Academic Press, New York (1977).

[21] B. Ya. Gorodilov, V. V. Sumarokov, P. Stachowiak, and A. Jezowski, Phys. Rev. B **58**, 3089 (1998).

[22] A. M. Tolkachev, A. N. Aleksandrovskiĭ, and V. G. Manzheliĭ, Fiz. Nizk. Temp. **3**, 1340 (1977) [Sov. J. Low Temp. Phys. **3**, 647 (1977)].

Translated by Steve Torstveit

Properties and structure of fluid hydrogen near the line of crystallization

E. S. Yakub*

Odessa State Medical University, Valikhovskiĭ per. 2, 65026 Odessa, Ukraine

(Submitted November 10, 1999)
Fiz. Nizk. Temp. **26**, 330–339 (April 2000)

The thermodynamic properties and distribution functions of highly compressed molecular hydrogen are investigated in a nonempirical atom–atom approximation. Quantum corrections are introduced on the basis of the Feynman variational approach. The pressure, energy, compressibility, thermal expansion, heat capacity, and sound velocity are calculated by the Monte Carlo method at temperatures of 200–500 K and pressures up to 5 GPa. The results are compared with the available experimental data. It is shown that effects due to incompressibility of the molecules and quantum effects must be taken into account in calculating the contributions to the thermodynamic functions from inter- and intramolecular forces. The behavior of the properties of fluid hydrogen near the line of crystallization outside the investigated region is predicted, and an estimate is made for the jump in volume upon crystallization of hydrogen at $T=300\,\mathrm{K}$. © *2000 American Institute of Physics.* [S1063-777X(00)00204-8]

INTRODUCTION

The thermodynamic, transport, and structural properties of isotopes of hydrogen in the condensed phase have been under intensive investigation for many years. A rich body of experimental material in the cryogenic region has been accumulated.[1] At high pressures the most important experimental results have been obtained in the solid phase by the diamond anvil method.[2] In recent years there has also been substantial progress in the study of highly compressed fluid hydrogen in the high-temperature region, where a transition to a metallic state has been observed in dynamic experiments.[3] Fluid hydrogen at low temperatures remains much less investigated. The existing published data has yielded the equation of state for the fluid phase of normal hydrogen at temperatures up to 500 K and pressures up to 2 GPa.[4] As we see in Fig. 1, there is a significant gap between the region investigated experimentally by static methods and the region studied in dynamic experiments. At high pressures and moderate temperatures the fluid-phase region adjacent to the line of crystallization remains practically uninvestigated. Since it is quite difficult to do an experiment here, it is of particular urgency to undertake a theoretical prediction of the properties of highly compressed fluid hydrogen.[5] However, there is an extremely restricted choice of nonempirical methods of predicting the properties of such dense systems. Methods based on the direct quantum-mechanical computer simulation, e.g., the path-integral Monte Carlo (PIMC) method,[6] are very demanding of computational resources and have not yet attained the necessary accuracy. A simpler approach based on the atom–atom approximation[7] essentially uses classical mechanics and is not directly applicable to light molecules at relatively low temperatures.

The difficulties facing the theoretical prediction of the properties of highly compressed hydrogen are not due solely to the appreciable quantum effects.[5] Molecular hydrogen has a number of distinctive features of the intermolecular interaction that make it different from all other homonuclear diatomic systems. The exceptionally soft repulsion of its molecules at short distances due to the absence of inner electronic shells accounts for the unique ability of hydrogen to be compressed in volume by more than a factor of ten in the condensed state without substantial changes to its molecular structure.[2] This peculiarity leads to certain difficulties in applying to hydrogen the well-developed methods of the theory of fluids, which make use of the model of rigid, impermeable molecules.

At the same time, the interaction laws for atoms and

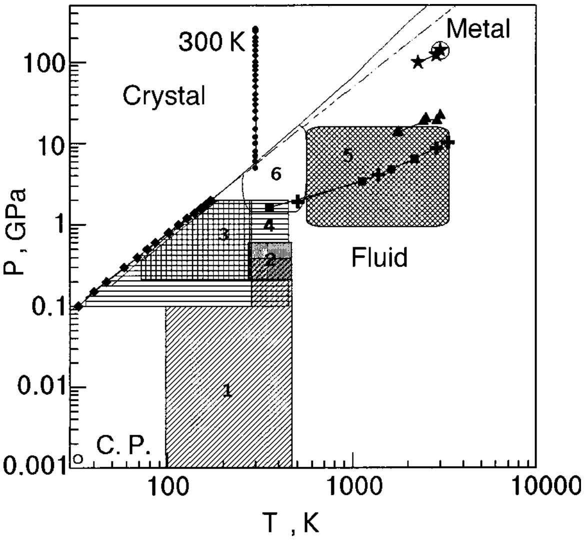

FIG. 1. $P-T$ relation for fluid hydrogen on the line of crystallization, according to Ross[19] (solid line), and a linear extrapolation in logarithmic coordinates (dashed line). The various shadings indicate the regions of the experimental studies of Michels *et al.*,[15] 1959 (*1*); Tsiklis *et al.*,[16] 1975 (*2*); and Mills *et al.*,[17] 1977 (*3*); and the domains of applicability of the equation of state of Sheĭnina *et al.*,[4] 1993 (*4*); the classical atom–atom approximation[7] (*5*); the atom–atom approximation with quantum corrections (present study) (*6*). The letters C.P. label the liquid–vapor critical point (○). Data obtained under various types of compression: shock[18,20] (■, +); double shock (behind the reflected shock wave)[20] (▲); quasi-isentropic[3] (★); static (diamond anvil)[2] (●). Data on the line of crystallization[1,2] (◆).

molecules of hydrogen are now well known.[5] There are some theoretical models capable of describing a noncentral interaction of hydrogen isotopes.[2,5] There have also been a number of successful attempts to explain on the basis of these models the phase transitions observed in condensed hydrogen at high pressures[5] and low temperatures, where the quantum properties of the crystal are domimant. In the high-temperature region, on the contrary, it has turned out that the results of dynamic experiments can be described correctly on the basis of purely classical models.[7] Here the atom–atom approximation gives a simple and reliable basis for predicting the properties of fluid hydrogen at high pressures.[9] In the atom–atom approach it is relatively simple to describe the effects associated with the nonrigidity of the hydrogen molecules and which are manifested in changes in the length of the chemical bond and the frequency of intramolecular vibrations.

Nonrigidity effects, which play an important role in highly compressed fluid hydrogen at high temperatures,[7,9] remain substantial at intermediate temperatures as well, especially near the line of crystallization, where the density of the fluid is high. In this region, however, one cannot neglect quantum effects, particularly for the light isotopes of hydrogen. The goal of the present study is to investigate the possibility of using the atom–atom approximation in conjunction with quantum corrections in order to predict the behavior of dense hydrogen near the line of crystallization.

ATOM–ATOM APPROXIMATION

In the atom–atom approximation[7,9] the energy of interaction of hydrogen molecules is expressed in terms of the interaction energy of individual pairs of atoms. Two hydrogen atoms, as we know, interact differently depending on their total spin.[10] In the singlet ground state $^1\Sigma$ the atoms form an H_2 molecule — a bound state with a well depth of 4.75 eV and a bond length of about 0.74 Å. In the triplet excited state $^3\Sigma$ the curve of the interaction energy does not have a minimum (except for a small dispersion well at a distance greater than 3 Å).

In the atom–atom approximation the intermolecular interaction energy can be expressed relatively simply in terms of the interaction energy of the atoms within the molecule. This approximation is based on the Bohm–Alrichs theorem, which was proved by those authors in Ref. 8 in the Hartree–Fock approximation, in which the molecular orbitals are represented by a linear combination of atomic orbitals (LCAO MO). According to the theorem, the energy of the nonvalent interaction of two atoms (i.e., the interaction energy of two atoms belonging to different molecules with closed electronic shells) is equal to the weighted average (i.e., with allowance for the degeneracy with respect to projections of the spin and orbital angular momenta) of the interaction energy of two free atoms calculated in this same approximation.

According to the theorem, the nonvalent interaction potential $\varphi(r)$ of hydrogen atoms can be calculated as a linear combination of the singlet and triplet potentials, with weights proportional to the multiplicities of these states:

$$\varphi(r)=\frac{1}{4}U(^1\Sigma|r)+\frac{3}{4}U(^3\Sigma|r). \tag{1}$$

Here $U(^1\Sigma|r)$ is the interaction energy of two atoms in the $^1\Sigma$ ground state (with antiparallel spins); $U(^3\Sigma|r)$ is the interaction energy of atoms in the $^3\Sigma$ excited state (with parallel spins).

The total energy of two H_2 molecules found in the electronic ground state $^1\Sigma$ in the atom–atom approximation consists of intra- and intermolecular contributions:

$$U_2=U(^1\Sigma|R_{12})+U(^1\Sigma|R_{34})\varphi(r_{13})$$
$$+\varphi(r_{14})+\varphi(r_{23})+\varphi(r_{24}). \tag{2}$$

The indices 1 and 2 refer to the atoms bound together in the first molecule, while 3 and 4 refer to the atoms bound in the second molecule. Here and below $R_{ij}=R_{12},R_{34},\ldots$ are the intramolecular interatomic distances (the instantaneous lengths of the chemical bonds in the molecules), while $r_{ij}=r_{13},r_{14},\ldots$ denote the instantaneous distances between atoms of different molecules (intermolecular distances).

For N molecules the generalization of Eq. (2) is written

$$U_N=\sum_{\text{intra}}U(^1\Sigma|R_{ij})+\sum_{\text{inter}}\varphi(r_{ij}). \tag{3}$$

The first sum in (3) is over the intramolecular interactions of all N molecules, and the second sum is over all the $2N(N-1)$ pairs of atoms belonging to different molecules.

For describing the intramolecular potential energy in the $^1\Sigma$ state in the region of relatively low temperatures in this paper we use the Morse function:

$$U(^1\Sigma|R)=D_e\{\exp[-2\beta(R/R_e-1)]$$
$$-2\exp[-\beta(R/R_e-1)]\}. \tag{4}$$

The potential (4) contains three parameters which are determined from the results of quantum-mechanical calculations[10] and which are practically equal to those found from the spectroscopic measurements: $R_e=0.74126$ Å is the length of the chemical bond in the molecule, $D_e=4.788$ eV is the binding energy of the atoms in the molecule, and the parameter $\beta=1.4403$.

The nonvalent interaction potential $\varphi(r)$ was represented in the approximation proposed by Saumon and Chabrier:[13]

$$\varphi(r)=\varepsilon\{\gamma\exp[-2s_1(r-r^*)]$$
$$-(1+\gamma)\exp[-s_2(r-r^*)]\}. \tag{5}$$

The parameters appearing in Eq. (5), $r^*=3.2809$ Å, $\varepsilon=1.74\times10^{-3}$ eV, $\gamma=0.4615$, $s_1=1.6367\,\text{Å}^{-1}$, and $s_2=1.2041\,\text{Å}^{-1}$, were obtained in Ref. 13 on the basis of the well-known variational calculations of Kolos and Wolniewitz for the H_2 molecule.[10] Formula (5) gives a very accurate description of potential (1) over a wide interval of distances (from 0.5 to 3.5 Å), including the region of strong repulsion at short distances and the region of weak dispersional attraction at large distances.

Thus the atom–atom approximation (1)–(3) with the potentials (4) and (5) permits a quite simple determination of the potential surface of the ground state of a system consisting of an arbitrary number of hydrogen molecules. We note

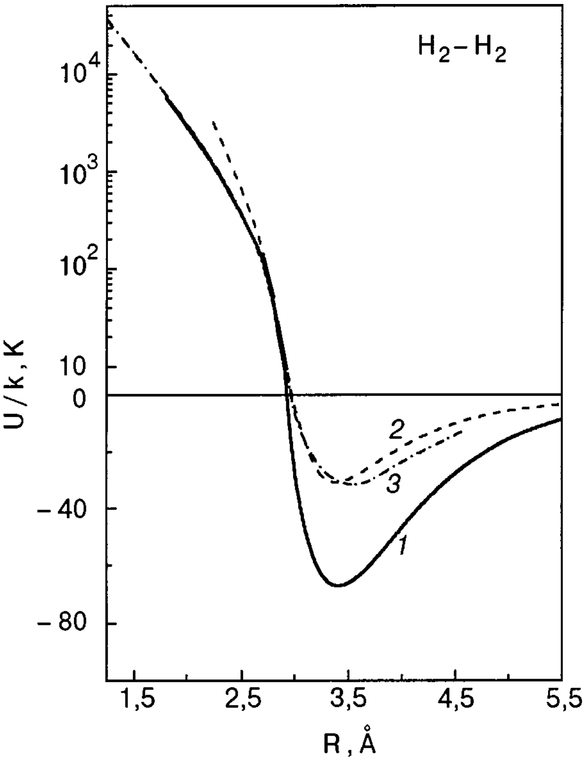

FIG. 2. Isotropic part of the interaction potential of two hydrogen molecules: the potential of the atom–atom approximation, averaged over all orientations for a fixed bond length $R_e = 0.74$ Å(1); the empirical Lennard-Jones potential ($\sigma = 2.95$ Å, $\varepsilon/k = 32$ K) (*2*); the Silvera–Goldman potential[12] (*3*).

that this approximation does not contain any adjustable parameters found from the experimental data but uses only the pair potentials $U(^1\Sigma|R)$ and $U(^1\Sigma|R)$ obtained from *ab initio* calculations.[10]

A comparison of the predictions of the atom–atom approximation with the results of direct quantum-mechanical calculations of the H_2–H_2 interaction energy and with the results of experiments on the scattering of molecular beams has shown[7] that this approximation gives an entirely satisfactory description of the short-range repulsion of the molecules but that the molecular attraction at large distances is overestimated somewhat. This is seen in Fig. 2, which shows the interaction potentials of two hydrogen molecules, averaged over all orientations. Moreover, the atom–atom approximation at large distances does not recover the asymptotic behavior of the orientational part of the intermolecular potential, in particular, that of its quadrupole–quadrupole component. This shortcoming, which is important at relatively low densities, can also be important in the description of phase transitions in solid hydrogen.[5] At the same time, at high pressure in the isotropic phase, where the main role is played by the short-range repulsive forces, this aspect of the atom–atom approximation plays a secondary role. The thermodynamic properties of shock-compressed hydrogen and deuterium predicted on the basis of this approximation are in good agreement with the experimental data at high temperatures and at pressures up to hundreds of kilobar (tens of GPa).[7,9]

Calculations have shown[9] that at ultrahigh (megabar) pressures the atom–atom approximation begins to overestimate the intermolecular attraction considerably. This is apparently because it completely ignores the electronic excitation, which ultimately leads to metallization of fluid hydrogen at high temperatures and pressures. Thus the domain of applicability of the atom–atom approximation (see Fig. 1) is bounded at both high and low densities (pressures).

QUANTUM CORRECTIONS

For predicting the thermodynamic behavior of dense deuterium and especially hydrogen at lower temperatures on the basis of the atom–atom approximation, one must modify this approach to incorporate quantum-mechanical effects, which play a governing role in the behavior of these light molecules at low temperatures. In this paper we use the approach proposed by Feynman, which is based on his variational procedure for the free energy.[11]

In this approach the free energy of a quantum-mechanical particle in an external field can be calculated approximately by a classical method if its potential energy $V(r)$ is replaced by a certain effective potential $\tilde{U}(r,T)$ given by[11]

$$\tilde{U}(r,T) = \frac{1}{\sqrt{\pi}} \int_{-\infty}^{+\infty} V(r+\lambda t)\exp(-t^2)dt. \tag{6}$$

The parameter

$$\lambda = \hbar/\sqrt{6mkT} \tag{7}$$

plays the role of the quantum-mechanical wavelength associated with the given particle; k is Boltzmann's constant.

In the simplest cases the quantum corrections to the potential in approximation (6) are easily calculated explicitly. For example, for the harmonic oscillator $V(R) = (1/2)m\omega^2(R-R_e)^2$ with frequency ω and equilibrium distance R_e, formula (6) gives a distance-independent correction that is inversely proportional to the temperature and similar in meaning to the contribution from the energy of zero-point vibrations:

$$\tilde{U}(R,T) = \frac{m\omega^2}{2}(R-R_e)^2 + \frac{(\hbar\omega)^2}{24kT}. \tag{8}$$

For the exponential repulsive potential $V(r) = A\exp(-br)$, formula (6) leads simply to a renormalization of the pre-exponential factor, which becomes temperature-dependent:

$$A \to A\exp\{\lambda^2 b^2/4\}. \tag{9}$$

As we see, taking quantum effects into account in the framework of the Feynman approach here reduces simply to some increase in the effective interatomic repulsion. A rough estimate of the possible influence of these effects on the repulsion of the atoms is easily made by taking into account that the parameter b is close to 2 $(\text{a.u.})^{-1}$ for many atoms.[7] For example, for deuterium at $T = 500$ K the increase in the repulsion is only around 2.5%, but for hydrogen at $T = 200$ K it is already about 20%.

Thus one can assume that in the investigated temperature interval, taking quantum effects into account in the *intermolecular* interaction can be done at the level of a correction to

TABLE I. Calculated and experimental thermodynamic properties of fluid hydrogen ($N=256$) at $T=200$ K ($V=11.17$ cm^3/mole, $\lambda=0.20$ Å), 300 K ($V=11.63$ cm^3/mole, $\lambda=0.16$ Å), and 500 K ($V=12.53$ cm^3/mole, $\lambda=0.13$ Å) on the $P=2$ GPa isobar.

T, K	Method	P, GPa	C_V/R	C_P/R	α_T, 10^{-3} K^{-1}	β_T, GPa^{-1}	a, km/s
200	Without quantum correction	1.56	4.99	5.57	0.62	0.17	5.98
	With quantum correction	1.81	2.84	3.26	0.48	0.15	6.59
	Experiment (Ref. 4)	2.00	2.98	3.62	0.42	0.15	6.40
300	Without quantum correction	1.62	4.63	5.29	0.54	0.18	6.02
	With quantum correction	1.75	3.22	3.62	0.37	0.15	6.59
	Experiment (Ref. 4)	2.00	3.24	3.64	0.39	0.16	6.38
500	Without quantum correction	1.70	4.40	4.90	0.35	0.18	6.18
	With quantum correction	1.72	3.12	3.56	0.32	0.18	6.34
	Experiment (Ref. 4)	2.00	3.14	3.68	0.36	0.18	6.37
	Δ_{calc}	0.01	0.03	0.05	0.02	0.02	0.05

Note: Δ_{calc} is the absolute error of the calculation.

the intermolecular potential, and the Feynman variational approach[11] can be completely applicable to highly compressed hydrogen isotopes.

While the quantum corrections to the intermolecular interaction will be extremely insignificant at temperatures above 500 K, at temperatures below 200 K the influence of quantum effects will be too great to be treated like the corrections mentioned above. Fortunately, in this region the properties of fluid hydrogen have been investigated experimentally almost right up to the line of crystallization.[1,4]

As to the *intramolecular* vibrations, their quantum character is manifested at much higher temperatures, so that a correction of the type (8) is inadequate in the investigated temperature interval. The quantity in Eq. (8) becomes comparable to the heat capacity itself at temperatures above 1000 K.

In view of this and also of the fact that the correction (8) gives only the first term, linear in the inverse temperature, of the expansion of the exact expression for the contribution of the heat capacity of the harmonic oscillator to the free energy, one can [while remaining formally within the framework of the Feynman approach (6)] replace $(\hbar\omega)^2/24kT$ in (8) by

$$kT\ln\left(\frac{\sinh z}{z}\right), \tag{10}$$

where $z=\hbar\omega/kT$. At high temperatures the function (10) goes over to $(\hbar\omega)^2/24kT$, and at low temperatures it gives the exact expression for the harmonic-oscillator contribution to the free energy and the other thermodynamic properties. Although this modification of the Feynman approach cannot claim to be rigorous, it does permit one to advance into the region of lower temperatures, as may be judged only from a direct comparison with experiment. Below we present the results of such a comparison.

MONTE CARLO CALCULATIONS

To predict the properties of fluid hydrogen on the basis of the atom–atom approximation with the quantum corrections introduced above, we chose the method of Monte Carlo simulation. This approach can be used to eliminate the well-known inaccuracies in the solution of the statistical problem which are inherent to the present-day theoretical methods, such as the method of integral equations or the method of thermodynamic perturbation theory. The errors inherent to the Monte Carlo method are easily monitored by modern computational techniques and can be reduced to an acceptable level.

The calculation was done in an NVT ensemble, with N hydrogen atoms placed in a rectangular cell with periodic boundary conditions. The size of the cell was determined by the specified density, and the initial configuration corresponded to a random distribution of molecules with bond lengths close to the equilibrium bond length R_e. Each step of the experiment included a random choice of an individual atom, for which an attempt was made to move it to a new position within a specified distance Δ. Discrimination of the steps was carried out by the standard Metropolis method.[14] The value of Δ was chosen such that around 40% of the steps were successful. After equilibrium was established, which took about 1000 successful steps/atom,[1] the computer began to store the total values of the total energy and pressure and their squares and products for calculation of the necessary properties of the fluid. The accumulation of statistics was repeated after each atom had been displaced to a new position an average of three times and was continued for about 40 thousand successful steps per atom, until all the averages had stabilized and acceptable values had been obtained for the probable errors, which were estimated by standard statistical methods for a confidence level of 0.95.

The following averages were calculated:[2] the pressure

$$P=\frac{NkT}{V}+\frac{1}{3N}\left\langle\sum_{\text{intra}}R_{ij}\frac{\partial\tilde{U}(R_{ij})}{\partial R_{ij}}+\sum_{\text{initer}}r_{ij}\frac{\partial\tilde{\varphi}(r_{ij})}{\partial r_{ij}}\right\rangle; \tag{11}$$

the total energy

$$E=\frac{3}{2}kT+\frac{1}{2N}\left\langle\sum_{\text{intra}}\left\{\tilde{U}(R_{ij},T)-T\frac{\partial\tilde{U}(R_{ij},T)}{\partial T}\right\}\right.$$
$$\left.+\left\{\sum_{\text{inter}}\tilde{\varphi}(r_{ij},T)-T\frac{\partial\tilde{\varphi}(r_{ij},T)}{\partial T}\right\}\right\rangle; \tag{12}$$

and the isothermal compressibility $\beta_T=-(1/V)(\partial V/\partial P)_T$, the thermal pressure $P_T=T(\partial P/\partial T)_V$, and the isochoric

TABLE II. Thermodynamic properties of fluid hydrogen on the $T=300$ K isotherm.

Reduced density V_0/V	V, cm^3/mole	P, GPa	P_{in}, GPa	E, eV	E_{in}, eV	C_v/R	C_P/R	α_T, $10^{-3}\cdot\text{K}^{-1}$	β_T, GPa−1	a, km/s
2.12	11.63	1.76	0.16	−4.483	−4.568	3.12	3.64	0.44	0.158	6.53
2.82	10.00	2.97	0.25	−4.457	−4.568	3.18	3.58	0.32	0.094	7.69
3.13	9.00	4.31	0.36	−4.429	−4.568	3.15	3.51	0.27	0.067	8.63
3.31	8.50*	5.25	0.44	−4.409	−4.568	3.07	3.40	0.25	0.056	9.15

Note: $V_0=28.16$ cm^3/mole is the volume of liquid hydrogen at atmospheric pressure; the asterisk * indicates a state near equilibrium with the solid phase.

heat capacity C_V. The expressions for these thermodynamic functions in terms of the potentials are more awkward, and we will not give them here.

The energy of the intramolecular interaction of atoms $U(^1\Sigma|R)$ was calculated according to Eq. (4), and the corresponding frequency ω in Eq. (13) was expressed in terms of the parameters of the Morse potential (4) and the mass m of an atom:

$$\omega=\beta(R_e)^{-1}(2D_e)^{1/2}m^{-1/2}.$$

The effective intramolecular interaction potential $\tilde{U}(R,T)$ was calculated on the basis of (4) with the correction (10), both for the harmonic oscillator,

$$\tilde{U}(R,T)=U(^1\Sigma|R)+kT\left[\ln\left(\sinh\left(\frac{\hbar\omega}{kT}\right)\right)-\ln\left(\frac{\hbar\omega}{kT}\right)\right], \tag{13}$$

and for an effective intermolecular interaction potential $\tilde{\varphi}(r,T)$ of the atoms according to (5) and (9), i.e.,

$$\tilde{\varphi}(r,T)=\varepsilon\{\gamma c_1(T)\exp[-2s_1(r-r^*)] \\ -(1+\gamma)c_2(T)\exp[-s_2(r-r^*)]\}. \tag{14}$$

Here the coefficients $c_k(T)=\exp\{-\lambda^2 s_k^2\}$, $k=1,2$.

The isobaric heat capacity C_P, the volume coefficient of thermal expansion $\alpha_T=-(1/V)(\partial V/\partial T)_P$, and the sound velocity a were calculated from the known thermodynamic relations. The characteristic intramolecular contributions to the pressure P_{intra} and internal energy E_{intra} for the model of nonrigid molecules were calculated separately; as was shown previously,[9] they are appreciable at high densities. We also calculated the probability density for finding bound and unbound atoms at various distances (the intra- and intermolecular proton–proton distribution functions).

In every case the calculations were done for $N=256$ atoms in the cell, and some (at $T=300$ K) were also done for $N=500$ atoms (128 and 250 H_2 molecules in the cell, respectively). The interatomic interaction potential was ''cut off'' at a distance $r_{\max}=7$ Å; this did not introduce any new errors of practical consequence. For estimating the contribution of quantum effects the calculations were also done with and without the quantum corrections. In Table I the results for different temperatures along the 2 GPa isobar are compared with the experimental data.[4]

RESULTS AND DISCUSSION

A comparison of the results of a Monte Carlo computer simulation and the data obtained in Ref. 4 show good agreement, on the whole.

The only disagreement is that the calculated pressure of the fluid hydrogen is somewhat (about 0.2 GPa) lower than experiment, even when the quantum corrections are taken into account. The same disagreement is also observed with the data obtained in shock compression,[18,19] which agree in the temperature interval under consideration (see Fig. 1). This is apparently due to the aforementioned characteristic overestimate of the attraction of the molecules at large distances in the atom–atom approximation[9] (see Fig. 2).

As expected, the isochoric heat capacity is particularly influenced by quantum effects over the entire investigated temperature interval. The corrections to the thermal expansion coefficients and sound velocity are less important, but even for them the agreement with experiment is improved when these corrections are taken into account. As the temperature increases, this agreement becomes better and better, although even for $T=200$ K the predictions can be considered completely satisfactory for an approach that does not contain even one adjustable parameter. It is seen that the quantum corrections in the given temperature interval give

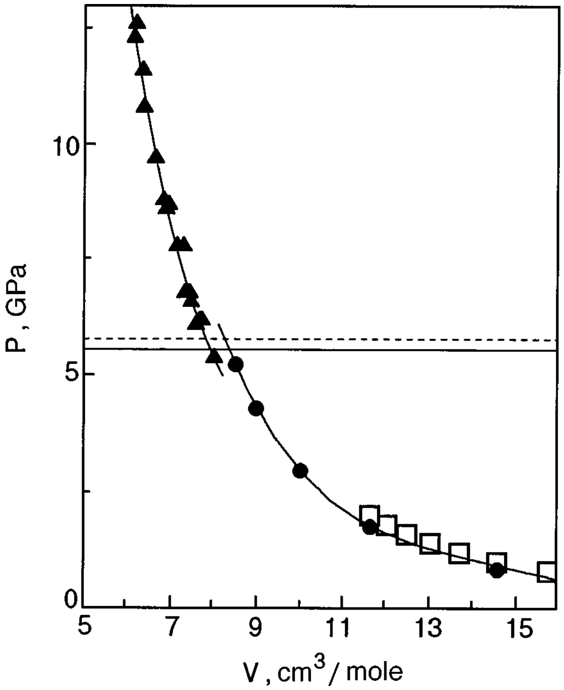

FIG. 3. The crystal–fluid transition at 300 K in normal hydrogen (along the $P(V)$ curve): the data of a static experiment in the solid phase, by Mao and Hemley[2] (▲); the atom–atom approximation with quantum corrections (present study) (●); the equation of state of Sheĭnina *et al.*[4] for the fluid (□); The horizontal lines are the linear extrapolation of $\ln P_s$–$\ln T$ (solid line) and the calculation of $P_s(T)$ by Ross[19] (dashed line).

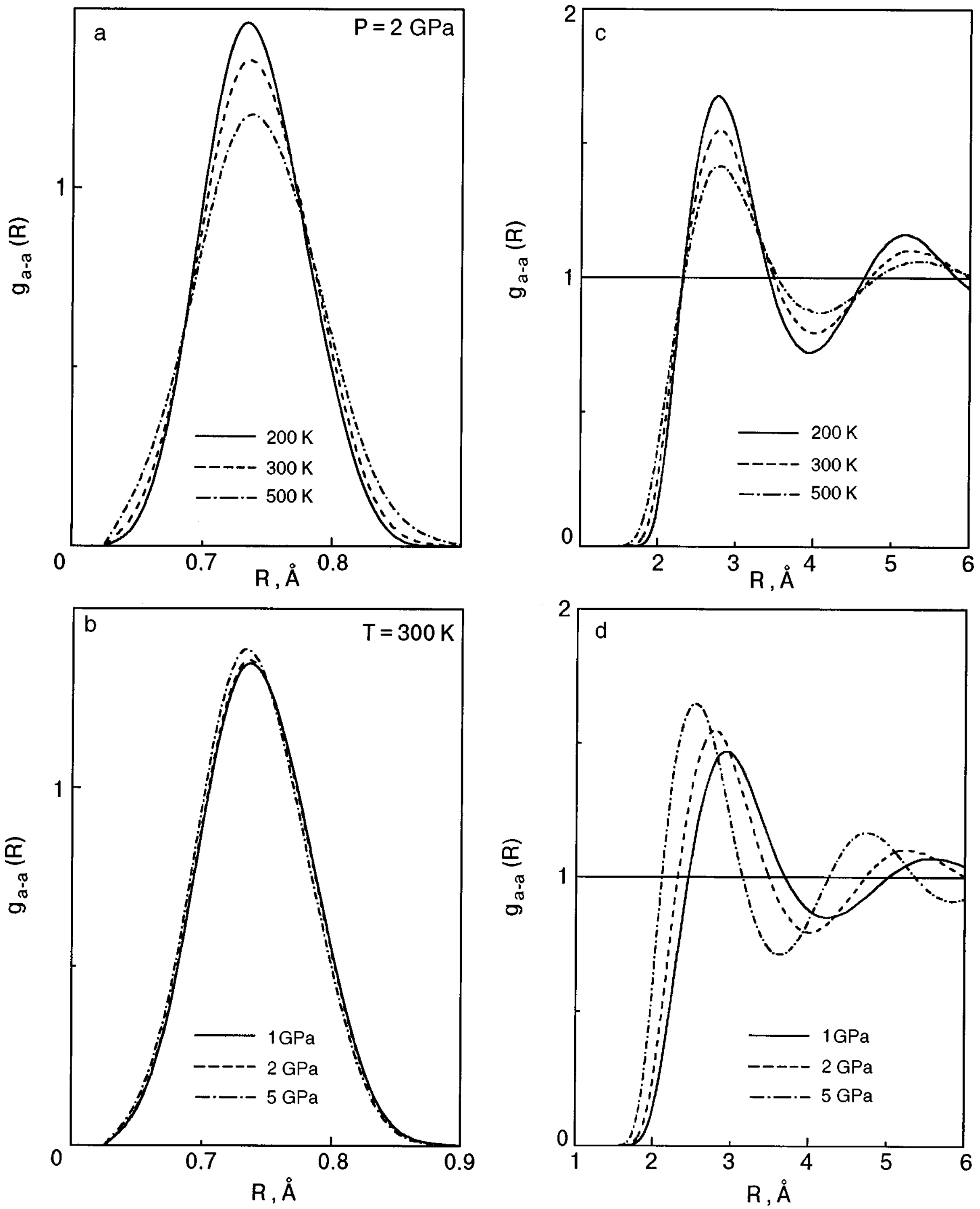

FIG. 4. Binary atom–atom distribution function at $P=2$ GPa for various temperatures (a,c) and at $T=300$ K for various pressures (b,d) (a and b show the intramolecular part; c and d the intermolecular part).

approximately the same contribution to the pressure (of the order of 10%) as the typical value of the intramolecular contribution[9] due to the nonrigidity of the hydrogen molecule. Taking the quantum corrections into account is absolutely necessary not only in calculating the heat capacity but also the thermal expansion, and it substantially improves the agreement with experiment, especially at low temperatures.

Table II presents the predicted properties of fluid hydrogen at high densities on the $T=300$ K isotherm. The second and lower rows of the table pertain to the region near the crystallization curve ($P \gg 2$ GPa), for which we do not know of any experimental data.

The estimated error of the Monte Carlo calculation averaged over all the simulations is given in Table I. The difference between the results of the calculation for $N=256$ and 500 can be seen by comparing the second row in Table II with the data in Table I for the same state ($T=300$ K, $V=11.63$ cm^3/mole). The changes in the values of most of the characteristics when the number of atoms is increased lie within the range of the statistical error. The pressure and internal energy can be reliably estimated using $N = 256$. The second derivatives of the free energy, especially the coefficients of thermal expansion and isothermal compressibility (and the sound velocity related to it), are more sensitive to the number of atoms in the cell.

Calculations done within the experimentally investigated region have predicted the behavior of highly compressed fluid hydrogen near the line of crystallization. Figure 3 shows a comparison of the $P(V)$ curves of the fluid and crystalline phases on the $T = 300$ K isotherm. We see that there is a jump of about $0.5\,\mathrm{cm}^3$/mole in the volume of the fluid and crystal at the independently established value of the pressure of crystallization (5.6–5.9 GPa, according to the estimates of different authors); this value of the pressure jump is in good agreement with the available experimental data at lower temperatures.[1,4] It should be emphasized that satisfactory agreement with experiment is achieved only when both the nonrigidity of the molecules (in particular, the intramolecular contribution to the pressure) and the quantum corrections are taken into account.

Figure 4 shows the temperature–density dependence of the the intra- and intermolecular components of the atom–atom distribution functions. As it turns out, even very slight changes in the intramolecular distribution function with pressure can lead to an appreciable contribution of the nonrigidity to the thermodynamic properties (see Table II).

CONCLUSION

The atom–atom approximation is a relatively simple nonempirical approach that is nevertheless suitable for quantitative prediction of the behavior of simple molecular fluids under pressure. All that is required for using this approach is the value of the interaction potential of two isolated atoms in different electronic states of the diatomic quasimolecule formed by them. These potentials (determined to high accuracy) are now available not only for hydrogen but also for nitrogen, fluorine, and other simple homonuclear systems. The predictions of the atom–atom approximation are in reasonable agreement with the existing experimental data both at high temperatures[7,9] and at moderate temperatures, in spite of the fact that the atom–atom potentials do not explicitly contain contributions from the short-range multiparticle and long-range electrostatic intermolecular forces and that the electronic excitation of the molecules is not fully taken into account.

In this paper we have introduced quantum corrections to the atom–atom approximation and have shown that this approach can be extended to the region of relatively low temperatures. We have calculated the thermodynamic properties and structure parameters of fluid hydrogen at high pressures, beyond the limits of the experimentally investigated region near the line of crystallization.

Even though the atom–atom approximation does suffer from the list of shortcomings mentioned above, as a nonempirical approach this approximation has its indisputable advantages and its own sphere of application. Expressions for the thermodynamic functions in the framework of the atom–atom approximation are simple,[9] and the individual contributions to them have clear physical meaning. This approach requires a minimum of initial information for predicting the properties, makes it possible to describe the effects of molecular nonrigidity, and can be useful for predicting the behavior of molecular fluids at high pressures not only in the Monte Carlo approach or in the theory of integral equations[7,9] but also in a molecular-dynamics calculation of the diffusion, viscosity, and other transport properties of compressed fluids.

In the region of relatively low temperatures, where the efficacy of the *ab initio* methods[6] is most problematic, the atom–atom approximation, which is not so demanding of computer resources, enjoys an advantage. Its application can also be useful in the study of the structure and properties of solid hydrogen and other diatomic homonuclear systems at high pressures.[21]

---

*E-mail: unive@paco.net

1) In states close to the line of crystallization the establishment of equilibrium is a much slower process, and the number of successful steps necessary increased sometimes to several thousand per atom.

2) The angle brackets denote averaging over the Markov chain (per atom) generated by the Monte Carlo method.

---

[1] B. I. Verkin (ed.), *Properties of Condensed Phases of Hydrogen and Oxygen* [in Russian], Naukova Dumka, Kiev (1984).

[2] H. K. Mao and R. J. Hemley, Rev. Mod. Phys. **66**, 671 (1994).

[3] S. T. Weir, A. C. Mitchell, and W. J. Nellis, Phys. Rev. Lett. **76**, 1860 (1996).

[4] A. A. Sheĭnina, N. G. Bereznyak, V. P. Vorob'eva, and M. A. Khadzhmuradov, Fiz. Nizk. Temp. **19**, 504 (1993) [Low Temp. Phys. **19**, 356 (1993)].

[5] V. G. Manzhelii and Yu. A. Freiman (eds.), *Physics of Cryocrystals*, AIP Press, Woodbury, New York (1996).

[6] W. R. Margo, D. M. Ceperley, C. Pierleoni, and B. Bernu, Phys. Rev. Lett. **76**, 1240 (1996).

[7] E. S. Yakub, Fiz. Nizk. Temp. **20**, 739 (1994) [Low Temp. Phys. **20**, 579 (1994)].

[8] H.-J. Bohm and R. Ahlrichs, J. Chem. Phys. **77**, 2028 (1982).

[9] E. S. Yakub, Physica B **265**, 31 (1999).

[10] W. Kolos and L. Wolniewitz, J. Chem. Phys. **41**, 3363 (1965); **43**, 2429 (1966).

[11] R. P. Feynman and A. R. Hibbs, *Quantum Mechanics and Path Integrals* [McGraw-Hill, New York (1965); Mir, Moscow (1968)].

[12] I. F. Silvera and V. V. Goldman, J. Chem. Phys. **69**, 4209 (1978).

[13] D. Saumon and G. Chabrier, Phys. Rev. A **44**, 5122 (1990).

[14] N. Metropolis, V. Rosenbluth, N. Rosenbluth, A. Teller, and E. Teller, J. Chem. Phys. **21**, 1087 (1953).

[15] A. Michels, W. De Graaff, T. Wassenaar, J. M. H. Levelt, and P. Louwerse, Physica (Amsterdam) **25**, 85 (1963).

[16] D. S. Tsiklis, V. Ya. Maslennikova, S. D. Gavrilov, A. I. Egorov, and G. V. Timofeeva, Dokl. Akad. Nauk **220**, 1384 (1975).

[17] R. L. Mills, D. H. Liebenberg, J. C. Bronson, and L. C. Schmidt, J. Chem. Phys. **66**, 3076 (1977).

[18] R. D. Dick and G. I. Kerley, J. Chem. Phys. **73**, 5264 (1980).

[19] M. Ross, in *Shock Waves in Condensed Matter*, edited by J. R. Asay, R. A. Graham, and G. K. Starub, Elsevier, New York (1984).

[20] W. J. Nellis, A. C. Mitchell, M. van Thiel, G. R. Devine, R. J. Trianor, and N. Brown, J. Chem. Phys. **79**, 1480 (1983).

[21] E. S. Yakub, J. Low Temp. Phys. **111**, 357 (1998).

Translated by Steve Torstveit

LOW TEMPERATURE PHYSICS VOLUME 26, NUMBER 4 APRIL 2000

SUPERCONDUCTIVITY, INCLUDING HIGH-TEMPERATURE SUPERCONDUCTIVITY

Low-field electrodynamics of granular high-temperature superconductors

V. K. Ignat'ev* and I. V. Neginskiĭ

Volgograd State University, ul. 2-ya Prodol'naya 30, 400062 Volgograd, Russia

(Submitted May 25, 1999; revised November 17, 1999)
Fiz. Nizk. Temp. **26**, 340–349 (April 2000)

Studies of the low-field electrodynamics of YBaCuO ceramic superconductors are described. An analytical treatment and a numerical simulation are carried out in the model of pinning and viscous flow of hypervortices in high-T_c superconductors (HTSCs) to find the dependence of the real and imaginary components of the surface impedance on the modulus of a static magnetic field and on the amplitude and frequency of an alternating field. Experimental results are presented on the magnetic-field dependence of the impedance components. The studies were carried out in the frequency range from 30 Hz to 1 kHz and at amplitudes of the alternating component of the field from 0.1 to 10 Oe. It is shown that the critical-state model is applicable to HTSCs in the region of low frequencies and small amplitudes of the alternating component of the field. The model of viscous flow of hypervortices gives a good description of the low-field electrodynamics of HTSCs over a wide range of frequencies and, in particular, predicts the experimentally observed hysteresis of the magnetic-field dependence of the surface impedance. © *2000 American Institute of Physics.* [S1063-777X(00)00304-2]

INTRODUCTION

Ceramic superconductors are now regarded as nonlinear materials whose electromagnetic properties are determined by the presence of three different phases in them: superconducting granules, an intergranule contact phase, and a normal phase in the intergranule space.[1] The presence of Josephson junctions in a ceramic superconductor gives rise to features in the flow of transport currents through the granular medium; the domain of applicability of the Bean model in these superconducting materials is therefore limited. For this reason the construction of a consistent phenomenological model of the critical and resistive states in ceramics is a topical problem.

The appreciable nonuniformity of the magnetic field distribution inside ceramic superconductors and the nonlinearity of the characteristics of the intergranule Josephson contacts in external magnetic fields up to 100 Oe makes the description of the low-field electrodynamics of HTSC ceramics with the use of effective values (of the magnetic permeability, for example) is incorrect. The value of the magnetic field at the observation point inside a sample is determined by both the distribution of the magnetic induction in a wide neighborhood of this point and by the magnetic prehistory of the sample; therefore the effective values of the magnetic permeability will depend on the character of the magnetic field: on its amplitude, frequency, and direction of sweep. Thus the magnetic permeability in this case is not a parameter of the medium but will depend on the external field applied. Therefore, it is more correct to speak of the surface impedance of the sample, the first harmonic of which is given as the ratio of the amplitude of the first harmonic of the electric field to the amplitude of the sinusoidal magnetic field at the surface of the sample. Using a mutual-inductance method[2] one can measure directly the electric field length surface of the sample at a rigidly fixed value of the magnetic field. For this reason the systematic error in the measurements due to the model representation of the electrodynamics of the sample can in practice be completely neglected.

Numerous studies have established that the electrodynamics of HTSCs in the low-frequency limit are described well by the critical-state model. From the results of surface impedance measurements on HTSCs in this frequency range one can recover completely the magnetic-field dependence of the critical current. Therefore, studying the surface impedance of a HTSC is a tried-and-true method of constructing the phenomenological electrodynamics of ceramic superconductors. The high-frequency electrodynamics of HTSCs, on the other hand, has a number of features that are not described by the Bean model, and the limits of applicability of this model to ceramic superconductors have not been clearly established.

In the this paper we attempt to describe the electrodynamics of of HTSCs over a wide frequency range in the model of pinning and viscous flow of hypervortices.[3] The main problem here is to find the parameters of the medium, or, more precisely, the phenomenological constants of the model, from experimental measurements of the surface impedance. This problem can be split up into several stages. First, in the framework of the model under study we must obtain analytical expressions for the family of integral characteristics of the medium in certain limiting cases and also measure these characteristics. Their agreement with the known expressions obtained in the critical-state model will serve to confirm the adequacy of both the model and the chosen method of investigation.

After an experimental study of the magnetic-field and frequency dependences of the surface impedance over a wide frequency range, a comparison of the experimentally and theoretically obtained families of integral characteristics will yield the parameters of the model and, hence, a prediction as to the reaction of the medium to an arbitrary external influence. Of course, since the system is nonlinear, the family of integral characteristics can be constructed in the general case only with the aid of a numerical simulation in the framework of the proposed model.

MODEL OF PINNING AND VISCOUS FLOW OF HYPERVORTICES

The penetration of a magnetic field into a superconductor found in the critical state can be described as a magnetic flux transport phenomenon. In the model of pinning and viscous flow of hypervortices[3] the magnetic field penetrates into the superconductor in the form of so-called hypervortices,[4] unlike the case of metallic superconductor, in which the magnetic field is transported by Abrikosov vortices. The dynamics of the motion of hypervortices in a sample, in analogy with the classical Kim–Andersen model,[5] is governed by the balance equation (1) for the three forces acting on it: the Lorentz force f_L (2), which is exerted by the external transport current, the viscous friction force f_{fr} (3), and the pinning force f_p, which has the meaning of a force of static friction:[6]

$$\mathbf{f}_L+\mathbf{f}_{\mathrm{fr}}+\mathbf{f}_p=0, \tag{1}$$

$$\mathbf{f}_L=[\mathbf{j}_T\times\mathbf{e}_B]\Phi, \tag{2}$$

$$\mathbf{f}_{\mathrm{fr}}=-\eta\mathbf{V}, \tag{3}$$

where Φ is the flux trapped by a hypervortex, and η is the coefficient of electrodynamic viscosity. However, the coefficient of viscosity and the pinning force which appear in these relations are functions of the magnetic induction at the observation point.

Analysis of the magnetic flux transport in the framework of Eq. (1) shows that one can distinguish two characteristic regimes. These are the flux-creep regime, in which the force of viscous friction is substantially smaller than the pinning force, and the regime of viscous flow of hypervortices, in which the force of viscous friction is significantly greater than the pinning force. Let us consider the dependence of the magnetic field penetration depth in a cylindrical sample in these two cases in the presence of an external field of the form $H(t)=H_0+H_m\cos(\omega t)$, where the constant component H_0 is slowly varied over the range from $-H_1$ to H_1.

In the first case there is practically no flux flow, and the viscous friction force f_{fr} (3), which is therefore proportional to the velocity of the vortices, is negligible or absent altogether. Then the Lorentz force counterbalances the pinning force f_p, and, in view of the definition of the critical current density,[6] we obtain a relation for the maximum pinning force f_p^m for a given material:

$$|\mathbf{B}|j_c=f_p^m. \tag{4}$$

Here, if the critical current density does not depend on the magnetic induction B, the density of vortices decreases linearly with depth in the superconductor, reaching zero (for $H_0=0$) at a distance $\lambda=H_m/j_c$. When the dependence of the critical current density on the alternating magnetic field is neglected, the penetration depth is independent of the frequency but proportional to the amplitude of the alternating component.

Equation (4) is the equation of the critical state in the strict Bean model. An estimate of the velocity $V\sim\omega l$ of the vortices, where l is the characteristic scale of variations, suggests that this model is most clearly realized in the region of low frequencies and small amplitudes. At low frequencies the force of viscous friction does not yet play a role in the redistribution of vortices inside the superconductor, and in view of the small amplitude one can say that the dimensions of the regions in which this redistribution occurs are small and, hence, that the displacements occur over short distances. Therefore, by studying the magnetic-field dependence of the surface impedance of a HTSC in the low-frequency region one can recover the equation of the critical state, i.e., the field dependence of the critical current, but not the coefficient of viscous friction of the vortices.

Analogous arguments suggest that a predominant influence of the force of viscous friction is more characteristic for a high-frequency alternating field with a large amplitude. For steady-state motion of the vortices, when the pinning force can be neglected because $f_{\mathrm{fr}}\gg f_p^m$, formula (1) has the form

$$\Phi j_T=\eta V. \tag{5}$$

Neglecting the vanishing of the vortices in the bulk of the superconductor, we can take[6]

$$\mathbf{E}=[\mathbf{V}\times\mathbf{B}], \tag{6}$$

and, with allowance for relation (5), we obtain

$$j=\frac{\eta}{\Phi B}E. \tag{7}$$

As a result, Eq. (1) takes the form of the differential Ohm's law $j=\sigma(B)E$ and describes the penetration of an alternating magnetic field to a depth $\lambda\sim\sqrt{\sigma(B)/\omega}$. Thus in the high-frequency limit, which is characteristic for the given regime, the penetration depth of the magnetic field is independent of the amplitude of the alternating component and decreases with increasing frequency according to a square-root law (as in the normal skin effect). By studying the surface impedance of HTSCs in this frequency range one can recover the field dependence of the coefficient of viscous friction of the vortices.

The flow of transport current along a superconductor is accompanied by the motion of hypervortices between potential wells, the role of which is played by pinning centers (α is the distance between pinning centers). In a weak external field (the flux-creep regime) the hypervortices execute hops between potential wells owing to thermal fluctuations in the system. The viscous flow regime corresponds to the process of continuous motion of the hypervortices. The dependence of their average velocity on the transport current density in these regime is described by the following relations (see the model of Ref. 3):

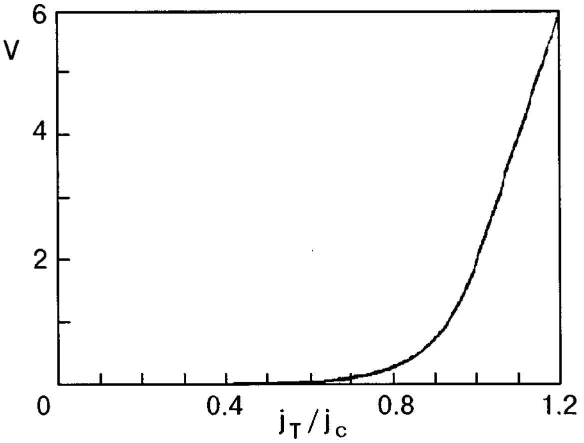

FIG. 1. Velocity of hypervortices (normalized to $kT/\alpha\eta$) versus the current density (see Eq. (8)).

$$V(|j_T|<j_c)=\frac{kt}{\alpha\eta}\left(\exp\left\{-\frac{\Phi\alpha}{kT}(j_c-|j_T|)\right\}-\exp\left\{-\frac{\Phi\alpha}{kT}(j_c+|j_T|)\right\}\right), \tag{8}$$

$$V(|j_T|>j_c)=\left(\frac{kT}{\alpha\eta}-\frac{kT}{\alpha\eta}\exp\left(-\frac{\Phi\alpha}{kT}(|j_T|+j_c)\right)+\frac{\Phi}{\eta}(|j_T|-j_c)\right), \tag{9}$$

where the velocity direction is determined by the direction of the vector product of the current density and magnetic induction at the observation point. The dependence of the modulus of the velocity V of the vortices on the transport current density is shown graphically in Fig. 1.

The depth of the potential well is determined by the dependence of the critical current on the local magnetic induction. In the model of pinning and viscous flow of hypervortices a superconductor is characterized by two functional relations:[3]

$$j_c(B)=\frac{j_{c0}}{(1+B^2/B_0^2)^{1/2}}, \tag{10}$$

$$\eta(B)=\eta_{00}+\eta_0\Phi B, \tag{11}$$

where j_{c0}, B_0, η_{00}, and η_0 are parameters of the superconductor.

ANALYTICAL ESTIMATES OF THE INTEGRAL CHARACTERISTICS OF A HTSC

Let us use the ideas set forth above to construct analytically the magnetic-field dependence of the impedance components in the following limiting cases: the flux-creep regime, corresponding to the critical state for the strict Bean model, and the regime of viscous flow of vortices. For simplicity we shall consider single-quantum vortices, i.e., $\Phi=\Phi_0$. We shall also assume that the second term in the expression (11) for the coefficient of viscosity is much greater than the coefficient η_{00}; this assumption corresponds to appreciable nonlinearity of the medium.

Since HTSC ceramics are media with strong dissipation and nonlinearity, the standard methods of analysis of the propagation of electromagnetic oscillations (the harmonic balance method, the method of slowly varying amplitudes) are inapplicable for them. For studying media of this kind one can use the power balance method,[7] in which one analyzes the energy balance in the system. For a sample in a uniform magnetic field H the power flux density, i.e., the Poynting vector, through the outer surface S_0 of the sample is equal to the change in its internal energy and the heat loss in it:

$$\oint_{S_0}\prod dS=P+\frac{dW}{dt},\quad \prod=[\mathbf{E}\times\mathbf{H}], \tag{12}$$

where P is the loss power in the sample and W is its internal energy.

Let us show that in a cylindrical sample of radius R in the case of a longitudinal harmonic external magnetic field the real component of the surface impedance is directly proportional to the average power loss in the system over a period:

$$\tilde{P}=\frac{1}{T}\int_0^T P\,dt. \tag{13}$$

Here we calculate the period-averaged value of the Poynting vector (12) through the lateral surface of a cylindrical sample of length L, taking into account that the average change in the internal energy of the system over a period is zero:

$$2\pi RLH_m^2 1/2\,\mathrm{Re}\,Z=\tilde{P}, \tag{14}$$

where the real component is defined as

$$\mathrm{Re}\,Z=\frac{2}{H_m}\int_0^{2\pi}E(t)\cos(\omega t)d(\omega t).$$

In the regime of viscous flow of hypervortices, under the assumptions made above as to the field dependence of the coefficient of electrodynamic viscosity, relation (7) takes the form of the differential Ohm's law describing the flow of current through a medium with conductivity η_0.

For the flux-creep regime one can use relation (14) to obtain analytically the dependence of the real component of the surface impedance on the static magnetic field. Let us consider in more detail the distribution of the magnetic field in the sample in a nonzero static magnetic field H_0 [Fig. 2a].

On the left in Fig. 2a we show the instantaneous distribution of the magnetic flux when the static component of the field falls from its maximum value of H_1 to an instantaneous value H_0, and on the right is the corresponding distribution when the field increases from its minimum value $-H_1$ to H_0.

Over the course of a period of the alternating component of the field the magnetic induction varies only in a small region of the order of the penetration depth λ of the alternating field. Then the losses in the sample over a period are caused by the motion of vortices in this region:

$$\frac{1}{T}\int_0^T P\,dt=4\int_0^{\lambda}S_x x N_x f_L\,dx, \tag{15}$$

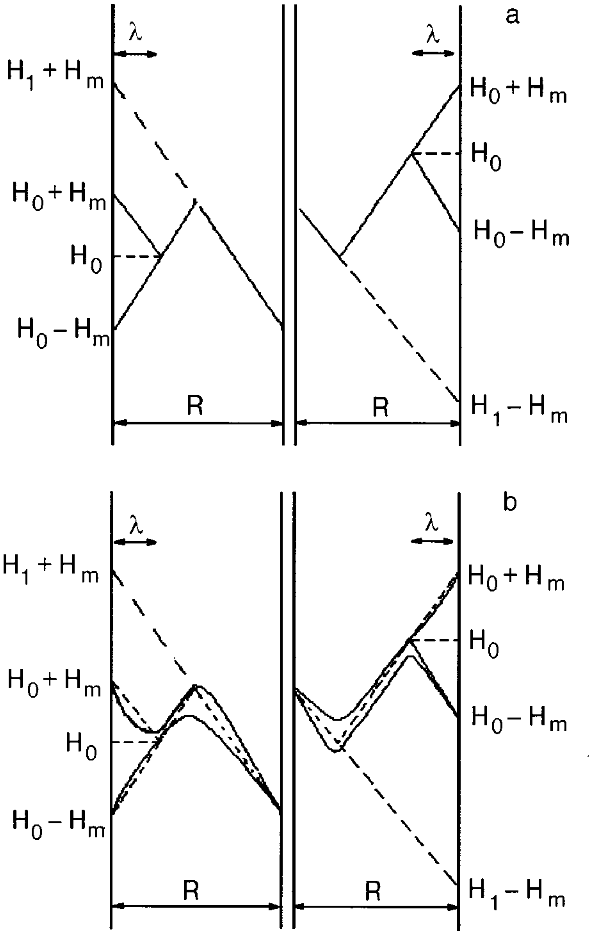

FIG. 2. Magnetic field distribution in the Bean model (a) and in the general case of the model of pinning and viscous flow of vortices (b)

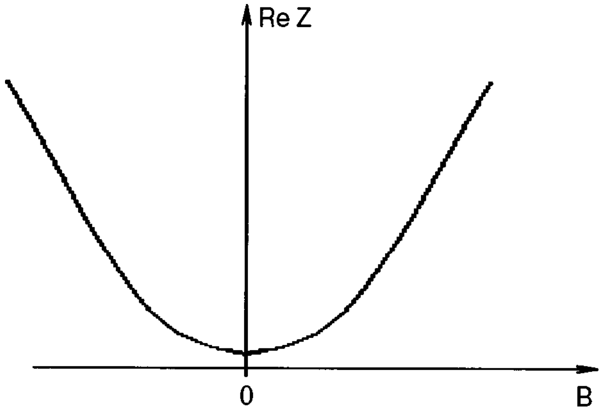

FIG. 3. Behavior of the real component of the impedance in the model of pinning and viscous flow of hypervortices.

where $S_x = 2\pi RL$ is the volume of a sector (along the radius R of the sample), $N_x = [(\lambda - x)/\lambda](H_m/\Phi_0)$ is the number of vortices at the point x, and f_L is the Lorentz force, which, according to Eq. (1), is equal to the sum of the pinning and viscous frictional forces: $f_L = j_c\Phi_0 + f_{\mathrm{fr}}$. Evaluating the integral in relation (15), we obtain

$$\frac{1}{T}\int_0^T P\,dt = \frac{4}{3}\pi R H_m^2 \lambda, \tag{16}$$

and expression (14) can be used to obtain the relations between $\operatorname{Re} Z$ and the penetration depth λ and critical current density:

$$\operatorname{Re} Z = \frac{2}{3}\lambda\frac{1}{2\pi\omega}, \tag{17}$$

$$j_c = \frac{1}{3\pi}\frac{1}{\omega}\frac{H_m}{\operatorname{Re} Z}, \tag{18}$$

where ω is the frequency of the alternating component of the magnetic field.

We note that at distances $x \leqslant \lambda$ from the surface of the superconductor, where the vortices move, the magnetic field distributions for increasing and decreasing static component of the field coincide, while in the region $\lambda \leqslant x \leqslant R$, where the distributions of the magnetic field are different, the vortices are immobile and the Lorentz force for them is equal to zero. Therefore, in the framework of the strict Bean model the dependence of the components of the surface impedance on the external static magnetic field does not exhibit hysteresis.

Let us elucidate the character of the magnetic-field dependences of the impedance components in the regime of rigid pinning. For this we substitute into relation (18) a field dependence of the critical current density in the form (10):

$$\operatorname{Re} Z(B) = \frac{1}{3\pi}\frac{1}{\omega}\frac{H_m}{j_c} = \frac{1}{3\pi}\frac{1}{\omega}\frac{H_m}{j_{c0}}\sqrt{1 + B^2/B_0^2}.$$

At values of the magnetic field which are small in comparison with the characteristic field B_0 of the medium, the field dependence of the impedance is close to parabolic, $\operatorname{Re} Z(B \ll B_0) \sim (1/3\pi j_{c0})(H_m/\omega)[1 + B^2/2B_0^2]$. At fields of the order of B_0 the real component of the impedance is a practically linear function of the static field (Fig. 3).

NUMERICAL SIMULATION

The complicated nature of the field dependence of each of the terms in relation (1) does not permit the construction of all the field dependences of the impedance components analytically. We therefore carried out a numerical simulation of the motion of the vortices in the sample. In the simulation we varied the field dependence of the critical current density $j_c(B)$ in the form (10) and the field dependence of the coefficient of viscosity $\eta(B)$ in the form (11) and calculated the magnetic-field dependences of the imaginary and real components of the surface impedance of the sample. In the case of large values of the critical current density the magnetic-field dependence of the imaginary and real components was monotonic and nonhysteretic [Fig. 4a], behavior which corresponds to the critical-state model.

As the critical current density decreases, hysteresis and nonmonotonicity arise in the dependence of the real component of the impedance on the modulus of the static magnetic field (Fig. 4b and 4c). As the critical current density decreases further [Fig. 4d] the nonmonotonicity vanishes, but the dependence exhibits significant hysteresis. It should be noted that the change in the shape of the dependence of the impedance components on the critical current density is equivalent to a change in the coefficient of viscosity. However, the trend here is opposite—the hysteresis becomes larger as the coefficient of viscosity increases.

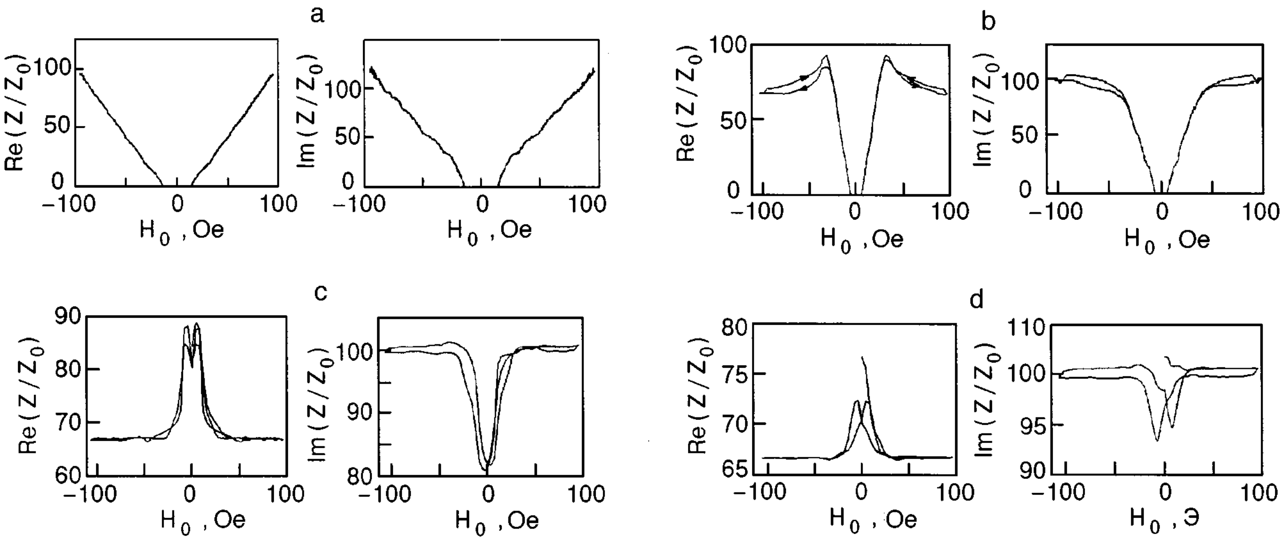

FIG. 4. Magnetic-field dependence of the real and imaginary components of the surface impedance for different values of the parameters of the medium: $j_{c0}=10^3$ A/cm^2, $H_j=10$ Oe, $\eta_0=10^{-5}$ (a); $j_{c0}=10^3$ A/cm^2, $H_j=5$ Oe, $\eta_0=10^{-4}$ (b); $j_{c0}=2\times10^2$ A/cm^2, $H_j=5$ Oe, $\eta_0=10^{-4}$ (c); $j_{c0}=10^2$ A/cm^2, $H_j=5$ Oe, $\eta_0=10^{-4}$ (d).

The appearance of hysteresis in the magnetic-field dependence of the components of the surface impedance, an effect which is not described in the strict Bean model, can be explained by proceeding from the concept of the pinning and viscous flow of hypervortices. As can be seen in Fig. 1, even at a current density j smaller than the critical value j_c, the hypervortices will move with a nonzero velocity and will be acted upon by the Lorentz force. Consequently, there will be contributions to the loss not only from the vortices located in a subsurface layer of thickness λ but from practically all the vortices in the interior of the superconductor. And, since in the case of a decreasing static component of the external magnetic field the concentration of hypervortices in the interior of the superconductor at a distance $\lambda \leqslant x \leqslant R$ from the surface is greater than in the case of an increasing static component [Fig. 2a], the real part of the surface impedance should also be larger in the case of a decreasing field than for an increasing field, and this is seen in Fig. 5.

We note that as the critical current density decreases with increasing static magnetic field, the force of viscous friction begins to play a more appreciable role in comparison with the pinning force. As a result, the distribution of the magnetic field in the interior of the superconductor loses the triangular profile that is characteristic for the strict Bean model [Fig. 2a], and that leads to a more complicated character of the magnetic-field dependence of the surface impedance.

EXPERIMENTAL INVESTIGATIONS

The inverse problem of finding the parameters of the medium (which in this case are constants of the model) from measurements of some integral quantity is in general ill-posed. A special measuring procedure is therefore required. Measurements in the low-frequency region (at frequencies of around 10–20 Hz) at small values of the alternating field require a meter with a threshold sensitivity better than 0.1 nΩ and with a precisely determined systematic error and a negligibly small random error. At large values of the alternating magnetic field the value of the imaginary component of the impedance is quite large, and its relative change as a function of the static field is less than 5%; this imposes a limitation on the resolution of the measuring apparatus. Since in the low-field limit the nonlinear response of ceramic superconductors is small, the demands imposed on the linearity of the measuring scheme are high and cannot be met by contact methods. A wide-band contactless measuring device with a low level of intrinsic noise and nonlinear distor-

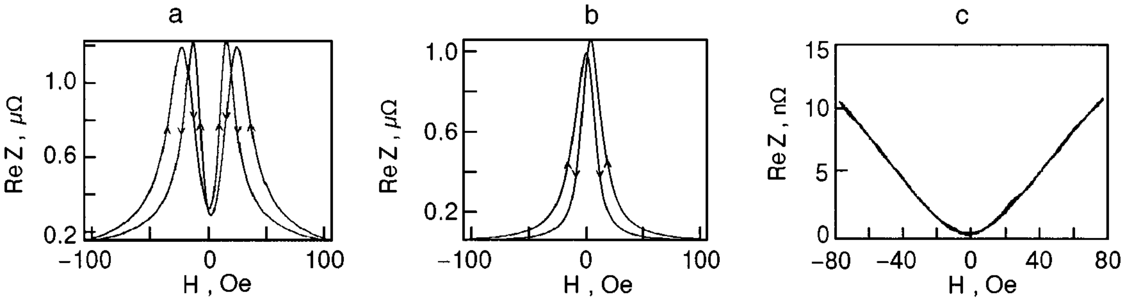

FIG. 5. Real component of the surface impedance of a YBaCuO ceramic versus the static magnetic field H for amplitudes of the alternating component of the field equal to 1 Oe (a) and 10 Oe (b) at a frequency of 663 Hz and at an amplitude of 200 mOe at a frequency of 30 Hz (c).

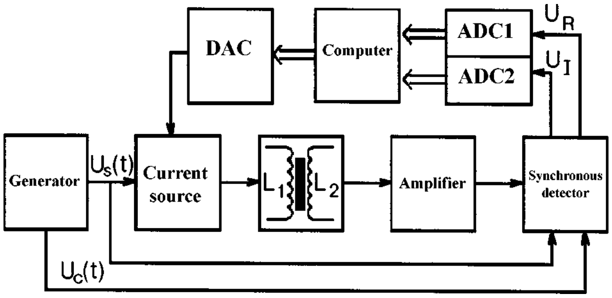

FIG. 6. Block diagram of the measurement unit.

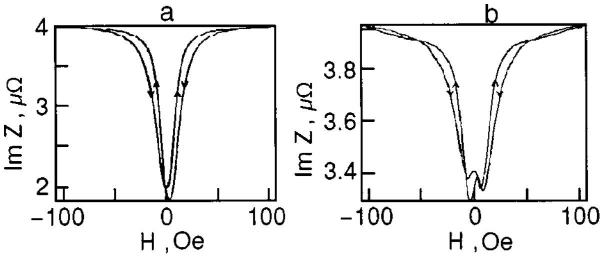

FIG. 7. Imaginary component of the surface impedance of a YBaCuO ceramic as a function of the static magnetic field H for amplitudes of the alternating component of the field equal to 4 Oe (a) and 10 Oe (b) at a frequency of the alternating field of 663 Hz.

tions is required for these studies. In order to obtain information not only about the energy of the magnetic field (which is characterized by the value of the imaginary component of the impedance) but also about the losses in the sample, both the imaginary and real components of the impedance must be measured simultaneously.

Figure 6 shows a block diagram of the program-controlled measuring unit developed here, which permits investigation of the magnetic-field dependence of the imaginary and real components of the surface impedance of cylindrical samples at constant values of the amplitude and frequency of the alternating field. The unit consists of a sensor containing the sample and a modulating coil L_1 and signal coil L_2, an analog surface impedance transducer, which includes a generator, a current source, a preamplifier, and a detector unit, and a computer-controlled registration unit that includes two analog-to-digital converters.

We note that the analog surface-impedance transducers[2] in the measuring unit can measure the dependence of the impedance components on both the modulus of the static magnetic field and on the frequency and amplitude of the alternating magnetic field. The results of a calibration on samples of an insulator, copper, and aluminum showed that the transducer error was 1% or better over the entire range of working frequencies and amplitudes of the current. The minimum measurable surface impedance, as estimated from the noise level of the preamplifier, is 5×10^{-12} Ω in a 1 Hz frequency band. The measurable ratio of the real to the imaginary part ranges from 0.01 to 100.

This measuring unit was used to investigate the behavior of the real and imaginary components of the surface impedance of samples as functions of the static component of the magnetic field at frequencies of the alternating component from 10 Hz to 1 kHz and at amplitudes of 0.1–10 Oe at liquid-nitrogen temperature. The most typical experimental magnetic-field dependences of the real and imaginary components of the impedance for different values of the frequency and amplitude of the alternating field are presented in Figs. 5 and 7. For small amplitudes of the alternating field we see that at low frequencies the magnetic-field dependence of the impedance has a monotonic, nonhysteretic character, which in the region of small values of the static field is close to parabolic, in agreement with the analytical estimates in the critical-state model. In fields of larger amplitude in the higher frequency range a nonmonotonic dependence of the real component of the impedance appears [Fig. 5a]. In the case of large amplitudes and high frequencies one again observes a monotonic dependence of both impedance components (Figs. 5 and 7). For relatively high frequencies of the alternating field the impedance components exhibit significant hysteresis (see Figs. 5a, 5b, and 7).

RESULTS AND CONCLUSIONS

To systematize the results of the measurements of the real and imaginary components of the surface impedance of HTSC ceramics, we selected certain characteristic points on the curves obtained and plotted the frequency dependence of these points on separate graphs. For both components we analyzed the values of the impedance at the extreme values of the static field (around 100 Oe) and in the neighborhood of zero.

Let us examine the behavior of the real component of the impedance divided by the frequency; the values of this normalized quantity at the selected points are plotted in Fig. 8. The extrema of the Re Z curve in the neighborhood of zero static field increase linearly with frequency [Fig. 8b]. In a static field of aroud 100 Oe the increase of Re Z with increasing frequency is faster than linear [Fig. 8a]. The form of the curves does not change as the frequency increases, but the amplitude of the change in the real component becomes smaller. Substantial changes in the shape of the curves occur when the amplitude of the alternating component of the field is changed (Fig. 9). As the amplitude is increased, the extrema in the neighborhood of zero static field converge toward a central extremum, so that these three extrema degenerate into one (see Fig. 5a and 5b).

The frequency dependence of the imaginary component of the impedance is linear in the investigated range for different amplitudes of the alternating field (Fig. 10) and, as a result, there are no changes in the shape of the curves. As the

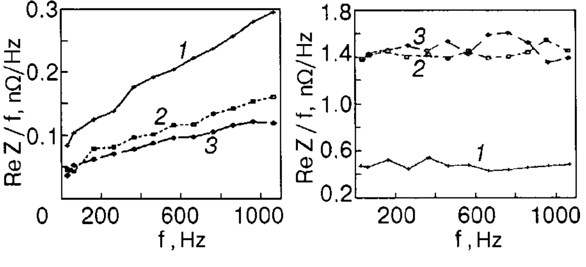

FIG. 8. Frequency dependence of the values of the real component of the surface impedance divided by the frequency, in a static field of 100 Oe (a) and in zero field (b) for various amplitudes of the alternating component of the field, Oe: 1 (*1*), 4 (*2*), and 10 (*3*).

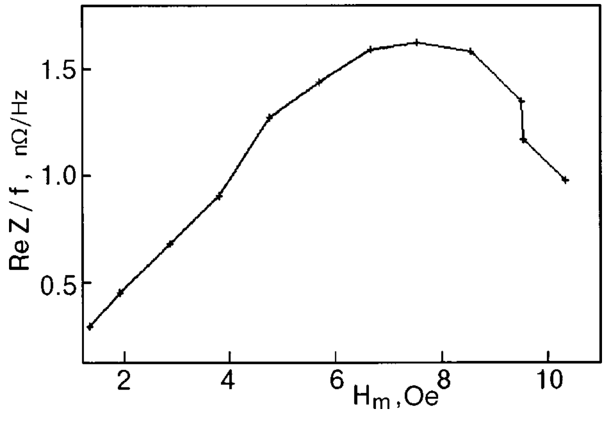

FIG. 9. Amplitude dependence of the real component of the surface impedance divided by the frequency, in zero static field and at a frequency of the alternating field of 63 Hz.

amplitude of the alternating component of the field is changed, a change in the form of the curve occurrences at large amplitudes of the alternating field [Fig. 7b]. As the amplitude increases, the central extremum degenerates, and, as a result, two more extrema appear in the neighborhood of zero.

As the static magnetic field is increased, both the imaginary and real components of the impedance go to saturation. This is most likely due to the growth of the penetration depth λ. Saturation corresponds to the complete penetration of the field into the sample, i.e., to the situation when the lattice of hypervortices completely fills the volume of the superconductor. In this case, as was shown in Ref. 8, the real component should grow faster than f and the imaginary part more slowly than f. And indeed, at large values of the static field the real component grows faster than f [Fig. 8a]. In the neighborhood of zero static field, when the vortices have not yet completely filled the volume of the sample, the frequency dependence is of a linear character [Fig. 8b].

At large amplitudes of the alternating field [Fig. 7b] certain features appear in the neighborhood of zero static field. These may be due to the fact that the measured quantity is not the impedance itself but rather

$$\tilde{Z}(H)=\frac{1}{2H_m}\int_{H-H_m}^{H+H_m} Z(\tilde{H})d\tilde{H}.$$

Thus it is clear that the measured dependence $\tilde{Z}(H)$ is closer to the impedance at small (compared to H) amplitudes H_m of the alternating field. The features can arise at large amplitudes of the alternating field because of the hysteresis in the function $Z(H)$. The hysteresis itself most likely arises on account of the specifics of the mechanism by which the field penetrates into the sample. When the field is increasing, the whole lattice of hypervortices is shifted into the interior of the sample, whereas when the field is decreasing, the changes occur in the subsurface region of the sample (Fig. 2).

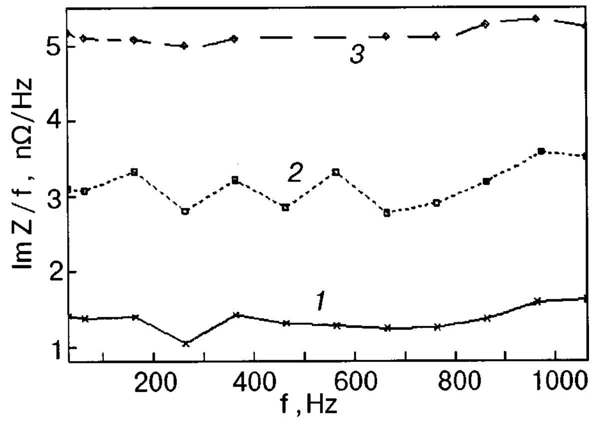

FIG. 10. Frequency dependence of the values of the imaginary component of the surface impedance divided by the frequency, in the neighborhood of zero field and for various amplitudes of the alternating field, Oe: 1 (*1*), 4 (*2*), and 10 (*3*).

An analytical examination and a numerical simulation of the dynamics of hypervortices in HTSCs in the framework of the pinning and viscous flow model predict a hysteretic character of the magnetic-field dependence of the surface impedance, in which the real component should be larger when the static component is decreasing in modulus than when it is increasing, and this is confirmed by experiment (Fig. 5). Relations (17) and (18) can be used to develop a technique of determining the parameters of the model from the experimental curves of the impedance. The experimental results show that the field dependence of the critical current density is well described by the model (10) [see Figs. 3 and 5a].

Analysis of the experimental data can reveal the boundaries of the domain of applicability of the critical-state model of ceramic superconductors. This model typifies the rigid pinning regime and does not permit a description of hysteresis in the magnetic-field dependence of the impedance components (even when the hysteresis of $B(H)$ is taken into account). For a YBaCuO ceramic sample prepared according to the standard technology, this regime is observed at frequencies up to 35 Hz at amplitudes of the alternating field less than 0.3 Oe. On the basis of an analysis of the results of a numerical simulation in the model of pinning and viscous flow of hypervortices, one can infer the existence of an important nonhysteretic regime at higher frequencies and small amplitudes of the alternating field, as are typical for practical applications in radio electronics. The presence of this regime for ceramic superconductors at working temperatures of around 77 K would significantly broaden the domain of application of ceramic superconductors.

A comparative analysis of the results of the numerical and analytical modeling with the experimentally obtained frequency and magnetic-field dependences of the impedance components shows that the model of pinning and viscous flow of hypervortices provides an adequate description of the low-field electrodynamics of ceramic superconductors over the entire frequency range. In the low-frequency range the proposed model is the same as the critical-state model and predicts a nonhysteretic, close to parabolic, character of the magnetic-field dependence of the surface impedance, in agreement with the experiments of a number of authors. In the high-frequency range the model correctly describes the features of the magnetic-field curves, including hysteresis.

This study was supported by the Government Program of the Russian Federation, ''Topical Problems in Condensed-Matter Physics,'' in the ''Superconductivity'' section.

[*] E-mail: ignatjev@zmail.ru

---

[1] V. F. Masterov, in *High-Temperature Superconductivity* [collected articles, in Russian], Mashinostroenie, Leningrad (1990).
[2] V. K. Ignat'ev and I. V. Neginskiĭ, Prib. Tekh. Éksp. , No. 2, 60 (1998).
[3] V. K. Ignat'ev, Author's Abstract of Doctoral Dissertation [in Russian], Moscow (1997).
[4] É. B. Sonin, JETP Lett. **47**, 496 (1988).
[5] P. W. Anderson and Y. B. Kim, Rev. Mod. Phys. **36**, 39 (1964).
[6] V. V. Shmidt, *The Physics of Superconductors: Introduction to Fundamentals and Applications* [Springer-Verlag, New York (1997); Nauka, Moscow (1982)].
[7] V. K. Ignat'ev, Élektromekhanika, No. 3, 11 (1998).
[8] L. M. Fisher, N. V. Il'in, I. F. Voloshin, N. M. Makarov, V. A. Yampol'skii, F. P. Rodriguez, and R. L. Snyder, Physica C **206**, 195 (1993).

Translated by Steve Torstveit

LOW TEMPERATURE MAGNETISM

On the influence of higher invariants of the thermodynamic potential on the onset of long-period magnetic structures

Yu. D. Zavorotnev* and L. I. Medvedeva

A. A. Galkin Donetsk Physics and Technology Institute, National Academy of Sciences of Ukraine, ul. R. Lyuksemburg 72, 83114 Donetsk, Ukraine

E. P. Stefanovskiĭ**

Department of Physics, Ben-Gurion University of the Negev, P.O.B. 653, Beer-Sheva 84 105, Israel

(Submitted June 21, 1999; revised November 26, 1999)
Fiz. Nizk. Temp. **26**, 350–354 (April 2000)

The formation of superstructures is considered with allowance for the biquadratic exchange interaction. It is shown that in this case the simultaneous coexistence of several long-period structures is possible, which can arise as a result of a first- or second-order phase transition.

Since the time when Villain,[1] Kaplan,[2] and Yoshimori[3] called attention to the possibility of a new type of magnetic ordering (different from ferro-, antiferro-, and ferrimagnetic), viz., modulated magnetic structures (MMS), whose spatial period is incommensurate with the spatial period of the crystal lattice, questions pertaining to the conditions for their onset and stability have been the subject of a rather large number of theoretical and experimental papers. Since our subject here will be matters pertaining to the phenomenological theory of MMS (magnetic structures of this kind are often called long-period or incommensurate magnetic phases), we must first mention the fundamental paper by Dzyaloshinskiĭ,[4] which is devoted to the phenomenological theory of the so-called exchange long-period magnetic structures (see also the reviews[5,6] and the monograph[7]). This theory, for example, provides an explanation for the occurrence of an incommensurate magnetic phase in the compound β-MnO$_2$. The Dzyaloshinskiĭ theory was subsequently[8] extended to MMS of exchange–relativistic origin and is reflected in the explanation of the occurrence of long-period magnetic structures in the systems MnSi, FeGe, and CsCuCl$_3$ (Refs. 9 and 10). Somewhat later[11–16] (see also Ref. 6) a phenomenological theory of the origin of the exchange and exchange–relativistic modulated magnetic structures was constructed, differing from the Dzyaloshinskiĭ theory and explaining the magnetic structures of a significant number of magnetically ordered crystals, such as Cr$_2$BeO$_4$, TbAsO$_4$, MnOOH, MnP, Mn$_3$B$_4$, etc. The onset of this kind of magnetic structures is due to a competition of magnetic interactions of various origins. For example, the coexistence of the so-called exchange MMS is due to the competition of the exchange interactions (see, e.g., Refs. 4, 13, and 14), while that of exchange–relativistic MMS is due to a competition of the exchange and exchange–relativistic interactions, respectively (see, e.g., Refs. 6, 15, and 16). We will be interested in the so-called ‘‘symmetry-dependent’’ MMS (see Refs. 4–8 and 10–16). From the standpoint of the phenomenological theory of magnetism the origin of this kind of MMS is due to the presence in the nonequilibrium thermodynamic potential (NTDP) of invariants linear in the first spatial derivatives of the irreproducible magnetic vectors (IMV) (the moments of the spin density), which describe the magnetic system, and their competition with the invariants which are quadratic in these derivatives (the symmetry conditions for the existence of such invariants are explained in the papers by Dzyaloshinskiĭ[4]).

The authors of the papers cited above, in discussing the conditions for the onset and stability of MMS of this kind, limited consideration to invariants of no higher than second degree in the IMV and the NTDP. However, the inclusion of invariants of higher degrees in the IMV can substantially disrupt the picture of phase transitions in the system, i.e., can alter the conditions for the onset of MMS. Therefore, generally speaking, one is justified in raising the question of the influence of the higher invariants on the conditions for the onset of MMS. In this paper we limit consideration to taking into account additional spatially homogeneous invariants of the fourth degree in systems with a triangular distribution of magnetic moments of the ions in the magnetic unit cell, e.g., in Fe$_2$P.

Thus we consider a ‘‘symmetry-dependent’’ MMS of exchange origin in the Fe$_2$P system.[17] As was shown in Ref. 18, in this case the following expression for the density of the NTDP in the exchange approximation:

$$\Phi=\delta_1\mathbf{F}^2+\delta_2(\mathbf{L}_1^2+\mathbf{L}_2^2)+\Delta\left(\mathbf{F}\frac{\partial\mathbf{L}_1}{\partial x}-\mathbf{L}_1\frac{\partial\mathbf{F}}{\partial x}+\mathbf{F}\frac{\partial\mathbf{L}_2}{\partial y}-\mathbf{L}_2\frac{\partial\mathbf{F}}{\partial y}\right)+\alpha_1\left(\frac{\partial\mathbf{F}}{\partial x}\right)^2+\alpha_2\left(\frac{\partial\mathbf{L}_1}{\partial x}\right)^2+\beta\mathbf{F}^2(\mathbf{L}_1^2+\mathbf{L}_2^2)+\alpha_3\mathbf{F}^4+\alpha_4(\mathbf{L}_1^4+\mathbf{L}_2^4)+\alpha_5\left(\frac{\partial\mathbf{F}}{\partial y}\right)^2+\alpha_6\left(\frac{\partial\mathbf{L}_2}{\partial y}\right)^2, \quad (1)$$

where

$$\mathbf{F}=\mathbf{S}_1+\mathbf{S}_2+\mathbf{S}_3,\quad \mathbf{L}_1=6^{-1/2}(2\mathbf{S}_1-\mathbf{S}_2-\mathbf{S}_3),$$

$$\mathbf{L}_2=2^{1/2}(\mathbf{S}_2-\mathbf{S}_3)$$

are the irreducible ferro- and antiferromagnetic vectors, respectively, $\mathbf{S}_i$ $(i=1,2,3)$ is the spin vector of the ith ion, $\delta_1=\beta_1(T-T_C)$; $\delta_2=\beta_2(T-T_N)$, Δ, α_i $(i=1,2,3,4,5,6)$, β, β_1, and β_2 are phenomenological coefficients, with $\alpha_3>0$, $\alpha_4>0$; T_C and T_N are the Curie and Néel temperatures, respectively. We emphasize that the irreducible magnetic vectors $\mathbf{F}$ and $(\mathbf{L}_1,\mathbf{L}_2)$ (see Ref. 18) transform according to different irreducible representations of the symmetry space group of the $\mathrm{Fe_2P}$ system, i.e., the onset of MMS in this case is due to the phenomenological mechanism proposed in Refs. 11–16 (see also Ref. 6). We are interested only in spatially homogeneous equilibrium magnetic states.

Minimizing the functional corresponding to (1) gives incommensurate structures with propagation vectors along the $0X$ and $0Y$ axes, respectively. In the first of these there is a rotation of the irreducible vectors $\mathbf{F}$ and $\mathbf{L}_1$, and in the second, of $\mathbf{F}$ and $\mathbf{L}_2$. For simplicity we consider a superstructure with a propagation vector directed along the $0X$ axis. We then have the following system of Euler's equations in a Cartesian coordinate system $(L_1=L)$:

$$\begin{cases} \alpha_1F_z''-\Delta L_z'-(\delta_1+2\alpha_3F^2+\beta L^2)F_z=0 \\ \alpha_2L_z''+\Delta F_z'-(\delta_2+2\alpha_4L^2+\beta F^2)L_z \\ \alpha_1F_y''-\Delta L_y'-(\delta_1+2\alpha_3F^2+\beta L^2)F_y=0' \\ \alpha_2L_y''+\Delta F_y'-(\delta_2+2\alpha_4L^2+\beta F^2)L_y=0 \end{cases} \tag{2}$$

where $F_i'=\partial F_i/\partial x$; $F_i''=\partial^2F_i/\partial x^2$ $(i=y,z)$. It follows from (2) that for $\beta=0$ the system decomposes into two independent subsystems for the Z and Y components of the irreducible vectors. In a theory making use of the approximation of constant moduli of the irreducible vectors,[3–6] these two subsystems are coupled by means of a decrease in the number of independent variables from two to one. Taking this approximation, we obtain

$$F_z=F\cos(kx)\quad L_z=L\cos(kx-\gamma)$$

$$F_y=F\sin(kx)\quad L_y=L\sin(kx-\gamma). \tag{3}$$

As was shown in Ref. 13, in the cases $\Delta<0$ and $\Delta>0$ we have $\gamma=\pi/2$ and $\gamma=-\pi/2$, respectively. For the sake of definiteness we assume below that $\Delta<0$. Substituting (3) into (2), we obtain

$$\begin{cases} k^2\alpha_1F-|\Delta|kL+(\delta_1+2\alpha_3F^2+\beta L^2)F=0 \\ k^2\alpha_2L-|\Delta|kF+(\delta_2+2\alpha_4L^2+\beta F^2)L=0^{\cdot} \end{cases} \tag{4}$$

Let us consider the solution of this system under the condition that $T_N<T_C$, $\delta_2>0$, and $T\approx T_C$. Then the F^4 term in the thermodynamic potential will be large. Making use of this circumstance, we can set $\alpha_4=0$ in (4). Eliminating the variable L from the system, we obtain

$$\begin{aligned} &2\alpha_3\beta^2F^6+\beta[4\alpha_3(\alpha_2k^2+\delta_2)+\beta(\alpha_1k^2+\delta_1)]F^4 \\ &\quad+2(\alpha_2k^2+\delta_2)[\alpha_3(\alpha_2k^2+\delta_2)+\beta(\alpha_1k^2+\delta_1)]F^2 \\ &\quad+[(\alpha_2k^2+\delta_2)^2(\alpha_1k^2+\delta_1)-\Delta^2k^2(\alpha_2k^2+\delta_2)]=0. \end{aligned} \tag{5}$$

Let us make a qualitative analysis of this bicubic equation, using the fact, known from the theory of algebraic equations, that the number of positive solutions is equal to the number of sign changes in the sequence of coefficients of the equation.

1. $\delta_1>0$, $\beta>0$.

Then, if

a) $(\alpha_2k^2+\delta_2)(\alpha_1k^2+\delta_1)-\Delta^2K^2>0$, there will be no change of sign in the sequence of coefficients in Eq. (5), and, consequently, no positive solutions for F^2;

b) $(\alpha_2k^2+\delta_2)(\alpha_1k^2+\delta_1)-\Delta^2k^2<0$, there is one sign change in the sequence of coefficients and, accordingly, one solution (one MMS structure). It follows that an incommensurate structure can arise both above and below the Curie temperature.

2. $\delta_1<0$, $\beta>0$. Then, if $\alpha_1k^2+\delta_1>0$, the result will be the same as for condition 1. If $\alpha_1k^2+\delta_1<0$ there are two possible cases:

a) $\alpha_3(\alpha_2k^2+\delta_2)+\beta(\alpha_1k^2+\delta_1)>0$; there is one solution, and

b) $\alpha_3(\alpha_2k^2+\delta_2)+\beta(\alpha_1k^2+\delta_1)<0$; regardless of the sign of the expression multiplying F^4 there is only one sign change, and one solution.

3. $\delta_1>0$, $\beta<0$. The following situations are possible:

a) $(\alpha_1k^2+\delta_1)(\alpha_2k^2+\delta_2)-\Delta^2k^2>0$; for any sign of the expression $\alpha_3(\alpha_2k^2+\delta_2)+\beta(\alpha_1k^2+\delta_1)$ there are two sign changes, and this will possibly give two superstructures if the stability conditions hold;

b) $(\alpha_1k^2+\delta_1)(\alpha_2k^2+\delta_2)-\Delta^2k^2<0$; in this case for $\alpha_3(\alpha_2k^2+\delta_2)+\beta(\alpha_1k^2+\delta_1)>0$ three solutions are possible. If $\alpha_3(\alpha_2k^2+\delta_2)+\beta(\alpha_1k^2+\delta_1)<0$, then regardless of the sign of the expression multiplying F^4 there is only one solution.

4. $\delta_1<0$, $\beta<0$.

a) $\alpha_1k^2+\delta_1>0$; the result is the same as in case 3.

b) $\alpha_1k^2+\delta_1<0$; in this case there are three sign changes and three positive solutions for F^2.

It should be emphasized that some of the predicted states may not appear, if the stability condition does not hold for them. It follows from what we have said that additional solutions arise only on account of the presence of the invariant $\mathbf{F}^2(\mathbf{L}_1^2+\mathbf{L}_2^2)$, and they all have the same value of the wave vector but different values of F and L. However, structures with different values of k can arise. As an illustration, let us consider the limiting case $\alpha_3=\alpha_4=0$.

The solution of system (4) can be written in the form

$$F^2=-\frac{1}{\beta}\left(\frac{k^2\alpha_2+\delta_2}{k^2\alpha_1+\delta_1}\right)^{1/2}\times\{\sqrt{(k^2\alpha_1+\delta_1)(k^2\alpha_2+\delta_2)}\pm|k\Delta|\},$$

$$L^2=-\frac{1}{\beta}\left(\frac{k^2\alpha_1+\delta_1}{k^2\alpha_2+\delta_2}\right)^{1/2}\times\{\sqrt{(k^2\alpha_1+\delta_1)(k^2\alpha_2+\delta_2)}\pm|k\Delta|\}. \tag{6}$$

To find the wave vector we must minimize the potential with respect to k. We then have the third equation of the system:

$$\Delta FL+k(\alpha_1F^2+\alpha_2L^2)=0. \tag{7}$$

From the two solutions (6) for $\beta > 0$ we must keep only the one with the negative sign in front of $|k\Delta|$. It is obvious that in order for a superstructure to exist, the following condition must be satisfied:

$$0 \leqslant (k^2\alpha_1 + \delta_1)(k^2\alpha_2 + \delta_2) < k^2\Delta^2. \tag{8}$$

In a theory that does not take into account the presence of the invariant F^2L^2, the wave vector $\mathbf{k}$ is determined from the relation[6]

$$(k^2\alpha_1 + \delta_1)(k^2\alpha_2 + \delta_2) = k^2\Delta^2. \tag{9}$$

Then in our case the condition $F^2 = L^2 = 0$ holds, and there is no superstructure. To find the modulus of the propagation vector we have the equation

$$4\alpha_1^2\alpha_2^2k^6 + \alpha_1\alpha_2[4\alpha_1\delta_2 + 4\delta_2\delta_1 - \Delta^2]k^4 + [(\alpha_1\delta_2 + \alpha_2\delta_1)^2 - \Delta^2(\alpha_1\delta_2 + \alpha_2\delta_1)]k^2 - \Delta^2\delta_1\delta_2 = 0, \tag{10}$$

which is cubic with respect to k^2.

For the sake of definiteness we consider the case $T_N < T < T_C$. Then $\delta_1 < 0$, $\delta_2 > 0$. Consequently, nontrivial solutions arise in two cases:

$$1)\ \frac{\delta_1}{\alpha_1} + \frac{\delta_2}{\alpha_2} < \frac{\Delta^2}{4\alpha_1\alpha_2}, \tag{11}$$

$$2)\ (\alpha_1\delta_2 + \alpha_2\delta_1)^2 - \Delta^2(\alpha_1\delta_2 + \alpha_2\delta_1) < 0. \tag{12}$$

The latter relation can hold only when the temperature T lies in the interval $[T_C, T_N]$ and the following double inequality holds:

$$0 < \frac{\delta_1}{\alpha_1} + \frac{\delta_2}{\alpha_2} < \frac{\Delta^2}{\alpha_1\alpha_2}. \tag{13}$$

The right-hand condition in (13) is less stringent than (11); it is analogous to the requirement imposed on the temperatures T_C and T_N in the theory with $\beta = 0$, viz., that these temperatures not be too far apart.[6]

It follows from what we have said that for $T_N < T < T_C$ a superstructure can exist only in the temperature interval specified by the relations

$$(\alpha_1\beta_2T_N + \alpha_2\beta_1T_C) < (\alpha_1\beta_2 + \alpha_2\beta_1)T < (\alpha_1\beta_2T_N + \alpha_2\beta_1T_C) + \Delta^2. \tag{14}$$

It should be noted that for $\delta_1 = 0$ there is always a solution with $k = 0$, and there is one solution with $k^2 > 0$ when condition (13) holds. This means that for $T = T_C$ there can be both a first-order phase transition with a jump in k^2 and a second-order phase transition. When the stability conditions hold, this can make for the existence of two superstructures with different wave vectors. Consequently, taking the biquadratic exchange interaction into account leads to the possibility of formation of an incommensurate structure as a result of a second-order phase transition.

Upon reaching the lower temperature boundary determined by condition (13), the spiral vanishes, and it appears anew at a temperature $T < T_N < T_C$, since then the quantity $(\delta_1\delta_2)$ will be positive, and there are three sign changes in the sequence of coefficients in Eq. (10). This means that three superstructures with different values of the wave vector can arise, with the sole restriction (8).

In the case $\beta < 0$ one solution of system (4) always exists, and a second exists under the condition

$$k^2\Delta^2 < (k^2\alpha_1 + \delta_1)(k^2\alpha_2 + \delta_2), \tag{15}$$

which can hold if both factors on the right-hand side of (15) have the same sign. This implies the two systems of relations

$$\begin{cases} T > T_C - k^2\alpha_1/\beta_1 \\ T > T_N - k^2\alpha_2/\beta_2, \end{cases} \quad \begin{cases} T < T_C - k^2\alpha_1/\beta_1 \\ T < T_N - k^2\alpha_2/\beta_2, \end{cases} \tag{16}$$

which show that the formation of a second superstructure for $T_N < T_C$ is possible in a narrow temperature band below T_C and everywhere below $T_N - k^2\alpha_2/\beta_2$. The value of the wave vector in this case is also determined by relation (10).

If $T \approx T_N$ and $\delta_1 < 0$, then one can set $\alpha_3 = 0$ in the thermodynamic potential. Then for determining the value of k we have the equation

$$2\alpha_4\beta^2L^6 + \beta[4\alpha_4(\alpha_1k^2 + \delta_1) + \beta(\alpha_2k^2 + \delta_2)]L^4 + 2(\alpha_1k^2 + \delta_1)(\alpha_4(\alpha_1k^2 + \delta_1) + \beta(\alpha_2k^2 + \delta_2))L^2 + [(\alpha_1k^2 + \delta_1)^2(\alpha_2k^2 + \delta_2) - \Delta^2k^2(\alpha_1k^2 + \delta_1)] = 0. \tag{17}$$

Let us consider the following cases:

1. $\beta > 0$, $\alpha_1k^2 + \delta_1 > 0$, $\delta_2 > 0$.

a) $(\alpha_1k^2 + \delta_1)^2 - \Delta^2k^2 > 0$; there are no solutions;

b) $(\alpha_1k^2 + \delta_1)^2 - \Delta^2k^2 < 0$; there is one solution.

2. $\beta > 0$, $\alpha_1k^2 + \delta_1 < 0$, $\delta_2 > 0$.

a) $(\alpha_1k^2 + \delta_1)^2 - \Delta^2k^2 > 0$; there are two solutions, provided that at least one of the expressions for L^2 or L^4 in Eq. (17) is negative;

b) $(\alpha_1k^2 + \delta_1)^2 - \Delta^2k^2 < 0$; there is only one solution.

3. $\beta > 0$, $\alpha_1k^2 + \delta_1 < 0$, $\delta_2 < 0$, $\alpha_2k^2 + \delta_2 < 0$.

a) $(\alpha_1k^2 + \delta_1)^2 - \Delta^2k^2 > 0$; there are two solutions under the condition $4\alpha_4(\alpha_1k^2 + \delta_1) + \beta(\alpha_2k^2 + \delta_2) < 0$;

b) $(\alpha_1k^2 + \delta_1)^2 - \Delta^2k^2 < 0$; there are three solutions if $4\alpha_4(\alpha_1k^2 + \delta_1) + \beta(\alpha_2k^2 + \delta_2) < 0$.

4. $\beta < 0$, $\alpha_1k^2 + \delta_1 > 0$, $\delta_2 > 0$.

a) $(\alpha_1k^2 + \delta_1)^2 - \Delta^2k^2 > 0$; there are two solutions;

b) $(\alpha_1k^2 + \delta_1)^2 - \Delta^2k^2 < 0$; there are either two solutions or one solution, depending on the signs of the quantities multiplying L^2 and L^4.

5. $\beta < 0$, $\alpha_1k^2 + \delta_1 < 0$, $\delta_2 > 0$.

a) $(\alpha_1k^2 + \delta_1)^2 - \Delta^2k^2 > 0$; there are no solutions;

b) $(\alpha_1k^2 + \delta_1)^2 - \Delta^2k^2 < 0$; there is one solution.

6. $\beta < 0$, $\alpha_1k^2 + \delta_1 < 0$, $\delta_2 < 0$, $\alpha_2k^2 + \delta_2 < 0$.

a) $(\alpha_1k^2 + \delta_1)^2 - \Delta^2k^2 > 0$; at relatively small values of β, such that the coefficients of L^2 and L^4 are positive, there are no solutions. As β increases, one or both of these expressions changes sign, and two solutions exist.

b) $(\alpha_1k^2 + \delta_1)^2 - \Delta^2k^2 < 0$; there is one solution at any value of β.

It is clear from what we have said that for $T \approx T_N$ the appearance of additional aperiodic structures is also due to the presence of a mixed invariant $\mathbf{F}^2\mathbf{L}^2$. Consequently, in crystals with biquadratic exchange there can be several superstructures.

We thank I. E. Chupis for a discussion of this study and for valuable comments.

*E-mail: zavorot@host.dipt.donetsk.ua
**E-mail: stefan@bgumail.bgu.ac.il

---

[1] T. Villain, Phys. Chem. Solids **11**, 303 (1959).
[2] T. A. Kaplan, Phys. Rev. **116**, 888 (1959).
[3] A. Yoshimori, J. Phys. Soc. Jpn. **14**, 807 (1959).
[4] I. E. Dzyaloshinskiĭ, Zh. Éksp. Teor. Fiz. **46**, 1420 (1964) [Sov. Phys. JETP **19**, 960 (1964)].
[5] Yu. A. Izyumov, Usp. Fiz. Nauk **144**, 439 (1984) [Sov. Phys. Usp. **27**, 845 (1984)].
[6] V. G. Bar'yakhtar and E. P. Stefanovskiĭ, Fiz. Nizk. Temp. **22**, 904 (1996) [Low Temp. Phys. **22**, 693 (1996)].
[7] Yu. A. Izyumov, *Neutron Diffraction on Long-Period Structures* [in Russian], Énergoizdat, Moscow (1987).
[8] V. G. Bar'yakhtar and E. P. Stefanovskiĭ, Fiz. Tverd. Tela (Leningrad) **11**, 1946 (1969) [Sov. Phys. Solid State **11**, 1566 (1969)].
[9] P. Bak and M. H. Jensen, J. Phys. C **13**, 1881 (1980).
[10] A. L. Alistratov, E. P. Stefanovskiĭ, and D. A. Yablonskiĭ, Fiz. Nizk. Temp. **16**, 1306 (1990) [Sov. J. Low Temp. Phys. **16**, 749 (1990)].
[11] T. K. Soboleva and E. P. Stefanovskiĭ, Fiz. Tverd. Tela (Leningrad) **23**, 2866 (1981) [Sov. Phys. Solid State **23**, 1675 (1981)].
[12] T. K. Soboleva and E. P. Stefanovskiĭ, Fiz. Met. Metalloved. **54**, 186 (1982).
[13] V. G. Bar'yakhtar, E. P. Stefanovskiĭ, and D. A. Yablonskiĭ, JETP Lett. **42**, 317 (1985).
[14] V. G. Bar'yakhtar, E. P. Stefanovskiĭ, and D. A. Yablonskiĭ, Fiz. Tverd. Tela (Leningrad) **28**, 504 (1986) [Sov. Phys. Solid State **28**, 281 (1986)].
[15] E. P. Stefanovskiĭ, Fiz. Tverd. Tela (Leningrad) **28**, 3452 (1986) [Sov. Phys. Solid State **28**, 1941 (1986)].
[16] E. P. Stefanovskiĭ, Fiz. Nizk. Temp. **13**, 740 (1987) [Sov. J. Low Temp. Phys. **13**, 424 (1987)].
[17] H. Fujii, T. Hokabe, K. Eguchi, H. Fujiwara, and T. Okamoto, J. Phys. Soc. Jpn. **51**, 414 (1982).
[18] D. A. Yablonsky and L. I. Medvedeva, Physica B **167**, 125 (1990)

Translated by Steve Torstveit

LOW TEMPERATURE PHYSICS VOLUME 26, NUMBER 4 APRIL 2000

NMR of ^{57}Fe in RFe$_{1-x}$Mn$_x$O$_3$ orthoferrites

A. S. Karnachev,* Yu. I. Klechin, A. A. Prokhorov, and E. E. Solov'ev

A. A. Galkin Donetsk Physics and Technology Institute, National Academy of Sciences of Ukraine, ul. R. Lyuksemburg 72, 83114 Donetsk, Ukraine

(Submitted July 20, 1999; revised December 3, 1999)
Fiz. Nizk. Temp. **26**, 355–362 (April 2000)

The spin echo method is used to investigate the NMR spectrum of the ^{57}Fe nuclei in manganese-substituted Tm and Er orthoferrites. It is shown that the Jahn–Teller effect for the Mn^{3+} impurity ion is manifested in a proportional enhancement of the *E*-type deformation of the Fe$^{3+}-6$O^{2-} octahedron. In the region of the spin-reorientation transition a magnetic inequivalence of the sublattices is observed both for the Fe^{3+} ions and for the Mn^{3+} impurity ions. © *2000 American Institute of Physics.* [S1063-777X(00)00504-1]

INTRODUCTION

The orthoferrites RFe$_{1-x}$Mn$_x$O$_3$ with a variable Mn concentration are interesting objects in which to study the influence of the Jahn–Teller ions Mn^{3+} on the magnetic properties and spin-reorientation transitions. These compounds have a slightly distorted perovskite structure (space group $D_{2h}^{16}-P_{bnm}$; Refs. 1 and 2). The magnetic ordering of the *d* sublattice is characterized by the possible magnetic configurations of three types:[3] $\Gamma_1(A_z, G_y, C_z)$, $\Gamma_2(F_x, C_y, G_z)$, and $\Gamma_4(G_x, A_y, F_z)$ with basis vectors **F** (ferromagnetism) and **G**, **C**, **A** (antiferromagnetism), with $F, C, A \ll G$ (Ref. 4), which indicates a *G*-type structure.

Studying the NMR spectra of ^{57}Fe in rare-earth orthoferrites[5,6] yields information not only about the values of the local fields, their temperature dependence, and the anisotropy of the hyperfine (HF) interactions,[7] but also about the magnetic state of the Fe sublattice and the spin-reorientation (SR) transitions. For example, it was the NMR method that first clearly revealed evidence of the magnetic inequivalence of the sublattices of the Fe^{3+} ions in the region of the SR transition.[5,6]

Of particular interest is the study of the NMR of ^{57}Fe in substituted orthoferrites, where it become possible to study the magnetic and hyperfine interactions of the impurity and host, and also the influence of the impurity on the phase transitions.

Substitution of the Jahn–Teller ions Mn^{3+} for Fe^{3+} in orthoferrites leads to a substantial change in the main characteristics — the magnetization, magnetic anisotropy, and exchange interactions, to some modification of the existing SR transitions, and to new transitions, in particular, transitions of the Morin type in YFe$_{1-x}$Mn$_x$O$_3$ (Ref. 3).

JAHN–TELLER EFFECT AND THE GROUND STATE OF THE Mn^{3+} ION

In this paper we investigate the influence of the Jahn–Teller ions Mn^{3+} on the NMR spectrum of ^{57}Fe in Er and Tm orthoferrites. The difference between the transferred (indirect) HF interactions in the ^{57}Fe–O^{2-}–Fe^{3+} and ^{57}Fe–O^{2-}–Mn^{3+} chains causes the NMR spectrum to become more complicated — in addition to the main lines, corresponding to an impurity-free nearest-neighbor environment of the ^{57}Fe nucleus, three satellites appear, in accordance with the three inequivalent positions of the Mn^{3+} impurity ion in the nearest-neighbor environment of ^{57}Fe (Fig. 1). The position of these satellites relative to the main line depends substantially on the ground state of the Mn^{3+} ion in RFeO$_3$.

The Jahn–Teller ion Mn^{3+} with electronic configuration of unfilled shells $t_{2g}^3 e_g^1$ in the octahedral field has a twofold orbitally degenerate ground state ^5E. The orbital degeneracy can be lifted either by the Jahn–Teller effect or on account of the pre-existing noncubic distortions in complexes of the Mn$^{3+}-6$O^{2-} type. Here the ground state wave function can be represented as a linear combination of the *E*-type functions $|E0\rangle$ and $|E2\rangle$, which, with allowance for the coupling of the quasimoments of the t_{2g} and e_g shells in the Mn^{3+} ion, correspond to the $d_{x^2-y^2}$ and d_{z^2} states of the e_g electron:

$$\Psi_{\text{base}} = \cos\alpha|E0\rangle + \sin\alpha|E2\rangle, \tag{1}$$

where α is some angle; the ^5E state of the Mn^{3+} ion is obtained as a result of the coupling of the $^4A_2$ term of the

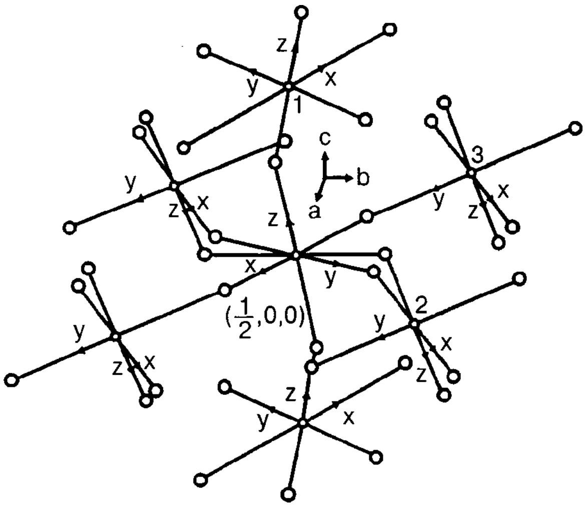

FIG. 1. Geometry of the Fe$^{3+}-$O$^{2-}-$Fe$^{3+}-$O^{2-} bonds in the orthoferrites RFeO$_3$. The orientation of the local axes is shown for each complex.

TABLE I. Theoretically predicted values of the parameter α for the Mn^{3+} ion in $RFeO_3$.

R	Pr	Nd	Sm	Eu	Gd	Tb	Dy	Y	Ho	Er	Tm	Yb	Lu
α, deg	−11	−16	−24	−20	−17	−25	−25	−28	−28	−31	−32	−36	−42

configuration t_{2g}^3 and the ^2E term of the configuration e_g^1. Thus in the state $|^5E0\rangle$ the electron is found in the $d_{x^2-y^2}$ orbital, while in the state $|^5E2\rangle$ it is found in the d_{z^2} orbital. The value of the angle α and, hence, the form of the wave function Ψ_{bas} can be related in the linear approximation with deformations of the $Mn^{3+}-6O^{2-}$ complex. For this it is convenient to go from the strain tensor ε_{ij} to its irreducible components of the E and T_2 types:

$$\varepsilon_0^E=\frac{1}{\sqrt{6}}(2\varepsilon_{zz}-\varepsilon_{xx}-\varepsilon_{yy});\quad \varepsilon_2^E=\frac{1}{\sqrt{2}}(\varepsilon_{xx}-\varepsilon_{yy})$$

$$\varepsilon_{-1}^{T_2}=-2\varepsilon_{xz},\quad \varepsilon_{+1}^{T_2}=2\varepsilon_{yz};\quad \varepsilon_2^{T_2}=-\sqrt{2}\,\varepsilon_{xy}. \tag{2}$$

Naturally, the form of Ψ_{base} will be determined solely by deformations of the E type, and it is easy to show that

$$\cos 2\alpha=\frac{\varepsilon_0^E}{\tilde{\varepsilon}},\quad \sin 2\alpha=-\frac{\varepsilon_2^E}{\tilde{\varepsilon}}, \tag{3}$$

where

$$\tilde{\varepsilon}=\sqrt{(\varepsilon_0^E)^2+(\varepsilon_2^E)^2}.$$

The value of the splitting of the ^5E ground state of the Mn^{3+} ion is given by

$$\Delta=|b|\tilde{\varepsilon},$$

where b is a coefficient relating the parameters of the noncubic field for the ^5E term with the deformations of the octahedron.

The splitting of the ^5E term due to the Jahn–Teller effect is accompanied by a specific degeneracy: the form of the ground state wave function is not fixed, since the value of α remains arbitrary. In fact, a given value of Δ and, hence, of $\tilde{\varepsilon}$, can be obtained for different ε_0^E and ε_2^E, which are connected by the single condition

$$(\varepsilon_0^E)^2+(\varepsilon_2^E)^2=\left(\frac{\Delta}{b}\right)^2=\text{const.}$$

This specific Jahn–Teller degeneracy will be lifted in the presence of at least a small external or initial deformation of the E type. In reality the Jahn–Teller effect reduces to a proportional enhancement of these deformations, $\varepsilon_v^E\rightarrow k\varepsilon_v^E$, with the ratio $\varepsilon_0^E/\varepsilon_2^E$ conserved.

This conclusion is of fundamental importance, since it enables one to find the ground state of a Jahn–Teller impurity ion of the Mn^{3+} type substituting for an ion with a known distortion of the nearest-neighbor environment. It should be noted that for a unique determination of the parameter α and, hence, Ψ_{base}, it is important to know the sign of the electron–lattice coupling parameter b. We will choose it to be negative, going on the reasonable assumption that the energy of the d_{z^2} electron is lowered relative to the energy of the $d_{x^2-y^2}$ electron when the M–6O octahedron is stretched along the z axis ($\varepsilon_2^E=0$, $\varepsilon_0^E>0$), i.e., that the ground state $|E2\rangle$ is thereby stabilized for ions with the configurations $3d^4$ and $3d^9$ (Refs. 8 and 9).

Thus for finding Ψ_{bas} of the Mn^{3+} ion in $RFeO_3$ it is sufficient to calculate the E-type deformation of the $Fe^{3+}-6O^{2-}$ complex from the known crystallographic data[1] and, from the value of the ratio

$$\tan 2\alpha=-\varepsilon_2^E/\varepsilon_0^E,$$

which is conserved when the Mn^{3+} ion is substituted for Fe^{3+}, to find α and Ψ_{base}. Table I gives the theoretically predicted values of the parameter α that determines the ground state of a Mn^{3+} impurity ion in $RFeO_3$. (The error in the determination of the angle is due to the uncertainties in the crystal parameters[1] and on average is not more than ±5°.)

Interestingly, for the Pr and Nd orthomanganites with known crystallographic parameters[2] the corresponding angles are equal to −25° ($PrMnO_3$) and −28° ($NdMnO_3$), i.e., rather close to the value of α for the analogous orthoferrites [−11° ($PrFeO_3$) and −16° ($NdFeO_3$)]. The differences can be explained by the effects of the cooperative Jahn–Teller distortion in orthomanganites. We note that the ratio of the values of $\tilde{\varepsilon}$ characterizing the degree of E-type distortion of the $Mn^{3+}-6O^{2-}$ octahedra in $PrMnO_3$ and $Fe^{3+}-6O^{2-}$ in $PrFeO_3$ is approximately equal to 15, which suggests the possibility of vibronic enhancement, by roughly an order of magnitude or more, of the deformations of the $Fe^{3+}-6O^{2-}$ octahedra in orthoferrites when Mn^{3+} is substituted for Fe^{3+}.

Figure 2 shows a qualitative picture of the orientation of

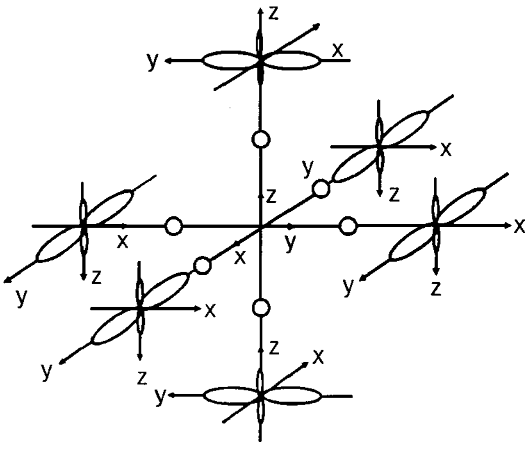

FIG. 2. Orientation of the e_g orbital of the d_{y^2} ion Mn^{3+} in six positions around a central Fe^{3+} ion.

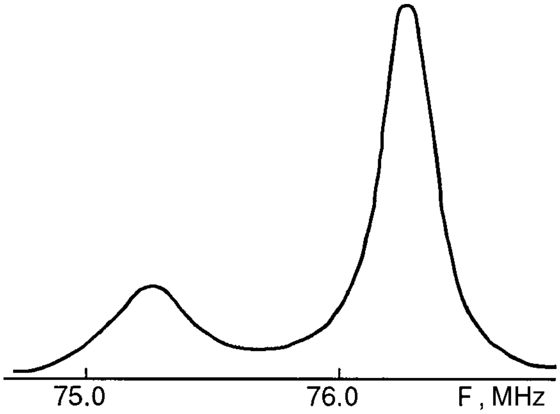

FIG. 3. Form of the NMR spectrum of ^{57}Fe in the orthoferrite $NdFe_{0.9}Al_{0.1}O_3$ at $T=112$ K.

the filled e_g orbitals of a $3d^4$ impurity ion. For simplicity we take the case $\alpha=-30°$, which is close to the real situation for $3d^4$ ions in Y, Ho, Er, and Tm orthoferrites. The wave function $\Psi_{\text{base}}=\sqrt{3}/2|E0\rangle-1/2|E2\rangle$ corresponds to the d_{y^2} orbital for an isolated e_g electron for the choice of local axes corresponding to Fig. 1. To simplify the picture the existing distortions of the perovskite structure in orthoferrites are not shown in Fig. 2.

We note that the method we have used to find the E-type ground state of Jahn–Teller ions in orthoferrites represents a further development of the concepts set forth mainly in Ref. 10.

For the purpose of studying the features of the manifestation of the Jahn–Teller effect of Mn^{3+} ions in $RFeO_3$, their ground state, and the confirmation of the conclusions of the theory, we have carried out an analysis of the satellite structure, which is mainly due to the transferred HF interaction, of the NMR spectrum of the ^{57}Fe nuclei in manganese-substituted Er and Tm orthoferrites.

In the unit cell of $RFeO_3$ there are four inequivalent positions of the Fe^{3+} ion. Each Fe^{3+} ion is coupled to six neighboring Fe^{3+} ions through the intermediate O^{2-} anions. Here one can distinguish three types of geometrically inequivalent $^{57}Fe–O^{2-}–Fe^{3+}$ bonds. When one of the neighboring Fe^{3+} ions is replaced by an ion with an orbitally nondegenerate ground state (a nonmagnetic ion such as Al^{3+} or Sc^{3+} or a magnetic ion such as Cr^{3+} or Mn^{2+}) this geometric inequivalence has practically no effect on the value of the HF field induced at the nucleus of the central Fe^{3+} ion. In that case the NMR spectrum of a system of the $RFe_{1-x}Al_xO_3$ type will contain, in addition to the main lines corresponding to the impurity-free ($6Fe^{3+}$) environment of the ^{57}Fe nucleus, isolated satellites corresponding to ^{57}Fe nuclei with one, two, etc. impurity ions in the nearest-neighbor environment. We have observed such a spectrum in the system $NdFe_{0.9}Al_{0.1}O_3$ (Fig. 3). When the Fe^{3+} ions are replaced by the magnetic ions Mn^{3+}, with an orbitally degenerate ground state, all three types of $^{57}Fe–O^{2-}–Fe^{3+}$ bonds will in general give different contributions to the HF field at the nucleus of the central Fe^{3+} ion. The NMR spectrum becomes more complicated: in addition to the main lines corresponding to an impurity-free nearest-neighbor environment of ^{57}Fe, one will observe, in the general case, three satellites corresponding to the three inequivalent $^{57}Fe–O^{2-}Mn^{3+}$ bonds of one Mn^{3+} impurity ion in the nearest-neighbor environment, etc.

The value of the HF field induced at the nucleus of the Fe^{3+} ion in the $^{57}Fe–O^{2-}–M$ chain, where M is a Jahn–Teller ion with orbital degeneracy of the ground state (Mn^{3+}, Co^{2+}, Fe^{2+}, . . .), will be essentially determined by the factors that lead to lifting of the orbital degeneracy of the M ion, on the one hand, and by the orbitally anisotropic contributions to the transferred HF interaction, on the other. Let us consider these effects in manganese-substituted orthoferrites, in which the Mn^{3+} ion can occupy six positions in the nearest-neighbor environment of a ^{57}Fe nucleus in $RFeO_3$, and, as we have said, only three of these are geometrically inequivalent (see Fig. 1).

The value of the HF field H_{THFI} induced at the ^{57}Fe nucleus for each of the $^{57}Fe–O^{2-}–Mn^{3+}$ chains can be related to the parameter α characterizing the ground state of any of the Mn^{3+} ions in the local coordinate system:

$$\begin{aligned}
H_{\text{THFI}}^{(1)}&=H_{e_g}^{(1)}\sin^2\alpha+H_{t_{2g}}^{(1)},\\
H_{\text{THFI}}^{(2)}&=H_{e_g}^{(2)}\sin^2(\alpha+60°)+H_{t_{2g}}^{(2)},\\
H_{\text{THFI}}^{(3)}&=H_{e_g}^{(3)}\sin^2(\alpha-60°)+H_{t_{2g}}^{(3)},
\end{aligned}\tag{4}$$

where H_{THFI} is the Hamiltonian of the transferred hyperfine interactions, H_{e_g} ($H_{t_{2g}}$) is the value corresponding to the HF field induced by a half-filled e_g (t_{2g}) shell. The superscript 1 refers to a $^{57}Fe–O^{2-}–Mn^{3+}$ chain lying along the c axis, and the superscripts 2 and 3 refer to chains in the ab plane (Figs. 1 and 2). Formulas (4) were obtained directly on the basis of the Hamiltonian H_{THFI} (see formula (24) of Ref. 11) with allowance for the fact that $\langle V_0^E(E)\rangle=-(1/2)\cos 2\alpha$ for chains along the c axis, and $\langle V_0^E(E)\rangle=-(1/2\cos 2(\alpha\pm60°)$ for chains in the ab plane.

In general the contributions to H_{THFI} from different chains cannot be assumed equal, for several reasons. First, the vibronic enhancement of deformations when the Jahn–Teller ion Mn^{3+} is substituted for Fe^{3+} is accompanied by a change in the $Mn^{3+}–O^{2-}$ distances in the chains, and this change is different for chains 1, 2, and 3. The relative change in the bond lengths in the case of vibronic enhancement is easily related to the parameter α characterizing the ground state of the Mn^{3+} ion:

$$\frac{\Delta R_{\text{Mn}-\text{O}}}{R_{\text{Mn}-\text{O}}}=\left(\frac{2}{3}\right)^{1/2}\tilde{\varepsilon}\cos 2\alpha \tag{5}$$

(for chains along the c axis),

$$\frac{\Delta R_{\text{Mn}-\text{O}}}{R_{\text{Mn}-\text{O}}}=\left(\frac{2}{3}\right)^{1/2}\tilde{\varepsilon}\cos 2(\alpha\pm60°)$$

(for chains in the ab plane),

where $\tilde{\varepsilon}$ is the average E-type deformation of the MnO_6 octahedron. Thus in the approximation linear in $\Delta R_{\text{Mn-O}}$ we have

$$\begin{aligned}
H_{e_g,t_{2g}}^{(i)}&=\tilde{H}_{e_g,t_{2g}}^{(i)}+\Delta H_{e_g,t_{2g}}\cos 2\alpha, \quad i=1,\\
H_{e_g,t_{2g}}^{(i)}&=\tilde{H}_{e_g,t_{2g}}^{(i)}+\Delta H_{e_g,t_{2g}}\cos(2\alpha+60°), \quad i=2,
\end{aligned}\tag{6}$$

$$H^{(i)}_{e_g,t_{2g}}=\widetilde{H}^{(i)}_{e_g,t_{2g}}+\Delta H_{e_g,t_{2g}}\cos(2\alpha-60^\circ),\qquad i=3,$$

and this complicates the analysis of the experiment considerably.

Second, a relation of the type $H^{(i)}_{e_g}=H_{e_g}$ does not take into account the important role that the empty e_g states of the Mn^{3+} ion play in a certain modification of the operator structure of H_{THFI} in the chains under consideration (concerning the features of the superexchange interaction involving the participation of empty e_g states, see, e.g., Refs. 12 and 13).

Ultimately, the expression for $H^{(1,2,3)}_{\mathrm{THFI}}$ can nevertheless be parametrized:

$$\begin{aligned}
H^{(1)}_{\mathrm{THFI}}&=H_{E_0}\cos^2\alpha+H_{E_2}\sin^2\alpha+\Delta H\sin^2\alpha\cos^2\alpha,\\
H^{(2)}_{\mathrm{THFI}}&=H_{E_0}\cos^2(\alpha+60^\circ)+H_{E_2}\sin^2(\alpha+60^\circ)\\
&\quad+\Delta H\sin^2(\alpha+60^\circ)\cos^2(\alpha+60^\circ),\qquad (7)\\
H^{(3)}_{\mathrm{THFI}}&=H_{E_0}\cos^2(\alpha-60^\circ)+H_{E_2}\sin^2(\alpha-60^\circ)\\
&\quad+\Delta H\sin^2(\alpha-60^\circ)\cos^2(\alpha-60^\circ),
\end{aligned}$$

where H_{E_0} and H_{E_2} are the values of H_{THFI} for $\alpha=0$ and $\alpha=\pi/2$, i.e., for the e_g electron in the $d_{x^2-y^2}$ and d_{z^2} states of the Mn^{3+} ion, respectively.

Thus the NMR spectrum of $^{57}\mathrm{Fe}$ in $\mathrm{RFe}_{1-x}\mathrm{Mn}_x\mathrm{O}_3$ contains, in addition to lines corresponding to an impurity-free environment of the iron nucleus, three satellite lines corresponding to an environment consisting of $5\mathrm{Fe}^{3+}+1\mathrm{Mn}^{3+}$ and shifted with respect to the main line in the direction of lower local fields by an amount

$$\Delta H^{(i)}=H_{\mathrm{THFI}}-H^{(i)}_{\mathrm{THFI}},\qquad (8)$$

where H_{THFI} is the contribution of the $^{57}\mathrm{Fe}\text{–}\mathrm{O}^{2-}\mathrm{Fe}^{3+}$ bond to the local field at the $^{57}\mathrm{Fe}$ nucleus. For $\alpha=-30^\circ$, which is close to the calculated value of this parameter for the Mn^{3+} ion in Y, Ho, Er, and Tm orthoferrites, we have

$$\begin{aligned}
\Delta H^{(1)}&=H_{\mathrm{THFI}}-\frac{3}{4}H_{E_0}-\frac{3}{16}\Delta H=\Delta H^{(2)},\\
\Delta H^{(3)}&=H_{\mathrm{THFI}}-H_{E_2}.
\end{aligned}\qquad (9)$$

An explanation of the experimental data can be obtained under the rather unusual condition

$$H_{E_2}\ll H_{\mathrm{THFI}}$$

which can be satisfied if, for example, allowance for the e_g states of the Mn^{3+} ion leads to a sharp change in the values of the constants α_1 in the Hamiltonian H_{THFI} of Ref. 11 from a value of $+1$ to values $\alpha_1<-1$. In this case the contribution of the d_{z^2} electron of the Mn^{3+} ion in a chain of type 1 should practically compensate the contribution of the t_{2g} shell. On the other hand, the experimental data indicate that the value of H_{E_0} (or ΔH) should be significant:

$$\left(H_{E_0}+\frac{1}{4}\Delta H\right)\approx H_{\mathrm{THFI}}$$

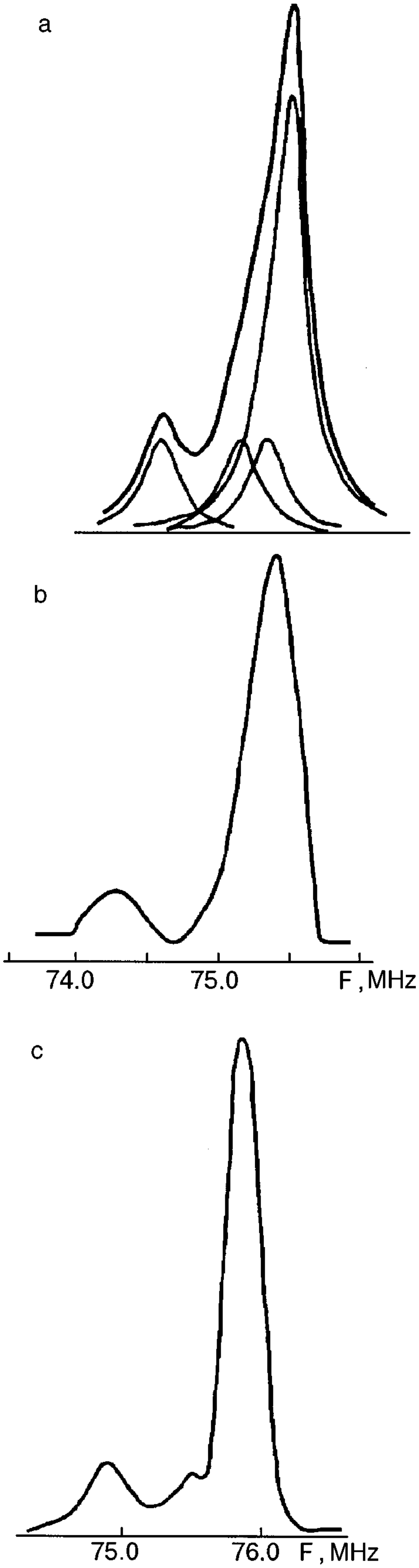

FIG. 4. NMR spectra of $^{57}\mathrm{Fe}$ in the manganese-substituted orthoferrite $\mathrm{ErFe}_{0.9}\mathrm{Mn}_{0.1}\mathrm{O}_3$ outside the spin-reorientation region, as predicted theoretically (a) and as measured experimentally at $T=94$ K (b) and 7 K (c).

Figure 4a shows the theoretical NMR spectrum of $^{57}\mathrm{Fe}$ in the orthoferrite $\mathrm{ErFe}_{1-x}\mathrm{Mn}_x\mathrm{O}_3$ for $x=0.1$. The value of Δ was chosen equal to 1.02 MHz and the half-width of the lines to 0.36 MHz (the line shape was assumed Lorentzian). Calculations were done in the approximation of a statistically uniform distribution of the manganese ions in the lattice. It is easy to see that if the lines are wide enough, only one of the three satellites, the one farthest from the central line, is resolved. The theoretical spectrum in Fig. 4a is in good agreement with the experimental NMR spectrum of ^{57}Fe in $ErFe_{0.9}Mn_{0.1}O_3$ at $T=94$ K [Fig. 4b]. The NMR spectrum of ^{57}Fe in manganese-substituted Tm orthoferrite has a similar form. When the temperature is lowered to 7 K, one more satellite is resolved [Fig. 4c].

SPIN-REORIENTATION TRANSITIONS AND THE ANISOTROPIC HYPERFINE INTERACTION

We note that in the analysis of the HF interaction in orthoferrites containing Mn ions we have temporarily neglected the anisotropy of the HF interaction, an effect that is particularly important in the interpretation of the NMR spectra in the region of the SR transitions. In other words, we have assumed that at sufficiently low concentrations of Mn^{3+} ions the presence of a Mn^{3+} ion in the nearest-neighbor environment of the Fe^{3+} ion does not alter its ''intrinsic'' anisotropic HF interactions resulting from the noncubic crystalline field of the lattice. This means that the value of the field for an impurity-free nearest-neighbor environment is assumed to be unaffected by the insertion of an impurity ion in the nearest-neighbor environment of ^{57}Fe and to remain equal to the corresponding value for pure $RFeO_3$. Certain arguments in support of this approximation are given by the conclusions in Ref. 7, according to which the largest contribution to the anisotropy of the ''intrinsic'' HF interactions in $RFeO_3$ comes from the noncubic field of the point lattice, and this field changes only slightly upon the substitution of Mn^{3+} for Fe^{3+}.

Let us consider the features of the anisotropic HF interactions in the substituted compounds. The anisotropic part of the HF field at the ^{57}Fe nucleus with a ''magnetic'' nearest-neighbor environment of the type $5Fe^{3+}$–$1Mn^{3+}$ in $RFe_{1-x}Mn_xO_3$ is represented in the form

$$\mathbf{h}=\mathbf{h}(0)-\mathbf{h}(\mathrm{Fe}_i)+\mathbf{h}(\mathrm{Mn}_i), \qquad (10)$$

where $\mathbf{h}(0)$ is the field for the impurity-free nearest-neighbor environment, and $\mathbf{h}(\mathrm{Re}_i)$ (or $\mathbf{h}(\mathrm{Mn}_i)$ is the field induced by the Fe^{3+} (or Mn^{3+}) ion found at the ith lattice site.

Assuming that at low enough concentrations of the Mn^{3+} ion the basic antiferromagnetic structure of the orthoferrites is preserved, and neglecting the noncollinearity of the spins, we write $\mathbf{h}$ in the form[7]

$$\mathbf{h}=\hat{a}\cdot\mathbf{G}, \qquad (11)$$

where $\mathbf{G}$ is the antiferromagnetism vector, and the components of the tensor $\hat{a}$ are determined by the parameters of different anisotropic interactions, and, in analogy with (10),

$$a_{lm}=a_{lm}(0)-a_{lm}(\mathrm{Fe}_i)+a_{lm}(\mathrm{Mn}_i). \qquad (12)$$

Thus we shall consider below only the contributions to $\mathbf{h}$ (or a_{lm}) resulting from the differences of the fields $\mathbf{h}(\mathrm{Fe}_i)$ and $\mathbf{h}(\mathrm{Mn}_i)$, which is due to the change in the magnetic-dipole interaction (^{57}Fe–Fe^{3+} and ^{57}Fe–Mn^{3+}) and the anisotropic transferred HF interaction (ATHFI) (^{57}Fe–O^{2-}–Fe^{3+} and ^{57}Fe–$O^{2-}Mn^{3+}$).

The change in the magnetic dipole contribution to a_{lm} can be straightforwardly calculated, and for the analysis of the ATHFI we use the technique proposed in Ref. 7, where it was shown that the following relation can be used to estimate the contribution of the ATHFI to the irreducible components of the tensor $\hat{a}(\mathrm{Fe}_i)$:

$$a_q^2(\mathrm{Fe}_i)=B(\mathrm{Fe})C_q^2(\theta_i,\varphi_i), \qquad (13)$$

with θ_i and φ_i being the polar and azimuthal angles of the vector of the O^{2-}–Fe_i bond in the system of crystallographic axes abc. The parameter B can in general be represented in the form of a sum, $B=B_\sigma+B_\pi$, where B_σ and B_π are the contributions from the σ and π bonds, respectively (actually, the contributions of the e_g and t_{2g} electrons of the Fe^{3+} ions).

Summing the contributions of the magnetic-dipole interaction and ATHFI, we find all of the components of interest to us $[a_{lm}(\mathrm{Mn}_i)-a_{lm}(\mathrm{Fe}_i)]$. It turns out that the shifts of the positions of the satellites relative to the predictions of the ''isotropic'' model are not large, and on the whole they hardly stand out above the standard error of the experiment (± 25 kHz). Interestingly, the small value of the shifts comes about as a result of a partial compensation of the contributions of the ATHFI and the magnetic-dipole interaction.

The most clear-cut effects of the anisotropic HF interaction are manifested in the NMR spectrum in the region of the SR transitions. As in the pure orthoferrites,[5–7] the substituted compounds also exhibit a shift and splitting of the NMR line, and not only of the main line but also of the satellites. The change in the position of the satellites relative to the main line at the transition from the Γ_2 to the Γ_4 configuration, i.e., the difference of the corresponding parameters of the anisotropic interactions, does not stand out above the limits of experimental error. The difference in the value of the splittings of the main line and satellites in the region of the SR transition $\Gamma_4\leftrightarrow\Gamma_2$ in the approximation used here is insignificant. Indeed, the magnetic-dipole interaction does not contribute to the quantity $2[a_{zx}(\mathrm{Mn})-a_{xz}(\mathrm{Fe})]$ that determines the difference in the splitting,[7] and our calculated value of the ATHFI contribution is only 0.03, 0.01, and 0.04 MHz for the satellites associated with the Mn^{3+} ion in positions 1, 2, and 3, respectively (Fig. 1).

Thus in the region of the SR transition $\Gamma_4\leftrightarrow\Gamma_2$ the values of the shift and splitting of the satellites and main NMR line of ^{57}Fe in manganese-substituted Er orthoferrite are practically the same within our adopted model. As an illustration, Fig. 5a shows the theoretical NMR spectrum of ^{57}Fe in $ErFe_{0.9}Mn_{0.1}O_3$ at the center of the temperature region of the SR transition $\Gamma_4\leftrightarrow\Gamma_2$; as a starting point, the initial positions of the lines and their half-widths were taken the same as for the spectrum in Fig. 4a. The splitting of the three satellites and the main line (these were all taken equal to 0.47 MHz, as in pure $ErFeO_3$) makes the picture of the NMR spectrum of ^{57}Fe considerably more complicated than that in the pure orthoferrites.[5–7] For comparison, Fig. 5b shows the experimental NMR spectrum of ^{57}Fe in $ErFe_{0.9}Mn_{0.1}O_3$ at $T=90.6$ K, which is approximately the temperature center of the SR transition. A comparison with the theoretical model spectrum shows good qualitative agreement.

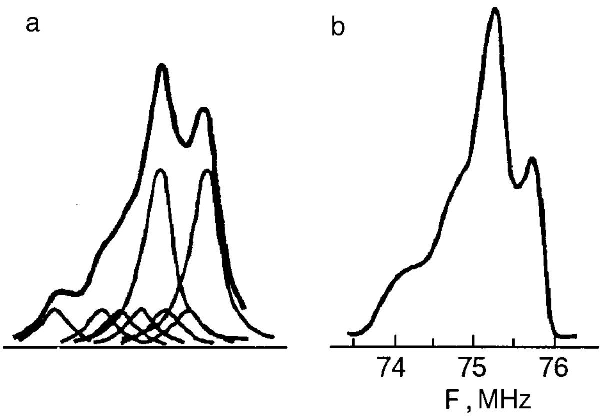

FIG. 5. NMR spectra of ^{57}Fe in $ErFe_{0.9}Mn_{0.1}O_3$ inside the temperature region of the SR transition, as predicted theoretically (a) and as measured experimentally at $T = 90.6$ K (b).

Thus the simple model we have adopted to describe the modification of the HF interactions in manganese-substituted orthoferrites correctly conveys all the characteristic features of the rather complicated NMR spectrum of ^{57}Fe in these compounds.

As in the pure orthoferrites, the NMR method can quite reliably establish the temperature interval of the reorientation in $RFe_{1-x}Mn_xO_3$; in particular, in $ErFe_{0.9}Mn_{0.1}O_3$ the SR transition $\Gamma_4 \leftrightarrow \Gamma_2$ occurs in the temperature interval 86.5–93 K.

CONCLUSION

We have used the spin-echo method to study the NMR spectrum of ^{57}Fe nuclei in manganese-substituted Er and Tm orthoferrites. The experimentally observed satellite structure of the spectra finds good agreement with the conclusions of a theoretical analysis, according to which the Jahn–Teller effect for the Mn^{3+} impurity ion is manifested in a physical enhancement of the *E*-type deformation of the $Fe^{3+}-6O^{2-}$ octahedron. This feature of the Jahn–Teller effect is also observed in a comparative analysis of the deformations of the complexes $Fe^{3+}-6O^{2-}$ in $RFeO_3$ and $Mn^{3+}-6O^{2-}$ in $RMnO_3$.

The ground state of the Mn^{3+} impurity ion in Tm and Er orthoferrites, as predicted theoretically and confirmed by experimental investigations of the satellite structure of the NMR spectrum, is described by a function Ψ_{base} for α close to 30° (see Table I). The same situation apparently exists for a number of other orthoferrites. This result is in good agreement with the published data on the influence of manganese ions on the magnetic properties of orthoferrites.[3] Indeed, for the ground state of the manganese ions corresponding to the value of the parameter α in Table I, the single-ion crystallographic magnetic anisotropy of the Mn^{3+} ions in all the orthoferrites is such that the *b* axis is the easy axis for the spins of the Mn^{3+} ions. This, in turn, agrees with the experimentally observed onset of SR transitions of the Morin type $G_x - G_y$ in manganese-substituted orthoferrites.[3]

The splitting of both the main and satellite lines of the ^{57}Fe NMR spectrum in manganese-substituted Er and Tm orthoferrites in the region of the SR transition is clear evidence that a magnetic inequivalence of both the sublattices of the Fe^{3+} ions and the sublattices of the Mn^{3+} impurity ions arises in this region.

We have presented a theoretical interpretation of the NMR spectra of ^{57}Fe in $RFe_{1-x}Mn_xO_3$ in the framework of the assumption that the Mn^{3+} ions are uniformly distributed over the four inequivalent positions in the orthoferrite lattice. The good agreement with the experimental data confirms the validity of this model.

*E-mail: karna@host.dipt.donetsk.ua

---

[1] M. Marezio, J. P. Remeika, and P. D. Dernier, Acta Crystallogr., Sect. B: **26**, 2008 (1970).

[2] *Magnetic Structures Determined by Neutron Diffraction*, Panst. Wyd. Naukowe, Warsaw (1976).

[3] K. P. Belov, A. K. Zvezdin, A. M. Kadomtseva, and R. Z. Levitin, *Orientational Transitions in Rare-Earth Magnets* [in Russian], Nauka, Moscow (1979).

[4] A. S. Moskvin and E. V. Sinitsyn, Fiz. Tverd. Tela (Leningrad) **17**, 2495 (1975) [Sov. Phys. Solid State **17**, 1664 (1975)].

[5] N. M. Kovtun, A. S. Karnachev, E. A. Solov'ev, A. Ya. Chervonenkis, and A. A. Shemyakov, Fiz. Tverd. Tela (Leningrad) **14**, 2150 (1972) [Sov. Phys. Solid State **14**, 1856 (1973)].

[6] V. D. Doroshev, A. S. Karnachev, N. M. Kovtun, E. E. Soloviev, A. Ya. Chervonenkis, and A. A. Shemyakov, Phys. Status Solidi B **51**, K31 (1972).

[7] A. S. Karnachev, Yu. I. Klechin, N. M. Kovtun, A. S. Moskvin, and E. E. Solov'ev, Zh. Éksp. Teor. Fiz. **78**, 1176 (1980) [Sov. Phys. JETP **51**, 592 (1980)].

[8] P. Novak, Czech. J. Phys., Sect. B **16**, 723 (1966).

[9] P. Novak, Int. J. Magn. **2**, 177 (1972).

[10] G. Matsumoto, J. Phys. Soc. Jpn. **29**, 606 (1970).

[11] A. S. Moskvin, N. S. Ovanesyan, and V. A. Trukhtanov, Hyperfine Interact. **3**, 429 (1977).

[12] J. B. Goodenough, *Magnetism and the Chemical Bond* [Interscience, New York (1963); Metallurgiya, Moscow (1969)].

[13] A. S. Moskvin, A. I. Likhtenshteĭn, and A. S. Luk'yanov, *Physics of Metals and Their Compounds* [in Russian], UrGU, Svedlovsk (1977).

Translated by Steve Torstveit

LOW TEMPERATURE PHYSICS VOLUME 26, NUMBER 4 APRIL 2000

Temperature-induced change in the ESR spectrum of the Fe^{3+} ion in polyaniline

V. N. Vasyukov, V. P. D'yakonov, and V. A. Shapovalov[a]

A. A. Galkin Donetsk Physics and Technology Institute, National Academy of Sciences of Ukraine, ul. R. Lyuksemburg 72, 83114 Donetsk, Ukraine

E. I. Aksimentyeva[b]

Lvov State University, ul Kirilla i Mefodiya 6, 79005 Lvov, Ukraine

H. Szymczak[c] and S. Piechota

Institute of Physics, Polish Academy of Sciences, Al. Lotnikov 32/46, 02-668 Warsaw, Poland

(Submitted August 3, 1999; revised December 3, 1999)
Fiz. Nizk. Temp. **26**, 363–369 (April 2000)

Research on polyaniline doped with $K_3[Fe(CN)_6]$ has revealed an effect which is manifested in an unusual temperature-induced change in the ESR spectrum of the Fe^{3+} ion. At low temperature ($T = 4.2$ K) one observes the first resonance line ($g_1 = 4.22 \pm 0.03$), and at high temperature ($T = 295$ K) the second line ($g_2 = 2.13 \pm 0.05$). The transition from the low-to the high-temperature spectrum occurs gradually and is accompanied by a redistribution of the absorption intensity. The observed properties of the temperature dependence of the ESR spectrum are typical of systems with a multiple-minimum potential. © *2000 American Institute of Physics.* [S1063-777X(00)00604-6]

1. INTRODUCTION

In Ref. 1 an unusual temperature dependence of the ESR spectrum of the Fe^{3+} ion was observed in the metalorganic substance nitroso-β-naphthol, the ESR spectrum of which is a superposition of low-temperature and high-temperature spectra. A change in temperature leads to a redistribution of the absorption intensities between the low-temperature and high-temperature spectra. This behavior of the ESR spectrum is evidence of unusual dynamics of the molecules surrounding the Fe^{3+} ion. The presence of this dynamics can have a substantial influence on the various properties of the substance.

In addition, research on these dynamic transitions is of independent interest, since the systems exhibiting these properties are, as a rule, systems with multiple-minimum potentials. These have not been adequately investigated experimentally. Systems with multiple-minimum potentials can be of various physical natures, but their common property is the presence of several potential wells separated by potential barriers. The best-studied is the Jahn–Teller system of a divalent copper ion in an octahedral environment.[2] In that study three energetically equivalent potential wells are determined by the Jahn–Teller interaction of the twofold degenerate orbital state with the tetragonal deformations of the octahedral environment.

An example of a physically different kind of system with a multiple-minimum potential is crystalline methane.[3] The energy of the couplings inside the molecule is much higher than the energy of the couplings between these molecules. Therefore, in their thermal motion the CH_4 molecules can be treated as separate anisotropic particles. At low temperatures the orientation of the molecules is fixed and corresponds to the minima of the interaction energy of these molecules in the crystal. The directions of the four equivalent threefold axes of the methane molecule dictate the orientations corresponding to the four minima of the interaction energy. Increasing the temperature leads to oscillations of the orientation of the molecules about the minima of the potential well. The amplitudes of these oscillations increase as the temperature is raised. This increases the probability that a threefold axis of the methane molecule will rotate from one minimum position to another. As a result, the orientation of the molecules is averaged out, and the anisotropy of the properties of the methane molecules is decreased.[3]

A system with a multiple-minimum potential of an unknown nature was observed in Ref. 1. It did not manifest a Jahn–Teller effect for the Fe^{3+} ion, and the cause of its unusual dynamics was tentatively attributed to features of the molecules surrounding the magnetic ion. Nitroso-β-naphthol contains aromatic hydrocarbon elements. The temperature dependence of the ESR spectrum may be due to either the motion of the aromatic elements relative to their equilibrium position or to the properties of the benzene rings themselves. In this paper we attempt to clarify this question by investigating the temperature dependence of the ESR spectrum of the $[Fe(CN)_6]^{3-}$ complex in polyaniline, the composition of which is substantially different from that of nitroso-β-naphthol. The base of the polyaniline structure is emeraldine (Fig. 1), which, like nitroso-β-naphthol, contains benzene rings.

To answer the question posed above we used the method of ESR spectroscopy.

2. EXPERIMENTAL RESULTS

We investigated the ESR spectrum on samples of undoped and doped polyaniline (PAN). The first sample, a PAN powder in the emeraldine base form, was obtained at $T = 293$ K by oxidative polymerization of aniline in

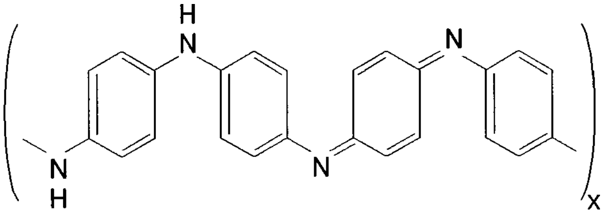

FIG. 1. Structural formula of emeraldine.

the presence of an equimolar quantity of ammonium peroxodisulfate in a 0.5 M aqueous solution of sulfuric acid, then neutralized with a 5% solution of ammonia, repeatedly washed with water and acetone until a colorless filtrate was obtained, and then dried in a dynamic vacuum at a temperature of 100–120 °C.

The second sample of PAN was obtained by the ion-exchange doping of an emeraldine base by holding the synthesized PAN powder in a 0.02 M solution of potassium hexacyanoferrate (III) in 0.05 M sulfuric acid for 24 hours. This sample was washed and dried in the same way as the first. Both samples were sealed in quartz ampoules. The first sample was a pure PAN powder, while the second contained 0.3% $K_3[Fe(CN)_6]$.

The ESR spectrum described in this article for PAN doped with potassium hexacyanoferrate (III) is a superposition of the ESR spectra of the free radicals of PAN and Fe(III) ions.

The spectrum was studied on an ESR spectrometer with a frequency of the microwave field $\nu = 9.241 \pm 0.001$ GHz in the temperature interval $T = 4.2$–295 K. The ESR spectrum of pure PAN in the temperature interval $T = 4.2$–295 K consists of one resonance line with a g factor $g_3 = 2.000 \pm 0.001$. This line has the feature than its width ΔH_{pp} decreases with increasing temperature (Fig. 2). The value of the g factor is independent of temperature. The resonance line of pure PAN is due to the existence of free radicals.

The ESR spectrum of the sample doped with $K_3[Fe(CN)_6]$ consists of three resonance lines. The overall appearance of the spectrum at an intermediate temperature $T = 109$ K is shown in Fig. 3. The first and second resonance lines result from the doping of the sample and can be explained by the presence of the Fe^{3+} ion. The third resonance line, as judged from the value of the g factor and the character of its behavior when the temperature is changed, belongs to free radicals in the PAN.

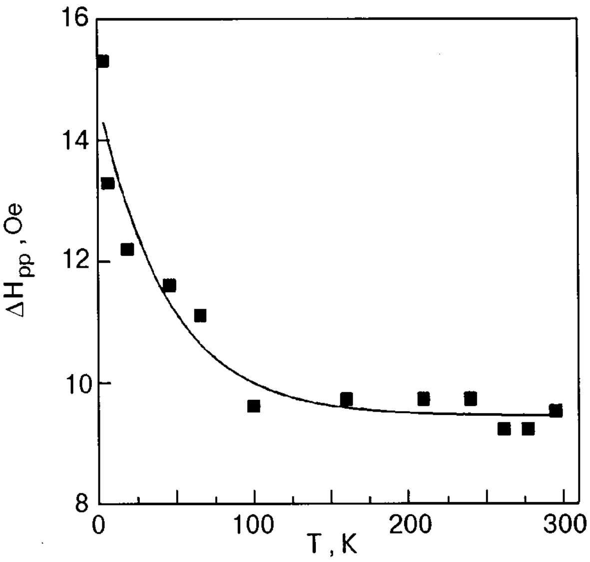

FIG. 2. Temperature dependence of the resonance linewidth ΔH_{pp} of pure polyaniline.

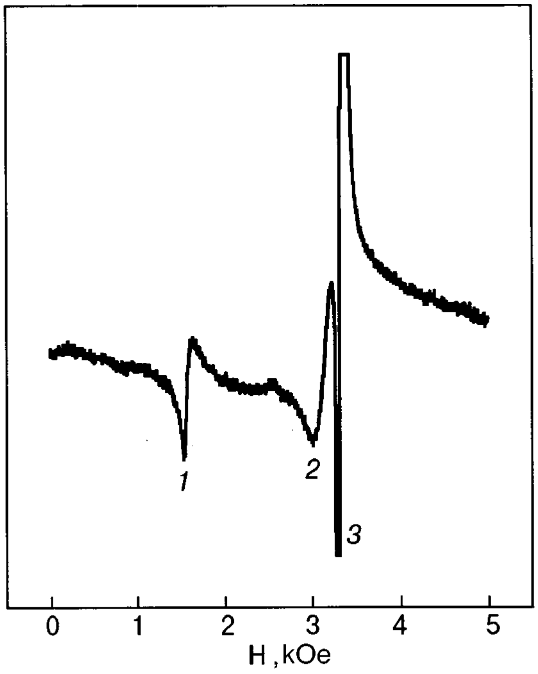

FIG. 3. Form of the ESR spectrum of the Fe^{3+} ion in polyaniline at $T = 109$ K.

The value of the g factor of line *1* at $T = 4.2$ K is $g_1 = 4.22 \pm 0.03$ and is practically independent of temperature. The g factor of line *2* at $T = 295$ K has the value $g_2 = 2.13 \pm 0.05$.

When the temperature is changed, one observes an unusual change in the resonance lines *1* and *2* of the ESR spectrum (see Fig. 4). When the temperature is increased, the intensity of the resonance line *1* decreases until it vanishes completely at $T = 295$ K. Here the linewidth ΔH_1 increases by no more than 30% (Fig. 5).

The increase in the intensity of line *1* when the temperature is lowered is due to two mechanisms. The first of these involves the ''usual'' change in the population of the energy levels between which the ESR transition occurs, and for a frequency $\nu = 9.24$ GHz of the microwave field the temperature dependence of the intensity is governed by the ratio $J(T)/J_0 = h\nu/kT$. This mechanism is more or less typical for all the resonance lines, but it is manifested most clearly for line *3* of pure PAN.

Figure 6 shows the temperature dependence of the ratio of the peak-to-peak intensities $J1_{pp}/J3_{pp}$ of lines *1* and *3*, which attests to the presence of an additional mechanism of temperature dependence of the intensity of line *1*, and that is the mechanism discussed in this paper. This atypical temperature dependence for the ESR spectrum of the Fe^{3+} ion indicates that the change in the intensity is not due to ordinary relaxation broadening of the resonance lines.

At $T = 295$ K the width of line *2* has the value ΔH_{pp}

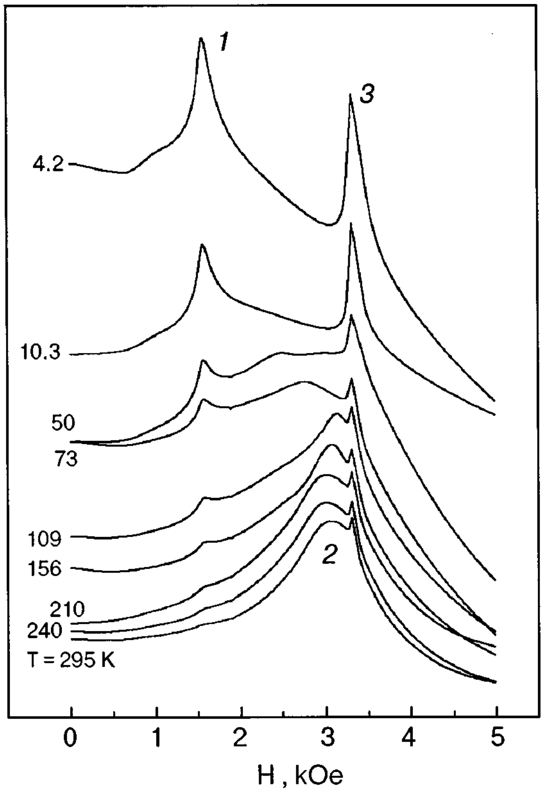

FIG. 4. Temperature-induced changes in the original absorption of the ESR spectrum of the Fe^{3+} ion in polyaniline.

$=0.75$ kOe. Its width increases as the temperature is lowered, and the resonance line is not detected at $T<50$ K. The broadening of line *2* is accompanied by a decrease of the peak intensity until it vanishes completely. It should be noted that the usual mechanism for broadening of the resonance line of the ESR spectrum, that due to spin–lattice relaxation processes, leads to an increase of the linewidth with increasing temperature. The experimental observation of the opposite temperature dependence of the linewidth is evidence for the presence of an additional, more effective mechanism that governs the width of the ESR line.

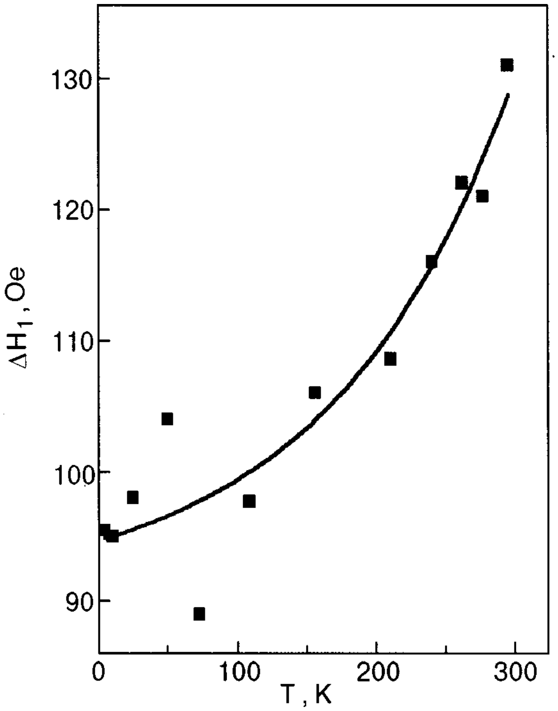

FIG. 5. Temperature dependence of the width ΔH_1 of the first resonance line.

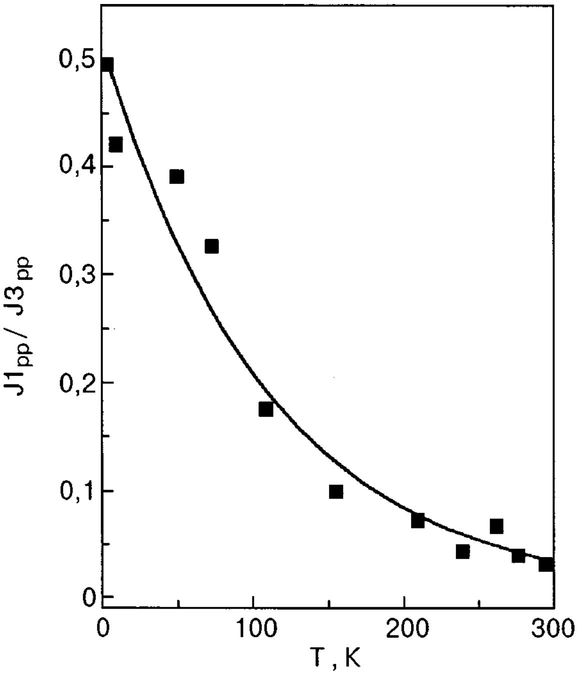

FIG. 6. Temperature dependence of the peak–peak intensity ratio $J1_{pp}/J3_{pp}$ of lines *1* and *3*.

The unusual behavior of the intensity of resonance line *1* and of the width of resonance line *2* of the ESR spectrum suggests that lines *1* and *2* are interrelated.

Since line *2* has an appreciable width that increases as the temperature is lowered, for illustration of the behavior of the ESR spectrum it is more convenient to represent it in the form of the absorption curve rather than its derivative, which is usually recorded when a synchronous detector is used. Figure 4 shows the form of the such an ESR spectrum for nine values of the temperature.

According to Fig. 4, the g factors of resonance lines *1* and *3* are independent of temperature. The position of line *2* in the interval interval 100–295 K corresponds to a g factor $g_2\approx 2.13$. As the temperature is lowered further, a gradual shift of line *2* to lower fields occurs along with a broadening of its width.

Resonance line *1* is the low-temperature ESR spectrum of the Fe^{3+} ions, and line *2* is the high-temperature spectrum. A change in temperature leads to a redistribution of the absorption intensity between the low-temperature and high-temperature spectra.

3. DISCUSSION OF THE RESULTS

The above-described ESR spectrum of the Fe^{3+} ion in PAN has a number of features that must be examined separately.

1. Let us start with a discussion of the values obtained for the g factors of resonance lines *1* and *2*, which belong to the iron impurity ion. The Fe^{3+} ion has the configuration d^5.

The spin of the ground state is $S=5/2$. For the most frequently encountered ESR spectra of the Fe^{3+} ion the g factor typically has a value close to 2.

On the other hand, the resonance line with $g\approx 4.3$ has been investigated in a number of studies[4–6] of the ESR spectrum of the iron ion in silicate glasses, which, like our PAN sample, lack long-range order. A spectrum with $g\approx 4.3$ is also observed in several polycrystalline biological systems.[7–9] A detailed analysis of the results on the ESR spectrum of iron ions in amorphous substances is given in Ref. 10. It was shown in that paper that the spectrum, which consists of two resonance lines with $g\approx 2$ and $g\approx 4.3$, belongs to different inequivalent magnetic centers of the Fe^{3+} ion, which differ in the amount of the low-symmetry component of the crystalline field acting on the magnetic ion. The line with $g\approx 2$ corresponds to a center at which the low-symmetry component of the crystalline field is much less than the Zeeman energy, while the line with $g\approx 4.3$ corresponds to a center for which the low-symmetry component of the crystalline field is much larger than the Zeeman energy.

In this paper we understand the term ''crystalline field'' to mean the local electric field created at an Fe^{3+} magnetic impurity ion by the surrounding molecules.

2. The intensity of the ESR line is proportional to the number of magnetic ions participating in a given transition. The redistribution of the intensities of lines *1* and *2* attests to a change in the number of magnetic ions corresponding to these centers.

The authors think it improbable that the temperature-induced changes lead to a real displacement of the Fe^{3+} ions from one of the inequivalent positions to another. In that case, according to the results of Ref. 10 and the temperature dependence of the ESR spectrum from the present study, the low-symmetry component of the crystalline field acting on an Fe^{3+} ion in PAN would be much less than the Zeeman energy at low temperatures and much greater than the Zeeman energy at high temperatures.

3. If the electric field of the nearest-neighbor environment of the magnetic ion Fe^{3+} has cubic symmetry or a low-symmetry component that is much less than the Zeeman energy, then the Hamiltonian of the zeroth approximation will be of the form

$$H_0=g_0\beta\mathbf{H}\cdot\mathbf{S}, \tag{1}$$

where β is the Bohr magneton and g_0 is the g factor of the ground state multiplet $S=5/2$. The numerical value of g_0 is close to 2.0. The Hamiltonian of the fine-structure splitting should be treated as a perturbation. The ESR spectrum of the magnetic center in this case consists of five lines. The central resonance line, as a rule, is independent of the direction of the magnetic field and corresponds to a transition $+1/2\leftrightarrow -1/2$. The other four resonance lines of the fine structure of the spectrum depend on the magnetic field direction. In a ''polycrystalline'' sample one will observe a single resonance line with an effective g factor equal to the g factor of the resonance transition $+1/2\leftrightarrow -1/2$ and having a value $g\approx 2$. The resonance lines of the other transitions of the fine structure of Fe^{3+} are averaged as a result of the orientational disordering and will contribute to the linewidth.

According the usual relaxation properties of the transition $+1/2\leftrightarrow -1/2$ for the S ion Fe^{3+}, one would expect that the spectral line with $g\approx 2$ should be observed experimentally throughout the entire temperature interval from helium to room temperatures. Raising the temperature should lead to the usual relaxation broadening of the line. However, the experiments done in the present study demonstrate the opposite temperature dependence of the width of the resonance line with $g\approx 2$: the width of this line decreases as the temperature is raised. This unusual behavior requires additional explanation.

4. If the low-symmetry component of the electric field of the nearest-neighbor environment of the magnetic ion Fe^{3+} is much greater than the Zeeman energy, then, according to Ref. 10, the Hamiltonian of the zeroth approximation should be expressed in the form

$$H_0=D(S_z^2-S(S+1)/3)+D(S_x^2-S_y^2)/3. \tag{2}$$

The Zeeman Hamiltonian (1) and the Hamiltonian of the fine-structure splitting

$$H_1=(E-D/3)(S_x^2-S_y^2) \tag{3}$$

should be treated as a perturbation. Here S_x, S_y, and S_z are components of the spin operator, and D and E are parameters of the initial splitting, which characterize the field of axial symmetry and the rhombic component of the field, respectively. The action of Hamiltonian (2) splits the spin multiplet $S=5/2$ into three Kramers doublets with energies $\varepsilon_1=0$, $\varepsilon_2=4\sqrt{7}D/3$, and $\varepsilon_3=-4\sqrt{7}D/3$. According to the estimate of Ref. 10, the lower and upper doublets have highly anisotropic g factors, while the g factor of the middle doublet is isotropic and approximately equal to 4.3. The axis of symmetry of the different magnetic centers in ''polycrystalline'' sample are oriented randomly in different directions with respect to the magnetic field. As a result, the ESR spectrum of the doublets with anisotropic g factors are ''smeared'' over a wide range of magnetic fields and are therefore not observed in experiments. Only resonance line *1* (Fig. 4), with $g_1=4.22$, is observed experimentally. The difference between the estimate $g_1=4.3$ in Ref. 10 and the experimental value 4.22 ± 0.03 for the S ion is within acceptable error and is apparently due to the fact that we have not taken into account all the mechanisms that contribute to the g factor.

On account of the characteristic relaxation properties of the S ion Fe^{3+}, line *1* with $g_1\approx 4.22$ should be observed over the entire range of temperatures investigated.

The results of the present study do not confirm such a character of the temperature dependence. According to the experimental data, at liquid-helium temperature one observes an intense line of width $\Delta H_{pp}=96$ Oe with an effective g factor $g_1=4.22\pm 0.03$. As the temperature is raised the intensity of the line decreases to where it vanishes completely (Fig. 4). Since the broadening of the line is insignificant, the fall of the peak intensity is not due to the usual relaxation processes.

5. The transition from the low-temperature spectrum to the high-temperature spectrum occurs gradually rather than in a jump (Fig. 4). Therefore, structural phase transitions cannot be the cause of the temperature-induced change of the intensity of the lines of the ESR spectrum.

Let us list the observed properties: 1) the existence of a low-temperature, low-symmetry state and a high-temperature, high-symmetry state; 2) the presence of a temperature region in which these states coexist; 3) a decrease of the intensity of the low-temperature spectrum and an increase in the intensity of the high-temperature spectrum as the temperature is raised. These properties are typical of systems with multiple-minimum potentials. The best-studied of these is the Jahn–Teller system of a divalent copper ion in an octahedral crystalline environment. The temperature-induced changes of the intensities of the spectra corresponding to the low-symmetry and high-symmetry states for such systems are due to a change in the population of vibronic states.[2] The fact that the temperature-induced changes of the ESR spectrum of the Fe^{3+} ion in PAN are the same as the analogous temperature-induced changes of other well-studied systems with multiple-minimum potentials[2,11,12] suggests that the sample under study can be regarded as a system with a multiple-minimum potential.

It should be noted here that Fe^{3+} is an *S* ion, and the appearance of the Jahn–Teller effect for this ion is improbable. In the case under study the Fe^{3+} ion plays the role of a paramagnetic probe which permits one to observe the unusual dynamics of the molecular environment.

4. CONCLUSION

In the framework of the proposed model we have been able to explain the unusual temperature dependence of the intensity of the resonance line *1* of the ESR spectrum, the width of the resonance line *2*, and other features of the ESR spectrum.

At helium temperature the molecules of the environment are ‘‘frozen’’ in positions corresponding to the largest value of the low-symmetry component of the crystalline field at the bottom of the potential wells. Then the anisotropy of the electric field is maximum, and therefore only the first resonance line is observed. As the temperature is raised, some of the magnetic centers undergo a transition to excited vibronic states. The excited states of systems with multiple-minimum potentials, as a rule, are less anisotropic than the ground state (the deformations are averaged as a result of fast ‘‘hops’’ from one potential well to another). The suprabarrier states (the states whose energies are greater than the height of the barrier separating the potential wells[2]) are the least anisotropic. The occupation of the suprabarrier states gives rise to resonance line *2* of the ESR spectrum (Fig. 4). Increasing the number of magnetic centers found in excited states will lead to a decrease in the number of magnetic centers in the ground state. This circumstance is the cause of the decrease of the intensity of resonance line *2* as the temperature is raised.

The unusual temperature dependence of the width of the resonance line *2* (Fig. 4) is due to the distribution of magnetic centers over excited states. As a rule, for systems with multiple-minimum potentials, the higher the energy of the excited state, the lower the distortion corresponding to this vibronic state. If the energy of excitation is greater than the height of the barrier between potential wells (suprabarrier states), then the distortion becomes minimal or equal to zero.

At high temperatures more of the magnetic centers are found in suprabarrier states. The ESR spectrum of these centers is determined by the *g* factor of the transition $+1/2 \leftrightarrow -1/2$.

At low temperatures an appreciable fraction of the magnetic centers will be found in subbarrier excited states. The lower the excitation energy, the larger the low-symmetry component of the electric field and the farther the resonance lines of the transitions $\pm 5/2 \leftrightarrow \pm 3/2$ will be from the line of the transition $+1/2 \leftrightarrow -1/2$. As a result of the orientational averaging over the directions of the symmetry axes, the contribution of the transitions $\pm 5/2 \leftrightarrow \pm 3/2$ and $\pm 3/2 \leftrightarrow \pm 1/2$ at low temperatures will lead to broadening of resonance line *2*.

The temperature-induced change in the ESR spectrum of the complex $[Fe(CN)_6]^{3-}$ in polyaniline is practically the same as the temperature-induced change of the ESR spectrum of the Fe^{3+} ion in nitroso-β-naphthol.[1] This coincidence of the properties of the ESR spectra of these two magnetic centers despite the substantially different molecular environments of the Fe^3 ion attests to the presence of an effect which is common to these substances.

[a]E-mail: shapoval@host.dipt.donetsk.ua
[b]E-mail: aksiment@org.lviv.net
[c]E-mail: szymh@gammal.ifpan.edu.pl

---

[1] V. P. D’yakonov, V. N. Vasyukov, V. A. Shapovalov, E. I. Aksimentyeva, G. Shimchak, and S. Pekhota, Fiz. Tekh. Vys. Davlenii **8**, 60 (1998).
[2] V. N. Vasyukov and B. Ya. Sukharevskiĭ, Fiz. Nizk. Temp. 20, 821 (1994) [Low Temp. Phys. **20**, 644 (1994)].
[3] A. V. Leont’eva, G. A. Marinin, and A. Yu. Prokhorov, Zh. Fiz. Khim. **68**, 975 (1994).
[4] T. Castner, G. S. Newell, W. C. Holton, and C. P. Slechter, J. Chem. Phys. **32**, 668 (1960).
[5] E. Burzo, M. Chipara, D. Ungur, and I. Ardelean, Phys. Status Solidi B **124**, K117 (1984).
[6] R. Singh, J. Phys. D **17**, L57 (1984).
[7] H. H. Wickman, M. P. Klein, and D. A. Shirley, J. Chem. Phys. **42**, 2113 (1965).
[8] R. D. Dowsing and J. F. Gibson, J. Chem. Phys. **50**, 294 (1969).
[9] R. Aasa, J. Chem. Phys. **52**, 3919 (1970).
[10] Ya. G. Klyava, *EPR Spectroscopy of Disordered Solids* [in Russian], Zinatne, Riga (1988).
[11] K. Tomita, Phys. Rev. **89**, 429 (1953).
[12] P. G. Krusic, D. C. Roe, and E. Johnston, J. Phys. Chem. **97**, 1736 (1993).

Translated by Steve Torstveit

ESR spectrum of $KTm(MoO_4)_2$

M. I. Kobets,* V. A. Pashchenko, and E. N. Khats'ko

B. I. Verkin Physicotechnical Instute for Low Temperature Physics, National Academy of Sciences of Ukraine, Lenin prospect, 47, 61164 Kharkov, Ukraine

(Submitted August 19, 1999; revised November 12, 1999)
Fiz. Nizk. Temp. **26**, 370–373 (April 2000)

The angular and frequency dependences of the ESR spectrum of single-crystal $KTm(MoO_4)_2$ are investigated at helium temperature. It is shown that this compound belongs to the class of highly anisotropic paramagnets. The g factors of the ground state ($g_x = 0.3 \pm 0.2$; $g_y = 0.3 \pm 0.2$; $g_z = 13.9 \pm 0.1$) and the angle of rotation of the local axes in the ac plane ($\theta = \pm(7.6 \pm 1)°$) are determined for two Tm^{3+} paramagnetic centers. © *2000 American Institute of Physics.* [S1063-777X(00)00704-0]

INTRODUCTION

Potassium–thulium molybdate $KTm(MoO_4)_2$ is a typical member of the $KR(MoO_4)_2$ family (where R=Dy, Ho, Er, Tm, Yb, Lu, Y).[1] Many members of this series are Jahn–Teller systems. These compounds belong to the orthorhombic symmetry class, with space group $D_{2h}^{14}(Pbcn)$. They have four formula units per unit cell. The lattice constants of $KTm(MoO_4)_2$ are as follows: $a = 5.05$ Å, $b = 18.28$ Å, $c = 7.89$ Å.[2,3] In the present study we have investigated the resonance behavior of the Tm^{3+} ions in the $KTm(MoO_4)_2$ lattice by the ESR method for the purpose of obtaining important information about the ground state of the paramagnet, the values of the g factors, and the interactions that form the energy spectrum.

EXPERIMENTAL RESULTS

The high-frequency properties of single-crystal KTm $(MoO_4)_2$ were investigated at helium temperature in the frequency range 36–190 GHz. The measurements were made on a complex of radio spectrometers with a resonator cell. The sample was mounted in the cylindrical resonator on a dielectric device which permitted rotating the sample; it was placed near an antinode of the rf magnetic field, where both parallel and perpendicular polarizations of the microwave field relative to the external static magnetic field were present. The magnetic field source in the experiment was a superconducting solenoid with a maximum field of 8 T. We studied the angular dependence of the ESR spectrum of the Tm^{3+} ions in the crystallographic planes ac and bc of the crystal and the frequency–field dependence of the ESR absorption line for an orientation of the external magnetic field along the c axis.

Figures 1 and 2 show the angular dependence of the ESR spectrum of $KTm(MoO_4)_2$ for different directions of the external magnetic field in the ac and bc planes, respectively. The measurements were made at a frequency of 104.3 GHz at helium temperature. For the orientation with the magnetic field in the ac plane (Fig. 1) we observed the absorption lines of two geometrically inequivalent centers. The local axes z and x of these centers are symmetrically rotated in the ac plane in both directions relative to the crystallographic axes c and a. The angle of rotation is $(7.6 \pm 1)°$. The presence of two centers is typical for the majority of the members of this family.[4,5] In the bc plane one sees a single structure of the ESR absorption line at any angles. The half-width of the resonance absorption line is found to depend strongly on the direction of the external magnetic field relative to the local magnetic axes. The minimum half width at half maximum (HWHM) of the ESR line of the Tm^{3+} ions, $\Delta H = 150$ Oe, corresponds to a direction of the applied field along the local z axis, and as the direction deviates from this axis toward either of the crystallographic axes a or b the absorption line gradually broadens to 4000 Oe. The narrow absorption line ($\Delta H = 450$ Oe) is unusual for the magnetically concentrated paramagnets of this family. The significant broadening of the resonance absorption line, especially in the neighborhood of the local axes x and y of the Tm^{3+} magnetic centers, and the small values of the splitting of the g factors g_x and g_y do not allow an accurate determination of the extremal positions of the resonance absorption line along these axes. Since the capabilities of our experimental apparatus do not allow us to reach the magnetic field values at which the absorption line is observed, we could only estimate an upper bound on the spectroscopic splitting factor.

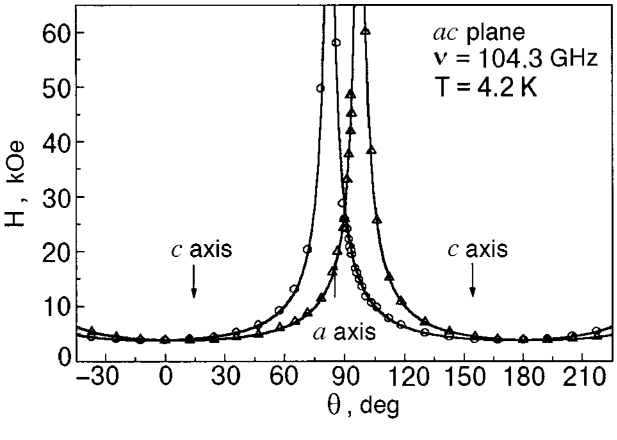

FIG. 1. Angular dependence of the position of the ESR line of single-crystal $KTm(MoO_4)_2$ for an orientation with the external magnetic field H in the ac plane. The continuous curves are the theoretical calculation; the points are experimental data.

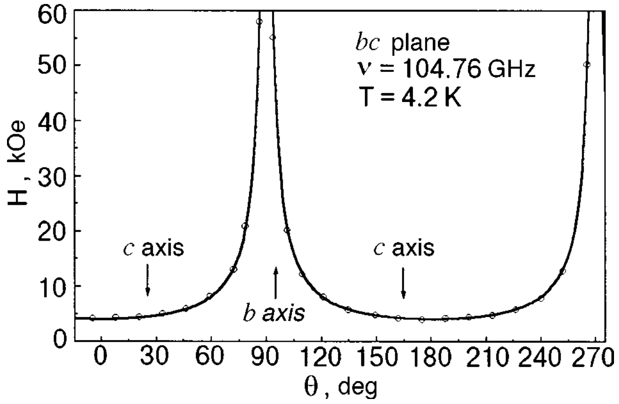

FIG. 2. Angular dependence of the position of the ESR lines of single-crystal $KTm(MoO_4)_2$ for an orientation with the external magnetic field H in the bc plane. The continuous curves are the theoretical calculation; the points are experimental data.

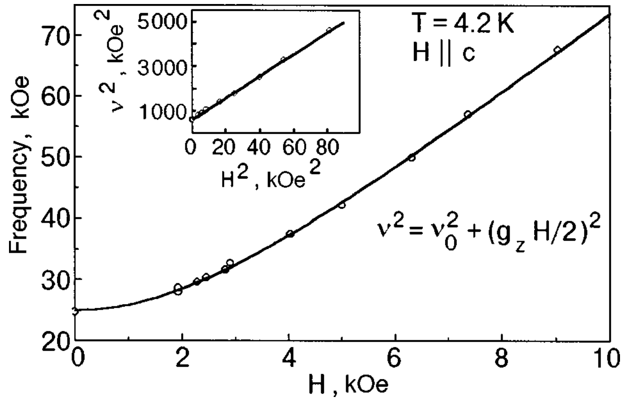

FIG. 3. Frequency–field curve of the ESR spectrum of $KTm(MoO_4)_2$ for $H\|z$.

For these directions the g factor does not exceed 0.4.

We note that the width and intensity of the ESR line of the Tm^{3+} ion in the crystal $KTm(MoO_4)_2$ depend strongly on the mechanical stresses and pressure.

Figure 3 shows the frequency–field dependence of the ESR spectrum of $KTm(MoO_4)_2$ for the orientation with the external magnetic field $\mathbf{H}$ along the local z axis of the crystal ($T=4.2$ K). The frequency–field curve of the ESR absorption line has a nonlinear character and conforms well to a quadratic law with a gap of (69.9±0.5) GHz at zero magnetic field. This quadratic dependence is shown in the inset to Fig. 3. From the slope of the straight line we determined the value of the effective g factor for this axis of the crystal: $g_z=13.9\pm0.1$. At frequencies less than the value of the gap the ESR spectrum is not observed in single-crystal KTm $(MoO_4)_2$.

DISCUSSION OF THE RESULTS

Angular dependence of the ESR

It is known that, depending on the type of rare-earth ion and the symmetry of the crystalline environment, the multiplets of the ion should be split by the crystalline field into energy levels with different degrees of degeneracy — singlets, doublets, and triplets. In real crystals these levels can be close in energy. As a result, quasidegenerate levels — accidental doublets, triplets, etc. — appear in the spectrum of the ion. In low-temperature studies one ordinarily examines only the lowest energy levels, since only they are populated at these temperatures. If the ground-state quasidoublet of the rare-earth ion is separated from the excited levels by a large interval ΔE, then at temperatures $T<\Delta E$ the interaction of the rare-earth ion with the external magnetic field can be described by a Hamiltonian of the form $H=E_0+\Delta S_x+m_B(\mathbf{g}\cdot\mathbf{H})S_z$, where $E_0=(1/2)(E_{01}+E_{02})$ is the energy corresponding to the centroid of the quasidoublet, $\Delta=E_{02}-E_{01}$ is the initial ‘‘splitting’’ of the quasidoublet in the crystalline field, $\mathbf{g}$ is the vector determining the magnitude and direction of the (only) nonzero g factor, and S_x and S_z are the standard matrices of the spin-1/2 operators.[6]

A magnetic field applied in any direction perpendicular to the z axis will not cause additional splitting of the quasidoublet; the g tensor of the quasidoublet is axially symmetric and has only one nonzero component g (along the z axis) regardless of the symmetry of the crystalline environment of the ion, if one does not take into account the terms quadratic in the magnetic field.[7]

Experimental investigations of the angular dependence of the ESR spectrum of the Tm^{3+} ion in the $KTm(MoO_4)_2$ lattice indicate that this rare-earth ion can be regarded as a typical non-Kramers ion (ground state $4f^{12}$, $^3H_6$) with an initial splitting of the ground state. The strong anisotropy of the g tensor ($g_z \gg g_x, g_y$) allows one to use the above Hamiltonian without taking the interactions into account. The quasidoublet of the non-Kramers ion Tm^{3+} in the KTm $(MoO_4)_2$ crystal consists of two close-lying singlet levels that are separated from the higher levels E_i by a rather large energy interval (200 cm^{-1}).[8] In this case, as we have shown above, only the lowest quasidoublet plays a major role in the formation of the ESR spectrum at low temperatures ($T \ll E_i$). In the case of a strict orientation of the magnetic field the principal values of the g tensor are $g_z=13.9\pm0.1$, $g_x \leqslant 0.4$, and $g_y \leqslant 0.4$.

Ions with an extremely anisotropic g factor are called Ising ions to point up the fact that their behavior in a magnetic field is analogous to that of the spins in the Ising model.

Since the g-tensor ellipsoid has a pronounced Ising-like form, an important role in the description of the angular dependence of the spectrum will be played by the orientation of the axis of the maximum value of the g tensor relative to the direction of the external magnetic field or, in other words, the value of the projection made by the component g_z of the g-tensor ellipsoid on the plane of rotation of the external magnetic field. Using only simple geometric arguments, one can obtain the following expressions for the maximum values of these projections of the g factors on the coordinate planes:

ac plane: $g^2=g_z^2(\cos^2\theta+\sin^2\theta\cos^2\varphi)$;
bc plane: $g^2=g_z^2(\cos^2\theta+\sin^2\theta\sin^2\varphi)$;
ab plane: $g^2=g_z^2\sin^2\theta$.

The best fit of the experimental data presented in Figs. 1 and 2 is obtained for the following values of the parameters of the Tm^{3+} paramagnetic center: $g_x=0.3\pm0.2$, $g_y=0.3\pm0.2$, $g_z=13.9\pm0.1$, $\varphi=0$, and $\theta=(7.6\pm1)°$, where θ is the angle between the crystallographic axis c and the local magnetic axis z of the paramagnetic center, which is rotated in the ac plane. The functions calculated according to the given formulas are shown by the continuous curves in the figures and demonstrate good agreement with experiment.

The value obtained for g_z can be compared with the maximum value attainable for the Tm^{3+} ion. For this estimate we use the total angular momentum $J=6$ for the ground-state multiplet of the Tm^{3+} ion, which is characterized by a Landé factor $g_J=7/6$. The maximum possible magnetic moment p of a rare-earth ion is $g_J\mu_B[J(J+1)]^{1/2}=7.56\mu_B$, which, for an effective spin of the quasidoublet $S=1/2$, corresponds to a value $g_{\max}\approx 14$ and is therefore consistent with the value we obtained for g_z.

According to Ref. 9, the presence of lower singlet levels of the Tm^{3+} ion in the crystalline electric field leads to a substantial decrease of the resonance linewidth created by the magnetic dipole interactions with the electron spins, especially at very low temperatures and for highly anisotropic g factors, when the population of the lower level is considerably larger than that of the upper levels. For this reason, the broadening due to the dipole–dipole interactions of the electron magnetic moments practically vanishes. It is noteworthy that in one of the early papers[10] on the ESR of the rare-earth ion Tb^{3+} in $PbMoO_4$, for which the lowest state is a quasidoublet, it was noted that the ESR line was very narrow, but no theoretical explanation of the experiment was given.

Frequency–field dependence of the ESR spectrum of $KTm(MoO_4)_2$ for $H\|z$

The frequency–field curve of the ESR spectrum for $H\|z$ (Fig. 3) shows that the lowest ground state is a quasidoublet with a projection of the angular momentum J close to $m_J=\pm 6$. The observed ESR spectrum may be due solely to transitions between components of the ground-state quasidoublet ± 6. This would correspond to a g factor $g_z=13.95$.

The crystalline field of the $KTm(MoO_4)_2$ crystal forms a doublet and a singlet structure of energy levels. The main contribution to the formation of the state is given by the high-symmetry components of the field, and their signs are such that the ground state is a quasidoublet with spin projections ± 6. The low-symmetry components will cause a mixing of different states, which will lead, in particular, to an initial splitting of the ground state. A magnetic field changes this splitting according to the law $\nu^2=\nu_0^2+(g_zH/2)^2$, where $\nu_0=69.95$ GHz. The functions corresponding to these parameters are shown by the continuous curves in Fig. 3.

CONCLUSIONS

To summarize, our investigation of the ESR spectra of Tm^{3+} ions in single-crystal $KTm(MoO_4)_2$ has yielded the following results.

1. We detected two magnetically inequivalent Tm^{3+} paramagnetic centers in the $KTm(MoO_4)_2$ crystal lattice. We determined the angle of rotation of the local magnetic axes of these centers ($2\theta=15.2°$).

2. We determined the g factors of the ground-state quasidoublet in the crystal. The strong anisotropy of the g factors allows us to classify the Tm^{3+} ion in the compound $KTm(MoO_4)_2$ as an Ising ion, and the spin–spin interaction will also be purely Ising-like.

3. We have determined the value of the initial splitting of the ground-state quasidoublet in the crystal ($\Delta E=2.3$ cm^{-1}).

The authors thank A. A. Loginov for helpful discussions of the results of this study.

*E-mail: kobets@ilt.kharkov.ua

---

[1] J. Hanuza and L. Macalik, Acta Part A(GB) **38A**, 61 (1982).
[2] R. F. Klevtsova and S. V. Borisov, Dokl. Akad. Nauk SSSR **177**, 1333 (1967) [Sov. Phys. Dokl. **12**, 1095 (1968)].
[3] V. I. Spitsyn and V. K. Trunov, Dokl. Akad. Nauk **185**, 854 (1969).
[4] V. A. Bagulya, A. I. Zvyagin, A. N. Zaika, M. I. Kobets, and A. A. Stepanov, Fiz. Nizk. Temp. **14**, 493 (1988) [Sov. J. Low Temp. Phys. **14**, 270 (1988)].
[5] A. M. Pshisukha, A. S. Chernyĭ, and A. I. Zvyagin, Fiz. Nizk. Temp. **1**, 473 (1975) [Sov. J. Low Temp. Phys. **1**, 233 (1975)].
[6] A. K. Zvezdin, V. M. Matveev, A. A. Mukhin, and A. I. Popov, *Rare-Earth Ions in Magnetically Ordered Crystals* [in Russian], Nauka, Moscow (1985), p. 56.
[7] J. S. Griffiths, Phys. Rev. **132**, 316 (1963).
[8] M. I. Kobets, V. V. Kurnosov, V. A. Pashchenko, and E. N. Khats'ko, Fiz. Nizk. Temp. **25**, 512 (1999) [Low Temp. Phys. **25**, 379 (1999)].
[9] S. A. Al'tshuler, R. M. Mineeva, Fiz. Tverd. Tela (Leningrad) **7**, 310 (1965) [Sov. Phys. Solid State **7**, 247 (1965)].
[10] A. A. Antipin, I. N. Kurkin, V. G. Stepanov, and L. Ya. Shekun, Fiz. Tverd. Tela (Leningrad) **7**, 985 (1965) [Sov. Phys. Solid State **7**, 792 (1965)].

Translated by Steve Torstveit

LOW TEMPERATURE PHYSICS VOLUME 26, NUMBER 4 APRIL 2000

LOW-DIMENSIONAL AND DISORDERED SYSTEMS

Influence of a biquadratic interaction on the magnetic ordering in two-dimensional ferromagnets

Yu. A. Fridman and D. V. Spirin

*V. I. Vernadskiĭ Tavricheskiĭ National University, ul. Yaltinskaya 4, 95007 Simferopol, Ukraine**

(Submitted September 13, 1999; revised October 18, 1999)
Fiz. Nizk. Temp. **26**, 374–379 (April 2000)

The question of whether the long-range magnetic order in a two-dimensional ferromagnet can be stabilized by the inclusion of a biquadratic interaction is investigated. It is shown that the stabilization of the long-range magnetic order results from the presence of a magnetoelastic interaction. Certain types of spin configurations in the system under study are investigated for different relative sizes of the Heisenberg and biquadratic exchange constants. © *2000 American Institute of Physics.* [S1063-777X(00)00804-5]

INTRODUCTION

For many years the Heisenberg model has served as the foundation on which the theory of magnetism has been developed. Since the state of an atom in a magnet with localized spins is determined by the direction of its spin, in an isotropic space the energy of interaction of two atoms can depend only on the scalar product of the spins of these atoms. In the Heisenberg Hamiltonian this dependence is assumed linear.

Of course, the Heisenberg Hamiltonian, being bilinear in the spins and, hence, two-centered, is by no means the most general form of Hamiltonian for a magnet with localized spins. The Heisenberg Hamiltonian can be generalized in different ways. First, while remaining in the framework of a structure which is bilinear in the spins, one can include various types of relativistic interactions (anisotropy, magnetoelastic interaction, etc.). However, it is also possible to go beyond the confines of a bilinear exchange interaction. Such a generalization of the Heisenberg model is possible, e.g., by taking into account the higher invariants in the spin variables. The simplest model of such a magnet incorporates a biquadratic interaction in the exchange Hamiltonian.[1]

The most interesting property of such a magnet is its magnetic polymorphism. The largest number of phases (14) has been observed in CeBi. Previously ‘‘order–order’’ phase transitions have ordinarily been explained as being due to Kittel exchange inversion (a change in sign of the exchange integral on account of thermal expansion of the lattice).[2] However, this theory is clearly unsuited to low-temperature transitions and is completely unable to explain the whole cascade of such transitions that can be brought about by exchange interactions of higher orders in the spin. An argument in favor of this mechanism is the fact that ‘‘order–order’’ transitions are most often observed in materials with non-Heisenberg structures.

The influence of non-Heisenberg exchange has been investigated quite actively in three-dimensional (3D) magnets.[3–5] However, we are unaware of any papers that have explored the influence of an exchange interaction of higher order in the spin on the stabilization of the long-range magnetic order in two-dimensional (2D) magnets or that have investigated ways that magnetic phases could be realized in them. Analysis of this question is the subject of the present paper. We explore the possibility of stabilization of the long-range magnetic order for different relationships among the values of the material constants. Incorporating a large biquadratic interaction (exceeding the Heisenberg interaction) gives rise to the appearance of a nonzero order parameter, but which is tensor rather than vector.

DISPERSION RELATION OF COUPLED MAGNETOELASTIC WAVES IN A TWO-DIMENSIONAL FERROMAGNET WITH BIQUADRATIC EXCHANGE

Let us consider a 2D ferromagnet with biquadratic exchange and ‘‘easy plane’’ anisotropy. It has been shown previously[6,7] that the long-range magnetic order in a 2D ferromagnet is stabilized by a magnetoelastic interaction. Incorporating a magnetoelastic interaction will lead to the existence, in the ferromagnetic phase, of a nonzero magnetic moment $\langle S^z \rangle$ in the plane of the ferromagnet; thus one can investigate the contribution of a biquadratic interaction both to the spectra of quasiparticles and to the process of stabilization of the long-range magnetic order.

We write the Hamiltonian of the system in the form

$$H=-\frac{1}{2}\sum_{n,n'}[J_{nn'}\mathbf{S}_n\mathbf{S}_{n'}+K_{nn'}(\mathbf{S}_n\mathbf{S}_{n'})^2]+\frac{\beta}{2}\sum_n (S_n^y)^2 +\lambda\sum_n [u_{xx}(S_n^x)^2+u_{zz}(S_n^z)^2+u_{xz}(S_n^zS_n^x+S_n^x+S_n^z)] +\frac{E}{2(1-\sigma^2)}\int dr[u_{xx}^2+u_{zz}^2+2\sigma u_{xx}u_{zz}+2(1-\sigma)u_{xz}^2], \tag{1}$$

where $J_{nn'}$ and $K_{nn'}$ are the bilinear and biquadratic exchange constants, $\beta>0$ is the single-ion anisotropy (SA) constant, λ is the magnetoelastic constant, u_{ij} are the symmetric parts of the components of the strain tensor, E is

Young's modulus, and σ is Poisson's ratio. We shall henceforth assume that the magnetic ion has spin $S=1$.

Separating out the mean field $\langle S^z\rangle$ and the additional fields q_2^p $(p=0,2)$ determined by the quadrupole moment, we obtain the one-site Hamiltonian $H_0(n)$:

$$H_0(n)=-\bar{H}S_n^z-B_2^0Q_{2n}^0-B_2^2Q_{2n}^2+\frac{\beta}{2}(S_n^y)^2+\lambda u_{xx}(S_n^x)^2 +\lambda u_{zz}(S_n^z)^2+\lambda u_{xz}(S_n^xS_n^z+S_n^zS_n^x), \tag{2}$$

where

$$\bar{H}=\langle S^z\rangle\left(J_0-\frac{K_0}{2}\right);\quad B_2^0=\frac{1}{6}K_0q_2^0;$$

$$B_2^2=\frac{1}{2}K_0q_2^2;\quad q_2^p=\langle Q_2^p\rangle;$$

$$Q_{2n}^0=3(S_n^z)^2-2;\quad Q_{2n}^2=\frac{1}{2}[(S_n^+)^2+(S_n^-)^2].$$

Solving the single-ion problem using Hamiltonian (2), we obtain the energy levels of the magnetic ion:

$$E_1=\frac{\beta}{4}+\frac{\lambda}{2}(u_{xx}^{(0)}+2u_{zz}^{(0)})-B_2^0-\chi,$$

$$E_0=\frac{\beta}{2}+\lambda u_{xx}^{(0)}+2B_2^0,$$

$$E_{-1}=\frac{\beta}{4}+\frac{\lambda}{2}(u_{xx}^{(0)}+2u_{zz}^{(0)})-B_2^0+\chi,$$

$$\chi^2=\bar{H}^2+\left(\frac{\lambda}{2}u_{xx}^{(0)}-\frac{\beta}{4}-B_2^2\right)^2. \tag{3}$$

The spontaneous strains are determined from the condition that the free energy density be minimum; they have the values

$$u_{xx}^{(0)}=-\frac{\lambda}{E}\frac{1-2\sigma}{2},\quad u_{zz}^{(0)}=-\frac{\lambda}{E}\frac{2-\sigma}{2},\quad u_{xz}^{(0)}=0.$$

In the basis of eigenfunctions of the Hamiltonian $H_0(n)$ we construct the Hubbard operators $X^{M'M}\equiv|\Psi(M')\rangle\langle\Psi(M)|$, which describe the transition of the magnetic ion from the state M' to the state M.[8,9] In terms of the Hubbard operators, Hamiltonian (2) is diagonal, and the spin operators are related to the Hubbard operators by the expressions

$$S_n^+=\sqrt{2}\cos\delta(X_n^{10}+X_n^{0-1})+\sqrt{2}\sin\delta(X_n^{01}-X_n^{-10}),$$

$$S_n^-=(S_n^+)^+, \tag{4}$$

$$S_n^z=\cos(2\delta)(H_n^1-H_n^{-1})-\sin(2\delta)(X_n^{1-1}+X_n^{-11}),$$

$$\cos\delta=\frac{B_2^2-\lambda u_{xx}^{(0)}/2+\beta/4}{\sqrt{(\chi-\bar{H})^2+(B_2^2-\lambda u_{xx}^{(0)}/2+\beta/4)^2}}.$$

After quantizing the dynamic part of the strain tensor in the standard way[10] and separating out in the one-site Hamiltonian (2) the terms proportional to the dynamic part of the strain tensor, we obtain a Hamiltonian describing processes of transformation of magnons into phonons and vice versa:

$$H_{\mathrm{tr}}=\sum_n\left(\sum_M P_MH_n^M+\sum_\alpha P_\alpha X_n^\alpha\right),$$

$$P_{M(\alpha)}=\frac{1}{\sqrt{N}}\sum_{q,\lambda}(b_{q,\lambda}+b_{-q,\lambda}^+)T_n^{M(\alpha)}(q,\lambda),$$

where N is the number of lattice sites, $b_{q,\lambda}$ and $b_{q,\lambda}^+$ are the creation and annihilation operators for phonons with polarization λ and wave vector $\mathbf{q}$, and $T_n^{M(\alpha)}(q,\lambda)$ are the amplitudes of the transformations:

$$T_n^{01}(q,\lambda)=T_n^{10}(q,\lambda)=\frac{\lambda}{2\sqrt{2}}T_n^0(q,\lambda)(e_\lambda^zq_x+e_\lambda^xq_z) \times(\cos\delta-\sin\delta),$$

$$T_n^{0-1}(q,\lambda)=T_n^{-10}(q,\lambda)=-\frac{\lambda}{2\sqrt{2}}T_n^0(q,\lambda)(e_\lambda^zq_x+e_\lambda^xq_z) \times(\cos\delta+\sin\delta),$$

$$T_n^0(q,\lambda)=i\frac{\exp(iqn)}{\sqrt{2m\omega_\lambda(q)}},$$

where m is the mass of the magnetic ion, $\omega_\lambda(q)$ is the dispersion relation for λ-polarized sound, $\omega_\lambda(q)=c_\lambda q$, and c_λ is the sound velocity. The calculations below will be done in the mean-field approximation, and we shall therefore need only the ''transverse'' part of the exchange Hamiltonian, which has the form

$$H_{int}^\perp=-\frac{1}{2}\sum_{\substack{n,n'\\ \alpha,\beta}}\{\mathbf{C}(\alpha),\hat{A}_{nn'}\mathbf{C}(\beta)\}X_n^\alpha X_n^\beta,$$

where $\mathbf{C}(\alpha)$ is an eight-dimensional vector having the following components:

$$C(\alpha)=[\gamma_1^\parallel(\alpha);\gamma_1^\perp(\alpha);\gamma_1^{*\perp}(-\alpha);\gamma_2^\parallel(\alpha);\gamma_2^\perp(\alpha)\gamma_2^{*\perp} (-\alpha);\gamma_3^\perp(\alpha);\gamma_3^{*\perp}(-\alpha)],$$

and the 8×8 matrix $\hat{A}_{nn'}$ decomposes into the direct sum of two matrices:

$$\hat{A}_{nn'}=\hat{A}_{nn'}^{(3)}\otimes\hat{A}_{nn'}^{(5)},$$

$$\hat{A}_{nn'}^{(3)}=\left\{J_{nn'}-\frac{1}{2}K_{nn'}\right\}\begin{pmatrix}1&0&0\\0&0&1/2\\0&1/2&0\end{pmatrix},$$

$$\hat{A}_{nn'}^{(5)}=\frac{1}{2}K_{nn'}\begin{pmatrix}1&0&0&0&0\\0&0&1/2&0&0\\0&1/2&0&0&0\\0&0&0&0&1/2\\0&0&0&1/2&0\end{pmatrix}.$$

The functions $\gamma^{\parallel\perp}(\alpha)$ are determined from the relation between the spin operators and Hubbard operators (4), and the following functions γ turn out to have nonzero values:

$$\gamma_1^\parallel(1-1)=\gamma_1^\parallel(-11)=-\sin2\delta,$$

$$\gamma_1^\perp(10)=\gamma_1^\perp(0-1)=\sqrt{2}\cos\delta,$$

$$\gamma_1^{\perp}(01) = -\gamma_1^{\perp}(-10) = \sqrt{2}\sin\delta,$$
$$\gamma_3^{\perp}(10) = -\gamma_3^{\perp}(0-1) = \sqrt{2}\cos\delta,$$
$$\gamma_3^{\perp}(01) = \gamma_3^{\perp}(-10) = -\sqrt{2}\sin\delta,$$
$$\gamma_2^{\perp}(1-1) = 2\cos^2\delta, \quad \gamma_2^{1}(-11) = -2\sin^2\delta. \tag{5}$$

The dispersion relation of coupled magnetoelastic waves can be obtained from an equation of the Larkin type for the Green function:[5]

$$\begin{aligned}\det\| \delta_{ij} &+ G_0^{\alpha} b(\alpha) a_{ik}(\alpha) A_{kj} \\ &+ B^0(q;\lambda,\lambda') T_{q,\lambda}^{-\alpha} G_0^{\alpha} b(\alpha) T_{-q,\lambda'}^{\beta}, \\ &\times G_0^{B} b(\beta) a_{ik}(\alpha,\beta) A_{kj}\| = 0,\end{aligned} \tag{6}$$

where $D_\lambda(q,\omega) = 2\omega_\lambda(q)/\omega^2 - \omega_\lambda^2(q)$ is the Green function of a λ-polarized phonon;

$$B^0(q;\lambda,\lambda') = \frac{D_\lambda(q,\omega)}{1 - Q_{\lambda\lambda'} D_\lambda(q,\omega)};$$

$$Q_{\lambda\lambda'} = T_{-q,\lambda'}^{\alpha}, G_0^{\alpha} b(\alpha) T_{q,\lambda}^{-\alpha};$$

$$a_{ik}(\alpha,\beta) = C_{ir}(\alpha) C_{rk}(-\beta); a_{ik}(\alpha) = a_{ik}(\alpha,\alpha);$$

$b(\alpha) = \langle \boldsymbol{\alpha} \cdot \mathbf{H} \rangle_0$ are terminal multipliers, and

$$\mathbf{H} = (X^{11}, X^{00}, X^{-1-1}).$$

The solutions of equation (6) determine the spectra of hybridized elementary excitations for arbitrary values of the single-ion anisotropy constants and biquadratic exchange and for arbitrary temperatures.

SPECTRA OF COUPLED MAGNETOELASTIC WAVES AND THE SPIN CONFIGURATIONS OF A TWO-DIMENSIONAL FERROMAGNET WITH BIQUADRATIC EXCHANGE FOR VARIOUS RELATIONSHIPS AMONG THE MATERIAL CONSTANTS

Let us restrict discussion to the case of low temperatures ($T \ll T_C$, where T_C is the Curie temperature), for which we can most simply and clearly describe the behavior of the system. In this situation the spectrum of quasimagnons has the form

$$\begin{aligned}\omega^2 = [&E_{10} + J_q - \sin(2\delta)(J_q - K_q)] \\ &\times [E_{10} + J_q + \sin(2\delta)(J_q - K_q)],\end{aligned} \tag{7}$$

where $E_{10} = E_1 - E_0$, and the values of the mean spin and quadrupole moments are determined from the equations

$$\langle S^z \rangle \approx \cos(2\delta), \quad q_2^0 \approx 1, \quad q_2^2 \approx \sin(2\delta). \tag{8}$$

From the last expression in (8) we can obtain an exact equation for $x \equiv q_2^2$:

$$\begin{aligned}x^6\left(\frac{K_0^4}{4}\right) &- x^5(2K_0^3\Delta) + x^4\left(K_0^2\overline{H}^2 + 6K_0^2\Delta^2 - \frac{K_0^4}{4}\right) \\ &+ x^3(2K_0^3\Delta - 8K_0\Delta^3 - 4K_0\overline{H}^2\Delta) + x^2(4\Delta^4 \\ &- 6K_0^2\Delta^2) + 4\overline{H}^2\Delta^2) + x(8K_0\Delta^3) - 4\Delta^4 = 0,\end{aligned}$$

where $\Delta \equiv -\beta/4 - \lambda^2(1-2\sigma)/4E$.

It is easy to see that one of the solutions for arbitrary values of the parameter of the system is $q_2^2 = 1$, which corresponds to the realization of a quadrupolar phase ($\langle S^z \rangle = 0$).

Here we define the quadrupolar phase as follows:[11]

$$\langle S^z \rangle = 0, \quad q_2^0 = 1, \quad q_2^2 = 1, \tag{9}$$

and we shall denote it below as the QP_1 phase, while the quadrupolar phase characterized by the following parameters (see, e.g., Ref. 12)

$$\langle S^z \rangle = 0, \quad q_2^0 = -2, \quad q_2^2 = 0 \tag{10}$$

will be called the QP_2 phase.

The possibility that long-range magnetic order exists is determined by the smallness of the fluctuations of the magnetic moment, i.e., the convergence of the fluctuation integral.[5] For calculation of the fluctuations of the magnetic moment we go over to a Bose description, using the method of bosonization of the Hubbard operators.[13] We associate with the operators X_n^α the pseudo-Hubbard operators $\tilde{X}_n^\alpha$, which are related to the Bose creation and annihilation operators for quasiparticles as follows:

$$\tilde{X}_n^{10} = (1 - a_n^+ a_n - b_n^+ b_n) a_n, \tilde{X}_n^{01} = a_n^+,$$
$$\tilde{X}_n^{1-1} = (1 - a_n^+ a_n - b_n^+ b_n) b_n, \tilde{X}_n^{-11} = b_n^+,$$
$$\overline{X}_n^{0-1} = a_n^+ b_n, \tilde{X}_n^{-10} = b_n^+ a_n, \tilde{X}_n^{00} = a_n^+ a_n,$$
$$\tilde{X}_n^{-1-1} = b_n^+ b_n, \overline{X}_n^{11} = 1 - a_n^+ a_n - b_n^+ b_n, \tag{11}$$

where a_n and b_n are the Bose operators corresponding to the transitions $|1\rangle \to |0\rangle$, $|0\rangle \to |1\rangle$, and $|1\rangle \to |-1\rangle$, $|-1\rangle \to |1\rangle$.

It is easy to show that the fluctuation integral will now have the form

$$\begin{aligned}\langle (S^x)^2 \rangle &\propto \frac{1}{N} \sum_n \langle a_n^+ a_n \rangle \\ &\propto \frac{1}{(2\pi)^d} \int_0^\infty \frac{q^{d-1} dq}{\omega_q[\exp(\omega_q/T) - 1]}.\end{aligned} \tag{12}$$

Let us consider some different cases corresponding to possible relationships among the parameters of the system under study.

1. Suppose that $\lambda = \beta = 0$. Then, depending on the relative sizes of J_0 and K_0, there are two situations:

a) $J_0 > K_0$. In this case the magnon spectrum has the form

$$\omega = \alpha q^2, \tag{13}$$

where $\alpha = J_0 R_0^2$ (R_0 is the interaction radius). Expression (12) for the fluctuation integral simplifies to

$$\langle (S^x)^2 \rangle \propto \frac{1}{N} \sum_n \langle a_n^+ a_n \rangle \propto \frac{1}{(2\pi)^d} \int_0^\infty \frac{q^{d-1} dq}{\exp(\omega_q/T) - 1}. \tag{14}$$

For this relationship among the material constants there is no long-range magnetic order in a 2D ferromagnet (on account of the divergence of (14) at the lower limit), while in a 3D ferromagnet a ferromagnetic phase is realized in the system.

b) $J_0 < K_0$.

Here $\omega^2 = 2(K_0 - J_0) p q^2$, (15)

where $\rho = K_0 R_0^2$. Although the magnon spectrum is linear in q, the presence of the multiplicative factor $1/\omega_q$ (which is due to the $u-v$ transformation) in the fluctuation integral causes this integral, as before, to diverge for a 2D ferromagnet, and a quadrupolar phase does not exist in the system, whereas for a 3D ferromagnet the quadrupolar order is stabilized.

2. Now suppose that $\lambda \neq 0$, $\beta \ll J_0$. We again consider two cases:

a) $J_0 > K_0$. In this case the solution of equation (8) can be found approximately, and it has the form $q_2^2 \approx \beta/4J_0$. A ferromagnetic phase $\langle S^z \rangle = 1$, $q_2^2 \ll 1$ is realized in a 2D ferromagnet, and a magnetoelastic gap appears in the quasimagnon spectrum:

$$\omega^2 = (b_0 + \alpha q^2)(b_0 + \beta/2 + \alpha q^2). \tag{16}$$

Here $b_0 = 3\lambda^2/4E$. As a result, the fluctuation integral converges, and long-range magnetic order is stabilized in the 2D system by virtue of the existence of a magnetoelastic gap in the quasimagnon spectrum.

b) $J_0 < K_0$. In this case the QP_1 phase is realized in the system, and the quasimagnon spectrum is modified, with a gap appearing in it on account of the single-ion anisotropy and the magnetoelastic interaction:

$$\omega^2 = (c_0 + \rho q^2)(c_0 + 2K_0 - 2J_0),$$

$$c_0 = \frac{\lambda^2}{2E}(2 - \sigma) + \frac{\beta}{2}. \tag{17}$$

As a result, even in the absence of a magnetoelastic interaction the quadrupolar order is stabilized in a 2D ferromagnet for $J_0 < K_0$.

The QP_1 phase can be brought about by single-ion anisotropy in addition to biquadratic exchange, and the existence region of the QP_1 phase is determined from the inequality

$$c_0 + 2K_0 - 2J_0 > 0.$$

The spectrum of quasiphonons (the wave vector $\mathbf{q}$ is parallel to the OY axis, t polarization) is determined by equation (6) and has the form

$$\omega^2 = \omega_t^2 \left\{ 1 + \frac{a_0}{E_{10} + J_0 + \sin(2\delta)(J_0 - K_0)} \right\},$$

$$a_0 = \frac{\lambda^2(1+\sigma)}{2E}[1 - \sin(2\delta)]. \tag{18}$$

In the ferromagnetic phase ($\sin(2\delta) \approx 0$) we have

$$\omega^2 = \omega_t^2 \left\{ 1 - a_0 \left[b_0 + \beta/4 + \left(\frac{\lambda^2(1-2\sigma)}{4E} + \frac{\beta}{4} + \frac{K_0}{2} \right) \times \left(J_0 - \frac{K_0}{2} \right)^{-1} \right]^{-1} \right\}.$$

In the QP_1 phase $\sin(2\delta) = 1$, and renormalization of the sound velocity does not take place:

$$\omega = \omega_t.$$

We note that an inversion of the energy levels can occur in the system under study. It follows from (3) that for

$$K_0 - \frac{1}{2}\beta - \frac{\lambda^2}{2E}(2 - \sigma) > 0$$

the lowest energy level is E_0. Calculations show that in this case spin waves do not arise in the system, and the 2D ferromagnet is found in a paramagnetic state.

CONCLUSION

In summary, if in a 2D ferromagnet one ignores the single-ion anisotropy and the magnetoelastic interaction, long-range magnetic order does not exist in the system for any relationship between the Heisenberg and biquadratic exchange constants. When the magnetoelastic interaction is taken into account a stabilization of the long-range magnetic order occurs in the system under study. However, the type of magnetic ordering depends on the relative sizes of the material constants. For $K_0 \ll J_0$ a ferromagnetic phase is realized in the system. In the opposite case ($K_0 > J_0$) a phase with a tensor order parameter, a quadrupolar (QP) phase, is realized in a two-dimensional ferromagnet. It should be noted that for such a relationship between the material constants the QP phase exists even in the absence of magnetoelastic coupling. This is a consequence of including both single-ion anisotropy and a biquadratic interaction.

Since the two-dimensionality of the system is taken into account explicitly only in the magnetoelastic interaction and in the calculation of the fluctuation integrals, the results obtained here can easily be generalized to the case of a 3D ferromagnet with a biquadratic interaction. In particular, it can be shown that in 2D and 3D ferromagnets in the absence of an external magnetic field, if the biquadratic exchange constant is larger than the Heisenberg exchange constant, the QP_1 phase, which is characterized by ordering of the antiferromagnetic type,[1] is realized. This is because the wave function corresponding to the energetically most favorable state of the magnetic ion has the form

$$\Psi(1) = \frac{1}{\sqrt{2}}|\rangle + \frac{1}{\sqrt{2}}|-1\rangle,$$

and thus the probabilities of finding the spin in one of the states $|1\rangle$ or $|-1\rangle$ are equal. The mechanism for realization of the QP_2 phase is different. It is due to inversion of the energy levels, as a result of which the lowest energy level becomes E_0 and the ground state is described by a wave function

$$\Psi(0) = |0\rangle.$$

In this case the ordering of the system reduces to one in which the the spins r ‘‘laid’’ in the basal plane, where they are oriented in an arbitrary way. Although such a phase can be realized in 3D systems (see, e.g., Ref. 11), it cannot exist in a 2D system.

[*] E-mail: man@expl.cris.crimea.ua

---

[1] É. L. Nagaev, *Magnets with Complicated Exchange Interactions* [in Russian], Nauka, Moscow (1988).
[2] N. P. Grazhdankina, Usp. Fiz. Nauk **96**, 291 (1968) [Sov. Phys. Usp. **11**, 727 (1969)].
[3] V. V. Val'kov and G. N. Matsuleva, Preprint No. 596 [in Russian], Institute of Physics, Siberian Branch of the Academy of Sciences of the USSR, Krasnoyarsk (1989).
[4] V. V. Val'kov and G. N. Matsuleva, Preprint No. 645F [in Russian], Institute of Physics, Siberian Branch of the Academy of Sciences of the USSR, Krasnoyarsk (1990).
[5] Yu. N. Mitsaĭ, A. N. Maĭorova, and Yu. A. Fridman, Fiz. Tverd. Tela (Leningrad) **34**, 66 (1992) [Sov. Phys. Solid State **34**, 34 (1992)].
[6] B. A. Ivanov and E. V. Tartakovskaya, JETP Lett. **63**, 835 (1996).
[7] Yu. N. Mitsaĭ, Yu. A. Fridman, D. V. Spirin, and K. N. Alekseev, Uchen. Zap. SGU **7(46)**, 139 (1998).
[8] R. O. Zaĭtsev, Zh. Éksp. Teor. Fiz. **68**, 207 (1975) [Sov. Phys. JETP **41**, 100 (1975)].
[9] V. M. Loktev and V. S. Ostrovskiĭ, Fiz. Tverd. Tela (Leningrad) **20**, 3086 (1978) [Sov. Phys. Solid State **20**, 1779 (1978)].
[10] L. D. Landau and E. M. Lifshitz, *Statistical Physics*, 3rd ed. [Pergamon Press, Oxford (1980); Nauka, Moscow (1976)].
[11] V. V. Val'kov, G. N. Matsuleva, and S. G. Ovshinnikov, Fiz. Tverd. Tela (Leningrad) **31**, 60 (1989) [Sov. Phys. Solid State **31**, 948 (1989)].
[12] F. P. Onufrieva, Zh. Éksp. Teor. Fiz. **94**(2), 232 (1988) [Sov. Phys. JETP **67**, 346 (1988)].
[13] V. V. Val'kov and T. A. Val'kova, Preprint No. 644F [in Russian], Institute of Physics, Siberian Branch of the Academy of Sciences of the USSR, Krasnoyarsk (1990).

Translated by Steve Torstveit

Heat transfer in the orientationally disordered phase of SF_6

O. I. Purskiĭ and N. N. Zholonko

Cherkassy Engineering and Technology Institute, bul'var Shevchenko 460, 257006 Cherkassy, Ukraine

V. A. Konstantinov*

B. I. Verkin Physicotechnical Institute for Low Temperature Physics, National Academy of Sciences of Ukraine, Lenin prospect, 47, 61164 Kharkov, Ukraine

(Submitted September 30, 1999; revised December 1, 1999)
Fiz. Nizk. Temp. **26**, 380–384 (April 2000)

The isobaric thermal conductivity of solid SF_6 is investigated in the high-temperature phase. The experimental results are rescaled to a constant density. The isochoric thermal conductivity initially decreases with increasing temperature, then passes through a smooth minimum and begins to grow. A modified version of the reduced coordinate method is used to calculate the phonon–phonon and phonon–rotational contributions to the total thermal resistance. The growth of the isochoric thermal conductivity is explained by a weakening of the scattering of phonons on collective rotational excitations of the molecules as the correlations of the rotation weaken. © *2000 American Institute of Physics.* [S1063-777X(00)00904-X]

Sulfur hexafluoride is often classified as a material having a plastic crystalline phase. However, the nature of the orientational disorder in the high-temperature phase of SF_6 is somewhat different than in the plastic phases of other molecular crystals, where the symmetries of the molecule and environment do not match. Ordinarily for crystals whose molecules have orientational freedom, there are a number of orientations available to a molecule, and it can go from one orientation to another. In individual cases the limit of this reorientational motion can be continuous rotation. Quite often an increase in the orientational mobility comes about because of a phase change or transition. The presence or absence of a transition is determined, as a rule, by whether or not the possible orientations are distinguishable, i.e., it depends on the interrelationship of the symmetry of the molecule and the symmetry of its position in the lattice.

The SF_6 molecule has octahedral symmetry. In the high-temperature β phase the molecules occupy sites of the bcc lattice of space symmetry 1_m3_m (Ref. 1–5). The existence region of the β phase is extraordinarily large: the crystallization of SF_6 occurs at 222.4 K, and the phase transition lowering the symmetry of the translational and orientational subsystems of the crystal does not occur until 94.3 K. The interaction between the nearest neighbors in the bcc phase tends to order the molecules so that their S–F bonds lie along the {100} direction, and in the interaction with the next-nearest neighbors a repulsion predominates between the fluorine atoms. The data from recent structural studies[3] indicate a strict orientational order in SF_6 above the phase transition temperature. This makes SF_6 different from such plastic crystals as CH_4, CCl_4, adamantane, etc., in which the destruction of the long-range order occurs immediately after the phase transition. The intensive growth of processes of orientational disordering begins in SF_6 only at temperatures above 150 K and is of a dynamic nature. The increase of the degree of orientational disorder as the temperature is raised is not a consequence of a simple increase in the amplitude of librations but is due to dynamic reorientations, which are facilitated by the frustration of the intermolecular interaction.[3–5] In view of what we have said, SF_6 is a convenient object for studying in a monophase, one-component system the influence of a broad spectrum of rotational states of the molecule on the thermal conductivity at the transition from practically complete orientational ordering to nearly free rotational motion.

To make the comparison of the experimental results with the theoretical predictions as correct as possible, the comparison must be done at constant volume in order to eliminate the influence of thermal expansion. Up till now the thermal conductivity of the solid phase of SF_6 has been studied only for several isochores in a narrow temperature interval near the melting point.[6] A growth of the isochoric thermal conductivity is observed as the temperature is raised, whereas the isobaric thermal conductivity decreases. The observed effect has been attributed to a weakening of the scattering of phonons on excitations of the rotational motion of the molecules as the correlations of their rotation becomes weaker. It is unquestionably of interest to expand the temperature interval of the thermal conductivity measurements all the way down to the phase transition at 94.3 K in order to span as wide as possible a spectrum of rotational excitations in SF_6. The thermal conductivity measured at the saturated vapor pressure can be rescaled to its isochoric counterpart with the use of the data on the thermal expansion[3] and the volume dependence of the thermal conductivity.[6]

In this paper we present the results of a study of the thermal conductivity of solid SF_6 by a steady-state planar method in the interval from the phase transition temperature 94.3 K to the melting point. The measurement ampoule, in which the sample was grown, was a tube of Kh18N9T stainless steel with a length of 70 mm and an inner diameter of 7.2 mm. The temperature sensors were germanium resistance thermometers and a copper–Constantan thermocouple, which were mounted on copper rings attached to the cell.

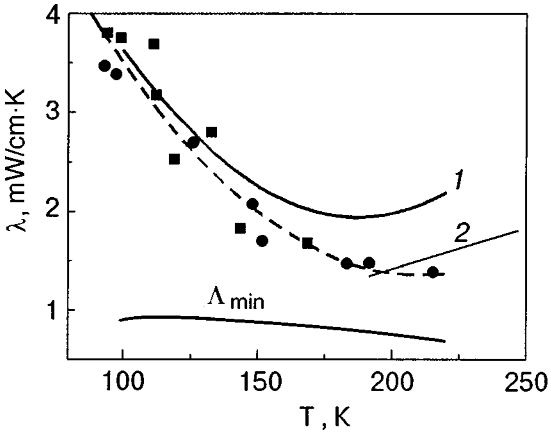

FIG. 1. Isochoric and isobaric thermal conductivities of solid SF_6 in the high-temperature phase. The symbols ■ and ● correspond to the two samples. Curve *1* is the thermal conductivity rescaled to a molar volume of 58.25 cm^3/mole. Line *2* is the data of Ref. 6 for a sample with a molar volume of 62.2 cm^3/mole. Also shown are the lower limit $\Lambda_{\min}$ of the thermal conductivity of solid SF_6, calculated for the isobaric case according to Cahill and Pohl, in the framework of the Einstein model of diffusional heat transfer directly from atom to atom.[9]

The measurements were made by a modified thermal potentiometer method,[7] which made it possible to minimize the error of determination of the thermal conductivity. Uncontrolled heat fluxes due to thermal radiation were reduced substantially with the aid of a radiation shield, on which a system of thermocouples and a precision temperature regulator reproduced the temperature field of the measuring cell. The sample was grown from the gas phase at a pressure of around 1.4 bar, with the temperature of the bottom of the measuring ampoule maintained close to the temperature of liquid nitrogen. The growth procedure took around 2 hours. Studies were done on two samples (the purity of the initial SF_6 was 99.98% or better). The overall error of the thermal conductivity measurement did not exceed 15%, the main part (10%) of which was systematic error and depended on the error with which the geometric dimensions of the ampoule were determined. The thermal conductivity of the two samples agreed within experimental error.

The results of the measurements are presented in Fig. 1 and Table I. The solid curve *1* shows the thermal conductivity rescaled to a molar volume of 58.25 cm^3/mole, which is the value for SF_6 above the phase transition temperature (94.3 K).[3] The calculation was done according to the formula[8]

$$\lambda_V=\lambda_P(V(T)/V_m)^g, \tag{1}$$

where λ_V and λ_P are the isochoric and isobaric thermal conductivities, respectively, $V(T)$ is the instantaneous value of the molar volume of a free sample, V_m is the molar volume to which the rescaling is done, and the Bridgman coefficient $g=-(\partial\ln\lambda/\partial\ln V)_T$ (according to the data of Ref. 6, it is equal to 5.2). The solid curve *2* shows the data of Ref. 6 for a sample with a molar volume of 62.2 cm^3/mole. The curve in the lower part of the figure is the lower limit of the thermal conductivity of solid SF_6, calculated for the isobaric case, according to Cahill and Pohl in the framework of the Einstein model for the diffusive transfer of heat directly from atom to atom:[9]

$$\Lambda_{\min}=\left(\frac{\pi}{6}\right)^{1/3}k_Bn^{2/3}\sum_i v_i\left\{\left(\frac{T}{\Theta_i}\right)^2\int_0^{\Theta_i T}\frac{x^3e^x}{(e^x-1)^2}dx\right\}. \tag{2}$$

TABLE I. Temperature dependence of the isobaric thermal conductivity of two samples of solid SF_6.

Sample No. 1		Sample No. 2	
T, K	λ, mW/cm·K	T, K	λ, mW/cm·K
94	3.81	93	3.46
99	3.75	97	3.38
111	3.68	126	2.69
112	3.17	148	2.07
119	2.53	152	1.70
132	2.80	183	1.47
143	1.83	191	1.48
168	1.68	215	1.40

The summation is over the three vibrational modes (two transverse and one longitudinal) with the sound velocities v_i; Θ_i is the limiting Debye frequency for each polarization, expressed in kelvins; $\Theta_i=v_i(\hbar/k_B)(6\pi^2n)^{1/3}$, where n is the number of atoms per unit volume, and k_B is Boltzmann's constant. The necessary data on the density and sound velocity for the calculation were taken from Ref. 3.

The isochoric thermal conductivity of solid SF_6 in the high-temperature β phase initially decreases with increasing temperature, then passes through a smooth minimum and starts to increase. Its behavior above 200 K is in good agreement with the data of Ref. 6 if the different density of the samples is taken into account. Interestingly, the character of the temperature dependence of the thermal conductivity of solid SF_6 is contrary to that of the plastic phase of solid methane.[10] In CH_4 (I) the isochoric thermal conductivity initially increases as the temperature is raised, and then it passes through a smooth maximum and decreases thereafter all the way to the melting point. It can also be seen from Fig. 1 that above 150 K the thermal conductivity of solid SF_6 approaches its lower limit, being no more than twice that value.

This circumstance has at least two important consequences. First, the proximity of the absolute value of the thermal conductivity to its lower limit gives us reason to expect that its temperature dependence is mainly determined by acoustical vibrations with small wave vectors. Experiments on the inelastic scattering of neutrons[4] and the data from molecular dynamics (MD) calculations[5] indicate the existence of well-defined acoustical phonons, which are strongly damped as one moves away from the center of the Brillouin zone. Second, one expects substantial deviations from the law $\lambda\propto 1/T$. This circumstance cannot, however, account for the growth of the thermal conductivity in the β phase of SF_6 at premelting temperatures.

To elucidate the reasons for such different behavior of the thermal conductivity in the high-temperature phases of methane and SF_6, in the present study we have undertaken to separate the phonon–phonon and phonon–rotational contributions to the total thermal conductivity of solid SF_6, much as this was done in the case of solid methane.[10] Here it was assumed that the heat is transferred mainly by translational

TABLE II. Reduced parameters and the molar weights for Kr, Xe, and SF_6.

Substance	T_{mol}, K	V_{mol}, $\mathrm{cm^3/mole}$	λ_{mol}, W/m·K	μ
Kr	209.4	92.01	0.124	83.8
Xe	289.7	119.5	0.100	131.3
SF_6	318.7	201.45	0.074	146.05

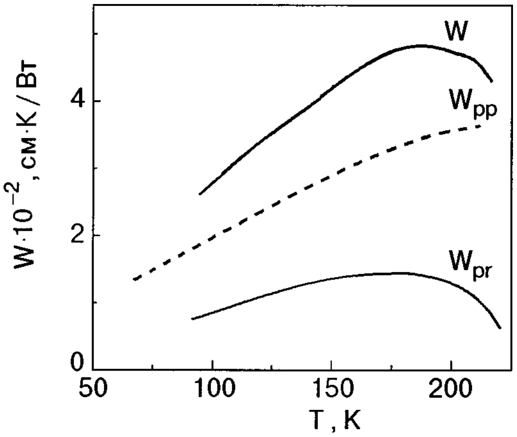

FIG. 2. Contributions of the phonon–phonon scattering (W_{pp}) and of the scattering of phonons on rotational excitations of the molecules (W_{pr}) to the total thermal resistance W of solid SF_6 with a molar volume of $58.25\ \mathrm{cm^3/mole}$.

vibrations, independent of the degree of orientational ordering. As we have mentioned earlier,[11] in orientationally ordered phases the role of librations in the heat transfer turns out to be insignificant on account of the small dispersion of the librational branches. In orientationally disordered phases the translational vibrations are the only well-defined excitations. The data were processed using a modified version of the method of reduced coordinates (see below). It is important to note that in this case there is no need to resort to some approximate model or other.

As a rule, the reducing parameters used are the values of $T_{\mathrm{mol}}=\varepsilon/k_B$, $\lambda_{\mathrm{mol}}=k_B/\sigma^2\sqrt{\varepsilon/\mu}$, and $V_{\mathrm{mol}}=N\sigma^3$, where σ and ε are the parameters of the Lennard-Jones potential, and μ is the molar weight. In this paper as the reducing parameters T_{mol} and V_{mol} we used the values of the temperatures and molar volumes of SF_6 and of solidified rare gases (krypton and xenon) at the critical points T_{cr} and V_{cr} (Table II).

The choice of the given parameters is explained as follows. For simple molecular substances, T_{cr} and V_{cr} are proportional to ε and σ^3, respectively. However, the accuracy of determination is much higher for the critical parameters than for the parameters of the binomial potential. We note that the quantities σ and ε depend substantially on the choice of binomial potential and the method used to determine it. Assuming that the total thermal resistance $W=1/\lambda$ of solid SF_6 is the sum of the phonon–phonon W_{pp} and phonon–rotational W_{pr} contributions and that in the reduced coordinates ($W^*=W/W_{\mathrm{mol}}$, $T^*=T/T_{\mathrm{mol}}$) the component due to the phonon–phonon scattering, W_{pp}, is the same as in solidified rare gases at equal values of the reduced molar volume $V^*=V/V_{\mathrm{mol}}$, one can isolate the phonon–phonon and phonon–rotational components of the thermal resistance.

The results of the calculation are presented in Fig. 2. The phonon–phonon component W_{pp} of the thermal resistance is practically (to within 2–3%) independent of the choice of rare gas used for comparison. Unlike the case of solid methane, in which the thermal resistance due to the presence of the rotational degrees of freedom of the molecules, W_{pr}, begins to decrease sharply immediately after the transition to the orientationally disordered phase and becomes practically equal to zero above 100 K (Ref. 10), for solid SF_6 the thermal resistance due to the presence of rotational degrees of freedom of the molecules initially increases as the temperature is raised, similarly to what occurs in the orientationally ordered phases of a number of simple molecular crystals.[9] This behavior can be attributed to additional scattering of phonons on collective rotational excitations, the density of which increases as the temperature is raised. This is in good agreement with the data of Ref. 3 indicating a rather strict orientational order in solid SF_6 immediately after the phase transition at 93.4 K, but it is at odds with the results of inelastic neutron scattering studies and with calculations by the molecular dynamics method.[4,5] In Ref. 5 the well-defined collective excitations due to the presence of rotational degrees of freedom of the molecules were not detected at all in solid SF_6 in any of the high-symmetry directions. At a temperature of around 170 K the phonon–rotational component of the thermal resistance passes through a maximum and begins to decrease. This again is in good agreement with the data of Ref. 3, according to which there is an intense growth of the processes of orientational disordering in the solid phase of SF_6 at temperatures above 150 K. The observed effect, as in the case of solid methane, can be attributed to a weakening of the scattering of phonons on collective rotational excitations of the SF_6 molecules as the correlations of their rotation becomes weaker. The additional contribution to the thermal resistance from the rotational degrees of freedom amounts to around 30% of the phonon–phonon component—much less than in solid methane immediately after the transition to the orientationally disordered phase[10] or in crystals of the nitrogen type.[12] The Brillouin scattering data[13] also attest to a weaker translational–rotational interaction in the solid phase of SF_6 in comparison with methane and other cubic crystals.

[*] E-mail: konstantinov@ilt.kharkov.ua

---

[1] J. Michel, M. Drifford, and P. Rigny, J. Chem. Phys. **67**, 31 (1970).
[2] G. Dolling, B. M. Powell, and V. F. Search, Mater. Chem. Phys. **37**, 1859 (1979).
[3] A. P. Isakina and A. I. Prokhvatilov, Fiz. Nizk. Temp. **19**, 201 (1993) [Low Temp. Phys. **19**, 142 (1993)].
[4] M. T. Dove and G. S. Pawley, J. Phys. C **17**, 6581 (1984).
[5] M. T. Dove, G. S. Pawley, G. Dolling, and B. M. Powell, Mol. Mater. **57**, 865 (1986).
[6] V. A. Konstaninov, V. G. Manzheliĭ, and S. A. Smirnov, Fiz. Nizk. Temp. **18**, 1290 (1992) [Sov. J. Low Temp. Phys. **18**, 902 (1992)].
[7] T. N. Antsygina, B. Ya. Gorodilov, N. N. Zholonko, A. I. Krivchikov, V. G. Manzheliĭ, and V. A. Slyusarev, Fiz. Nizk. Temp. **18**, 417 (1992) [Sov. J. Low Temp. Phys. **18**, 283 (1992)].
[8] V. A. Konstaninov, V. G. Manzheliĭ, M. A. Strzhemechnyĭ, and S. A. Smirnov, Fiz. Nizk. Temp. **14**, 90 (1988) [Sov. J. Low Temp. Phys. **14**, 48 (1988)].

[9] D. G. Cahill, S. K. Watson, and R. O. Pohl, Phys. Rev. B **46**, 6131 (1992).
[10] V. A. Konstantinov, V. G. Manzhelii, V. P. Revyakin, and S. A. Smirnov, Physica B **262**, 421 (1999).
[11] V. A. Konstantinov, V. G. Manzheliĭ, V. P. Revyakin, and S. A. Smirnov, Fiz. Nizk. Temp. **21**, 102 (1995) [Low Temp. Phys. **21**, 78 (1995)].
[12] V. A. Konstantinov, V. G. Manzheliĭ, S. A. Smirnov, and A. M. Tolkachev, Fiz. Nizk. Temp. **14**, 189 (1988) [Sov. J. Low Temp. Phys. **14**, 104 (1988)].
[13] H. Kniefte, R. Penney, and M. J. Clouter, J. Chem. Phys. **88**, 5846 (1998).

Translated by Steve Torstveit

Spontaneous onset of interaction anisotropy in a strongly correlated quasi-one-dimensional system of electrons

D. M. Apal'kov and A. A. Zvyagin

B. I. Verkin Physicothecnical Institute for Low Temperature Physics, National Academy of Sciences of Ukraine, Lenin prospect, 47, 61164 Kharkov, Ukraine

D. M. Apal'kov*

Kharkov State University, pl. Svobody 4, 61077 Kharkov, Ukraine

A. A. Zvyagin**

Max Planck Institut für Physik Komplexer Systeme, Nöthnitzer Str. 38, Dresden D-01187, Germany

(Submitted November 11, 1999)
Fiz. Nizk. Temp. **26**, 385–393 (April 2000)

Instability of a strongly correlated quasi-one-dimensional electron system in a real three-dimensional crystal is predicted, with the onset of anisotropy of the electron–electron interaction. The influence of an external magnetic field, the occupation of the electron band, and a small nonzero temperature on the predicted instability are investigated. © *2000 American Institute of Physics.* [S1063-777X(00)01004-5]

Low-dimensional electronic and magnetic systems have been attracting a heightened research interest, both theoretical and experimental, in recent years. In particular, crystals have been synthesized in which the electron bandwidth (and, hence, the Fermi velocity) and the interaction between electrons are tens of times larger along one of the crystallographic directions than along the others.[1] In these quasi-one-dimensional electron systems, owing to the presence of a one-dimensional feature in the density of states, quantum fluctuations are enhanced in comparison with the standard three-dimensional electron systems. Therefore, perturbative theoretical methods, such as perturbation theory or mean-field theory in their various modifications, are inapplicable, since they can lead to qualitatively incorrect results. The term ''strongly correlated electron system'' is ordinarily applied to systems for which the energy of the collectivized electrons (kinetic) is comparable in size to the energy of the electron–electron interaction (usually Coulomb). The latter can exist in strongly correlated electron systems both in the form of a scalar interaction between the charges of the electrons and in the form of an exchange interaction between their spins, and therefore both the charge (current) and magnetic characteristics are very important in these systems. Ordinarily the electron–electron correlations in one-dimensional systems of this kind are taken into account strictly by the use of rigorous methods such as the Bethe ansatz (or its algebraic version—the quantum inverse-scattering method).[2]

In this paper we investigate the stability of a strongly correlated quasi-one-dimensional electron system against the spontaneous onset of anisotropy in the electron–electron interactions. We shall show that the effect of the crystalline field of the ligands (the three-dimensional environment of a selected one-dimensional interacting electron chain in the crystal) makes the isotropic (Coulomb) interaction between electrons of the chain unstable with respect to the onset of anisotropy (both magnetic and charge), and we analyze how this instability is influenced by the value of the electron–lattice coupling, applied external voltage, the number of electrons in the chain, low temperatures, and an external magnetic field.

It has recently become clear that the orbital degrees of freedom play a fundamental role in the behavior of a number of strongly correlated electron systems. In the standard approach it is the orbital degrees of freedom of the electrons that react to the crystalline electric field of the ions forming the crystal lattice. The symmetry of this crystalline field is determined by the symmetry of the crystal lattice. Even if the ions surrounding a magnetic ion (the ligands) are nonmagnetic themselves, the electric field of the ligands will influence the spin behavior of the magnetic ions through the spin–orbit interaction (which is usually weak). Taking the crystalline electric field into account in the lowest approximation gives rise to magnetic anisotropy: the spin–spin interaction between electrons turns out to be different depending on its orientation with respect to the crystalline axes. The scalar interaction between the charges of the electrons can also be anisotropic as a result of the electric field of the ions of the crystal. The magnetic anisotropy can be both single-ion and inter-ion. For electrons with spin 1/2, of course, there is no single-ion anisotropy, and in this paper we shall therefore investigate only the effects of the inter-ion magnetic anisotropy.

The instabilities of dielectric magnetic chains with respect to the onset of magnetic anisotropy have been considered previously.[3,4] For example, the spontaneous onset of biaxial magnetic anisotropy in a highly anisotropic XY spin chain was predicted in Ref. 3 (the advantage of such a system from the standpoint of a theoretical description of its properties is that its Hamiltonian can be reduced to the Hamiltonian of a noninteracting lattice gas of spinless fermions by means of a nonlocal Jordan–Wigner transformation,[5] making it possible to obtain a number of exact results for the static thermodynamic characteristics of the system). This instability is analogous to the instability of an XY spin chain with respect to the spin–Peierls period doubling,[6] which has been observed for several inorganic compounds in recent years.[7] In the case of spin–Peierls period doubling this instability arises as a result of the interaction with a longitudinal phonon (a longitudinal displacement of the spins along the one-dimensional chain), whereas the onset of spontaneous magnetic anisotropy is due to the interaction (indirect) of the spins of the chain with a transverse phonon (transverse displacement of the ions) of the three-dimensional crystal lattice. In Ref. 4 it was predicted that a magnetic anisotropy of the easy plane type will arise in a dielectric crystal with a quasi-one-dimensional isotropic Heisenberg antiferromagnetic interaction between localized spins 1/2. In this case the one-dimensional system of spins is appreciably interacting, and therefore the problem of finding the energy levels for such a system (which are substantially nonequidistant) is considerably more complicated than for the case of an XY chain. In this paper we shall solve the more complicated problem in which the electrons in the chain have both spin and charge degrees of freedom, i.e., the sites of the chain can be occupied or empty (hole), and the number of electrons depends on the applied external voltage. This case, unlike the previous one,[4] corresponds to a conducting electron subsystem. Of course, when the (one-dimensional) band is half-filled by electrons, i.e., when one electron is found at each site, the problem reduces to the previous one. The charge (scalar) and exchange interactions between electrons found at neighboring sites of the chain (the preferred crystalline direction) leads to a substantially nonequidistant spectrum. Here, even in the low-temperature behavior of the electrons a substantial role is played by bound electron states, which are absent in a system with no electron–electron interaction, and this substantially complicates the problem.

Let us assume that the symmetry of the lattice of a three-dimensional crystal (one with quasi-one-dimensional electronic properties, i.e., the characteristic energies of the electron hops and interactions in one direction are large compared to the other directions) is altered as a result of a small displacement of the ions. Then, of course, the energy of its elastic subsystem will have increased. We shall take into account only uniform deformations of the lattice, which create an anisotropy of its electronic properties which is uniform along the entire quasi-one-dimensional system of electrons. In other words, the phonon that lifts the degeneracy of the energy of the one-dimensional electron subsystem with respect to the orbital degrees of freedom has a commensurate wave vector (quasimomentum), and the instability of the strongly correlated electron chain is determined by the the interaction with this phonon.

However, the ligands surrounding the quasi-one-dimensional electron system are also altered in the crystalline field. As a result, the interaction between the electrons of the chain become substantially anisotropic. Therefore, the energy of the quasi-one-dimensional strongly correlated electrons can be decreased, and the minimum of the total energy of the lattice and the one-dimensional electrons can correspond to a nonzero displacement of the ions of the lattice (its symmetry position) and, consequently, to nonzero anisotropy of the scalar and magnetic interactions of the electrons along the preferred direction. Thus a quasi-one-dimensional chain of strongly correlated electrons turns out to be unstable with respect to the onset of a substantial anisotropy of the electron–electron interaction.

Let us examine the influence of magnetic anisotropy on the stability of quasi-one-dimensional systems of strongly correlated electrons for a specific example, viz., the one-dimensional supersymmetric $t-J$ model, which is one of the most fundamental models of strongly correlated electron systems and has become widely used in recent years, mainly in connection with the problem of high-temperature superconductivity.[8] This model describes the behavior of electrons with an exchange interaction between the spins of electrons on nearest-neighbor sites, and there can be only one electron at any site of the lattice, i.e., at each site of the one-dimensional lattice there are three allowed electronic configurations: an electron with spin projections up and down, and a hole (a state without an electron). It has been shown previously that the one-dimensional isotropic $t-J$ model has a solution at the supersymmetric point (at which the constant for the hopping of electrons between neighboring sites, which is related to the free-electron bandwidth, is equal to one-half of the antiferromagnetic exchange constant between the spins of electrons found on neighboring sites), which was obtained through the use of the Bethe ansatz.[9–11] It has been proved (see, e.g., Ref. 12) that the symmetry of the $t-J$ model is characterized by the presence of four fermion and five boson modes (generalized currents), which correspond to the generators of the corresponding symmetry group $SU(1|2)$. The supersymmetric model explains why the characteristic velocities of these fermionic and bosonic generalized currents are the same at the supersymmetric ($SU(1|2)$) point.[12]

In the present paper we investigate the properties of the one-dimensional supersymmetric $t-J$ model with anisotropy of the magnetic and scalar (charge) interactions between electrons on neighboring sites, the Hamiltonian of which in the fermionic representation has the form[13]

$$\begin{aligned}\mathcal{H}=&\sum_{\sigma,j}\mathcal{P}(c^{+}_{j,\sigma},c_{j+1,\sigma}+c^{+}_{j+1,\sigma},c_{j,\sigma})\mathcal{P}\\&+\sum_{j}(c^{+}_{j,\downarrow}c_{j,\uparrow}c^{+}_{j+1,\uparrow}c_{j+1,\downarrow}+c^{+}_{j,\uparrow}c_{j,\downarrow}c^{+}_{j+1,\downarrow}c_{j+1,\uparrow})\\&-\sum_{j}(\mathrm{e}^{0}n_{j,\uparrow}n_{j+1,\downarrow}+\mathrm{e}^{-\eta}n_{j,\downarrow}n_{j+1,\uparrow})\\&-\frac{1}{2}H\sum_{j}(c^{+}_{j,\uparrow}c_{j,\uparrow}-c^{+}_{j,\downarrow},c_{j,\downarrow})+\frac{1}{2}C\delta^{2},\end{aligned}\tag{1}$$

where $c_{j,\sigma}$ and $c^{+}_{j,\sigma}$ are the Fermi annihilation and creation operators for electrons at site j with spin projection σ: $n_{j,\sigma}=c^{+}_{j,\sigma}c_{j,\sigma}$ is the operator for the number of particles at site j with spin projection σ, $\mathcal{P}=(1-n_{j,-\sigma})(1-n_{j+1,-\sigma})$ is the projection operator, which does not allow the presence of two electrons at the same site; $\eta\equiv x\delta$ is the anisotropy parameter of the electron–electron interaction (we note that in the spin sector it corresponds to inter-ion magnetic anisotropy of the easy axis type, and $\eta=0$ corresponds to an isotropic $SU(1|2)$-symmetric supersymmetric $t-J$ model), x is the electron–lattice interaction constant (we shall assume below that $x=1$); H is the external magnetic field, $(1/2)\,C\delta^2$ is the change in the energy of the elastic subsystem of the ligands (nonmagnetic ions surrounding the one-dimensional chain of electrons) in the lowest approximation in the displacement δ, and C is the elastic constant. Thus the parameter δ determines the distortion of the symmetry configuration of the nonmagnetic ions for a given symmetry of the (three-dimensional) crystal lattice.

With periodic boundary conditions the problem of diagonalizing the Hamiltonian, i.e., of finding its eigenfunctions and eigenvalues, reduces to one of solving the system of Bethe equations[13]

$$\left[\frac{\sin(v_j+i(\eta/2))}{\sin(v_j-i(\eta/2))}\right]^{N_a}=\prod_{\beta a=1}^{M}\frac{\sin(v_j-\Lambda_\alpha+i(\eta/2))}{\sin(v_j-\lambda_\alpha-i(\eta/2))}$$

$$j=1,\ldots,N, \tag{2}$$

$$\prod_{j=1}^{N}\frac{\sin(\Lambda_\alpha-v_j+i(\eta/2))}{\sin(\Lambda_\alpha-v_j-i(\eta/2))}=-\prod_{\beta=1}^{M}\frac{\sin(\Lambda_\alpha-\Lambda_\beta+i\eta)}{\sin(\Lambda_\alpha-\Lambda_\beta-i\eta)},$$

$$\alpha=1,\ldots,M,$$

where M is the number of electrons with spin down, N_a is the number of sites of the (one-dimensional) lattice, N is the total number of electrons in this lattice, v_j, $j=1,\ldots,N$ are the electron (charge) rapidities, and Λ_α, $\alpha=1,\ldots,M$ are the rapidities characterizing the spin degrees of freedom of the electrons in the chain. The rapidities in problems of this kind is the term given to the sets of quantum numbers (parameters) parametrizing the wave functions and eigenvalues of the Hamiltonian (1). The energy of the system is expressed as follows in terms of the rapidities:

$$E=\mu N-\frac{1}{2}H(N-2M)-\sum_{j=1}^{N}\left[\frac{\sin(v_j+i(\eta/2))}{\sin(v_j-i(\eta/2))}\right.$$

$$\left.+\frac{\sin(v_j-i(\eta/2))}{\sin(v_j+i(\eta/2))}\right]+\frac{1}{2}C\delta^2, \tag{3}$$

where μ is a Lagrange multiplier which is equivalent to the chemical potential of the electron subsystem. This multiplier can also take into account the external electrostatic voltage (scalar potential) applied to the system.

The ground state of the one-dimensional system of correlated electrons is characterized by the presence of $N-2M$ unbound electronic excitations (the charge rapidities v_j are real) and $2M$ singlet excitations similar to Cooper pairs (bound states of pairs of electrons with zero total spin; the charge rapidities of such pairs are complex).[13] As follows from the Bethe equations (2), there exists a Λ_β for which the following equation holds up to a factor of $\exp(-N_a)$:

$$v_\alpha^{\pm}=\Lambda_\beta\pm i\frac{\eta}{2}. \tag{4}$$

Then the equation of the Bethe ansatz is rewritten for the charge rapidities v_j characterizing the unbound electron states and for the spin rapidities Λ_α characterizing the states of electrons in singlet pairs. We note that now the charge rapidities characterize the behavior of the quasiparticles carrying spin 1/2, whereas the spin rapidities characterize the behavior of the singlet pairs of electrons, i.e., they have exchanged their functions, as it were. Going over to a description in terms of the rapidities of the pairs, we obtain in place of (2) the following system of equations:

$$\left[\frac{\sin(v_j+i(\eta/2))}{\sin(v_j-i(\eta/2))}\right]^{N_a}=\prod_{\alpha=1}^{M}\frac{\sin(v_j-\Lambda_\alpha+i(\eta/2))}{\sin(v_j-\Lambda_\alpha-i(\eta/2))},$$

$$j=1,\ldots,N-2M,$$

$$\left[\frac{\sin(\Lambda_\alpha+i\eta)}{\sin(\Lambda_\alpha-i\eta)}\right]^{N_a}=-\prod_{j=1}^{N-2M}\frac{\sin(\Lambda_\alpha-v_j+i(\eta/2))}{\sin(\Lambda_\alpha-v_j-i(\eta/2))} \tag{5}$$

$$\times\prod_{\beta=1}^{M}\frac{\sin(\Lambda_\alpha-\Lambda_\beta+i\eta)}{\sin(\Lambda_\alpha-\Lambda_\beta-i\eta)},$$

$$\alpha=1,\ldots,M.$$

The energy is now expressed in terms of the energies of the unbound electrons and singlet pairs:

$$E=\mu N-\sum_{j=1}^{N-2M}\left[\frac{\sin(v_j+i(\eta/2))}{\sin(v_j-i(\eta/2))}+\frac{\sin(v_j-i(\eta/2))}{\sin(v_j+i(\eta/2))}\right]$$

$$-\sum_{\alpha=1}^{M}2\cosh\eta\left(1+\frac{\sin^2\Lambda_\alpha}{\sin^2\Lambda_\alpha+\sinh^2\eta}\right)$$

$$-\frac{1}{2}(N-2M)H+\frac{1}{2}C\delta^2. \tag{6}$$

Taking the logarithm of the system of Bethe equations (5) yields

$$\Theta(v_j,\eta/2)=\frac{1}{N}\sum_{\alpha=1}^{M}\Theta(v_j-\Lambda_\alpha,\eta/2)+\frac{2\pi}{N_a}I_j,$$

$$j=1,\ldots,N-2M,$$

$$\Theta(\Lambda_\alpha,\eta)=\frac{1}{N}\sum_{j=1}^{N-2M}\Theta(\Lambda_\alpha-v_j,\eta/2) \tag{7}$$

$$+\frac{1}{N_a}\sum_{\beta=1}^{M}\Theta(\Lambda_\alpha-\Lambda_{\beta,\eta})+\frac{2\pi}{N_a}J_\alpha,$$

$$\alpha=1,\ldots,M,$$

where $\Theta(v,\eta)=2\tan^{-1}(\tan v\coth\eta)$, and the quantum numbers I_j,J_α parametrizing the solution of the system arise as a result of the multivaluedness of the arguments of the logarithms.

In the thermodynamic limit (in which the numbers of sites, electrons, and electrons with definite spin projection, N_a, N, and M, respectively, go to infinity while the densities N/N_a and M/N_a remain finite) the Bethe equations for the densities of the charge and spin rapidities become

$$\Theta'(v,\eta/2)=\int d\Lambda\,\Theta'(v-\Lambda,\eta/2)\sigma(\Lambda)$$

$$+2\pi[\rho(v)+\rho_h(v)],$$

$$\Theta'(\Lambda,\eta)=\int dv\,\Theta'(\Lambda-v,\eta/2)\rho(v)+\int dz\,\Theta'(\Lambda-z,\eta)\sigma(z)+2\pi[\sigma(\Lambda)+\sigma_h(\Lambda)], \tag{8}$$

where $\rho(v)$ and $\rho_h(v)$ are the distribution functions (densities) of the charge rapidities for ''quasiparticles'' and ''quasiholes,'' respectively, and $\sigma(\Lambda)$ and $\sigma_h(\Lambda)$ are the distribution functions of the spin rapidities; the prime, as usual, denotes a partial derivative. The internal energy of the system in the thermodynamic limit is written

$$\begin{aligned}E=\mu N-\int\rho(v)\left[\frac{\sin(v+i(\eta/2))}{\sin(v-i(\eta/2))}+\frac{\sin(v-i(\eta/2))}{\sin(v+i(\eta/2))}\right]dv\\-2\int\sigma(\Lambda)\cosh\eta\left(1+\frac{\sin^2\Lambda}{\sin^2\Lambda+\sinh^2\eta}\right)d\Lambda\\-\frac{1}{2}(N-2M)H+\frac{1}{2}C\delta^2.\end{aligned} \tag{9}$$

The ground state of the one-dimensional correlated electrons corresponds to eigenstates of the system in which the negative-energy states of the unbound electronic excitations and of the electrons bound into local pairs are all occupied (i.e., the corresponding Fermi seas are filled) and the positive energy states are all empty. We consider the case of zero external magnetic field $(H=0)$. Then the ground state will be made up only of singlet pairs of electrons $(2M=N)$,[13] and the system of Bethe equations will therefore be simplified substantially:

$$\Theta(\Lambda_\alpha,\eta)=\frac{1}{N_a}\sum_{\beta=1}^{M}\Theta(\Lambda_\alpha-\Lambda_{\beta,\eta})+\frac{2\pi}{N_a}J_\alpha,\quad \alpha=1,\dots M, \tag{10}$$

where the J_β are integers (half-integers) for $M+1$ odd (even) and are bounded by $J_{\max}$ (Ref. 14):

$$|J_\alpha|\leqslant\frac{N_a-M-1}{2}=J_{\max}. \tag{11}$$

The ground state corresponds to a set of quantum numbers J_α such that the interval $[-J_{\max},J_{\max}]$ is populated starting from the boundaries of the interval. After taking the thermodynamic limit, we obtain

$$\Theta'(\Lambda,\eta)=\left[\int_{-\pi}^{-\Lambda_0}+\int_{\Lambda_0}^{\pi}\right]dz\,\Theta'(\Lambda-z,\eta)\sigma(z)+2\pi[\sigma(\Lambda)+\sigma_h(\Lambda)]. \tag{12}$$

The quantities Λ_0 have the meaning of the Fermi points (the Fermi surface for a one-dimensional system), since in the ground state only electron states with $\Lambda\in[-\pi,-\Lambda_0]U[\Lambda_0,\pi]$ are observed. We note that, as usual in problems which are exactly solvable with the Bethe ansatz, the wave function of the electron pairs is symmetric (this is natural, since the noninteracting pairs are bosons), but these bosons are impermeable (they have a ''hard core''), and that corresponds to the behavior of a system of fermions. Because of this, the electron pairs have a Fermi sea. We also note that electron pairs interacting with one another in this system are characterized by anyon statistics. The parameter Λ_0 should correspond to the lowest value of the total energy of the electron subsystem:

$$\frac{E}{N_a}=\left[\int_{-\pi}^{-\Lambda_0}+\int_{\Lambda_0}^{\pi}\right]\left[2\mu-2\cosh\eta\times\left(1+\frac{\sin^2\Lambda}{\sin^2\Lambda+\sinh^2\eta}\right)\right]\sigma(\Lambda)d\Lambda+\frac{1}{2}C\delta^2, \tag{13}$$

with

$$\left[\int_{-\pi}^{\Lambda_0}+\int_{\Lambda_0}^{\pi}\right]\sigma(\Lambda)d\Lambda=\frac{M}{N_a}. \tag{14}$$

The ground state energy can be expressed in terms of the so-called ''dressed'' energies of the elementary low-lying excitations (in this case, singlet Cooper pairs):

$$\begin{aligned}E=\int\sigma(\Lambda)\varepsilon_0(\Lambda)d\Lambda\equiv\int\sigma_0(\Lambda)\varepsilon(\Lambda)d\Lambda\\=\frac{N_a}{2\pi}\left[\int_{-\pi}^{-\Lambda_0}+\int_{\Lambda_0}^{\pi}\right]\varepsilon(\Lambda)\Theta'(\Lambda,\eta)d\Lambda+\frac{1}{2}C\delta^2,\end{aligned} \tag{15}$$

where σ_0 is the so-called ''bare'' density of electron pairs, which is determined by the left-hand side of the integral equation (12).

The ''dressed'' energies of the pairs are determined from the integral equation

$$\begin{aligned}\varepsilon(\Lambda)=2\mu-2\cosh\eta\left(1+\frac{\sin^2\Lambda}{\sin^2\Lambda+\sinh^2\eta}\right)\\-\frac{1}{2\pi}\left[\int_{-\pi}^{-\Lambda_0}+\int_{\Lambda_0}^{\pi}\right]\Theta'(\Lambda-z,\eta)\varepsilon(z)dz,\end{aligned} \tag{16}$$

where the first two terms of the right-hand side of the integral equation determine the quantity ε_0 from (15); this is usually called the ''bare'' energy of the excitations, and the interaction, as usual, ''dresses'' it and the density of excitations (the distribution function).[2]

The decrease in energy of the subsystem of one-dimensional correlated electrons due to the influence of the anisotropy of the electron–electron scalar and magnetic interactions is accompanied by an increase in the energy of the elastic (three-dimensional) subsystem. The ground state of the total system (one-dimensional electrons and three-dimensional elastic environment) will correspond to a minimum value of the total energy.

Figure 1 shows the ground state energy of the one-dimensional subsystem of strongly correlated electrons and the elastic subsystem of the ligands (in a three-dimensional crystal lattice) as a function of the filling of the band (N/N_a) and the displacement δ, which determines the magnetic and scalar anisotropy parameter of the electron–electron interaction in the one-dimensional electron subsystem. We see that at all the reduced occupations of the electron band (we are actually talking about the occupation of the Fermi sea of the pairs, since in zero magnetic field there is no Fermi sea of the unbound electronic excitations) there is a minimum of the total energy of the ground state as a function of the distortion of the ligands (in other words, as a function of the anisotropy

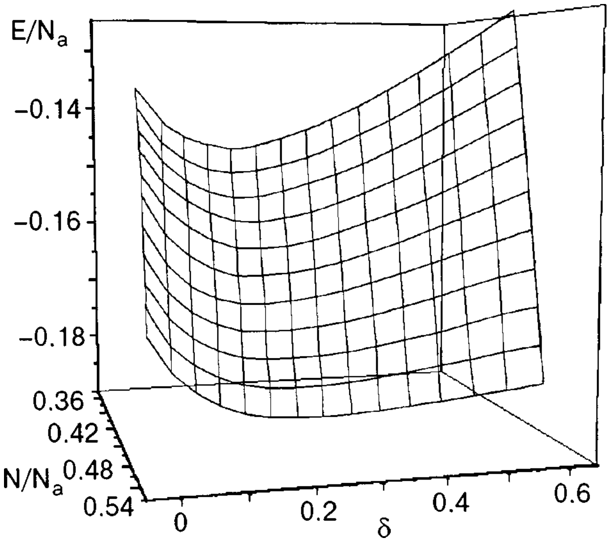

FIG. 1. Total energy E of the ground state of the electron (one-dimensional) and elastic subsystems as a function of the displacement δ of the positions of the ligand ions in the (three-dimensional) crystal lattice and the occupation of the electron band.

parameter of the electron–electron interaction). The value of the parameter δ corresponding to the minimum energy turns out to be nonzero. This means that in the ground state of a one-dimensional system of correlated electrons it is energy favorable for anisotropy of the electron–electron interaction to arise. We note that this anisotropy is manifested in both the magnetic and scalar (charge) interactions of the electrons found at neighboring sites of the one-dimensional lattice.

As an equivalent to the dependence of the energy of the system on the occupation of the band of low-lying electronic excitations, it is convenient to consider the dependence of the effect under discussion on the parameter μ, which can play the role of the chemical potential, or on the voltage (scalar potential) applied to the electron subsystem. Figure 2 shows the ground state energy of the system as a function of the displacement δ of the nonmagnetic ligand lattice for several values of C and μ. We see that at large values of the elastic constant ($C \geqslant 0.48$ for $\mu = 1.2$) the ground state energy of the system has a minimum at a nonzero distortion of the lattice of nonmagnetic ions. The extremal value of δ corresponding to the minimum of the ground state energy of the total system decreases as the elastic constant C increases, and at small C the minimum is not observed (it is shifted to larger values of δ). This is natural, since in order to detect the influence of the anisotropy of the interaction in the electron subsystems (this anisotropy is often very small), it is necessary that the elastic displacements be sufficiently large: after all, the effect is governed by the relativistically small spin–orbit interaction.

Will the stability of the strongly correlated electron subsystem against the onset of anisotropy in the electron–electron interaction be affected by an external magnetic field? Let us consider the system of integral equations (8) for the densities of the distributions of the quantum numbers of singlet pairs and the unbound electronic excitations or of the "dual" to this system, viz., the system of integral equations for the "dressed" energies of these same low-lying excitations of the electron subsystem, which have Fermi seas, i.e., states with negative energies:

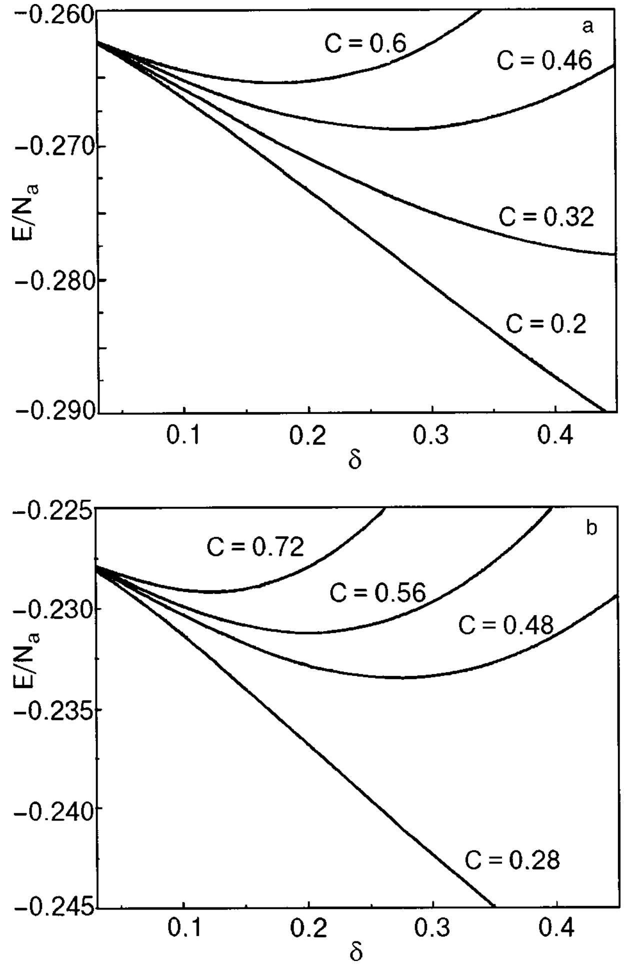

FIG. 2. Total energy E of the ground state of the electron and elastic subsystems as a function of the displacement δ of the position of the ligand ions in the (three-dimensional) crystal lattice. The electron chemical potential $\mu = 1.1$ (a) and 1.2 (b).

$$\mu + \frac{1}{2}H - \Theta'(v, \eta/2) = \frac{1}{2\pi}\int d\Lambda \Theta'(v-\Lambda, \eta/2)\varepsilon(\Lambda) + \epsilon(v),$$

$$2\mu - \Theta'(\Lambda, \eta) = \frac{1}{2\pi}\int dv \Theta'(\Lambda - v, \eta/2)\epsilon(v) + \frac{1}{2\pi}\int dz \Theta'(\Lambda - z, \eta)\varepsilon(z) + \epsilon(\Lambda), \tag{17}$$

where $\epsilon(v)$ is the "dressed" energy of the unbound electronic excitations (we note that the filling of this Fermi sea also starts from the ends of the interval $[-\pi, \pi]$). It is clear that in an external magnetic field H lower than the critical field H_c, which is given by

$$H_c = -2\mu + 2\Theta'(\pi, \eta/2) + \frac{1}{\pi}\int d\Lambda \Theta'(\pi - \Lambda, \eta/2)\varepsilon(\Lambda), \tag{18}$$

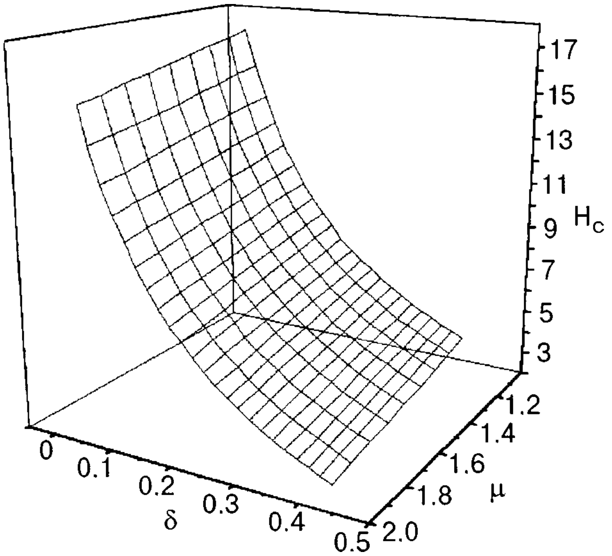

FIG. 3. Dependence of the critical magnetic field H_c on the chemical potential μ and anisotropy parameter δ.

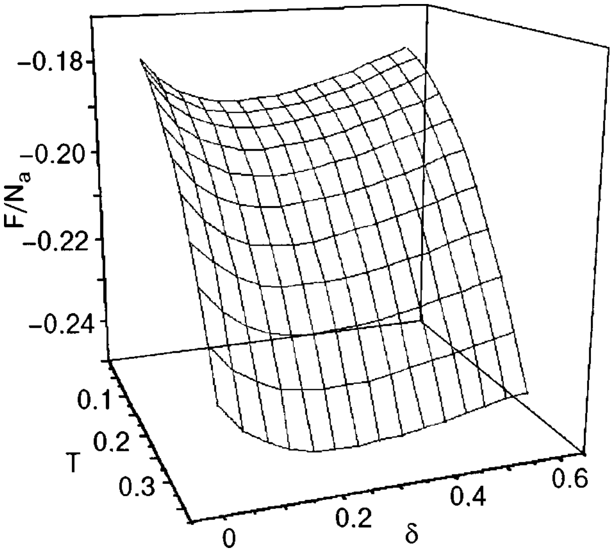

FIG. 4. Total free energy F of the one-dimensional electron and elastic subsystems as a function of the displacement δ of the position of the ligand ions and temperature, at an electron chemical potential $\mu = 1.34$.

the energies of the unbound electronic excitations have a gap in the spectrum (in other words, H_c is the minimum external magnetic field that must be applied to the system in order to ''break'' a singlet pair). This means that at values of the external magnetic field $H \leqslant H_c$ the spontaneous onset of anisotropy of the electron–electron interaction will be the same as in the absence of field. Figure 3 shows the dependence of the critical field H_c on the chemical potential μ and the anisotropy parameter δ of the electron–electron interaction.

If the external magnetic field exceeds a value H_s, which is given by the equation

$$H_s = -2\mu + 2\Theta'(\pi, \eta/2), \tag{19}$$

then the magnetization of the system of electrons will take on its maximum value (the saturation field, the field of the transition to a ferromagnetic, ''spin-polarized'' state in which there are no pairs, while the ''dressed'' energy spectra of the unbound electronic excitations become activational, i.e., a gap appears). At this value of the magnetic field, as at H_c, a second-order phase transition to the ground state occurs in the system. Thus the electron subsystem behaves like a type-II superconductor in an external field: for $H < H_c$ only singlet pairs exist in the system, while for $H_c < H < H_s$ there are both pairs and unbound electronic excitations—reminiscent of the Meissner effect. We note that in a one-dimensional system, of course, there is no real superconducting ordering (nondiagonal long-range order), but in the ground state the correlation functions of the singlet pairs and/or unbound electronic excitations decay most slowly, in a power-law manner, in the first/second phase. We note that for $H > H_s$ one can easily find the ground state energy. It depends (trivially) on the anisotropy parameter δ of the electron–electron interaction: $E = C\delta^2/2$. This means that in external magnetic fields higher than the critical field of the transition to the ''spin-polarized'' phase, there is no spontaneous onset of anisotropy of the electron–electron interaction. In the intermediate phase $H_c < H < H_s$ the ground state energy of the anisotropic supersymmetric $t-J$ chain of electrons is determined by the occupations of the two Fermi seas—for the singlet pairs and for the unbound electronic excitations. The spontaneous onset of anisotropy of the electron–electron interaction does occur, but for a quantitative calculation it is necessary to find a joint solution of the system of two integral equations (17).

One can estimate the influence of a small nonzero temperature on the effect under study (for this we shall assume that the temperature is so low that the elastic subsystem is found in the ground state, i.e., we will not take into account the thermal motion of the three-dimensional lattice). At low temperatures one can use the well-known Sommerfeld expansion (for simplicity we shall study only the case $H < H_c$). Then for the free energy we have the expression

$$F = E - N_a \frac{\pi T^2}{6 v_F}, \tag{20}$$

where v_F is the Fermi velocity of the singlet pairs, which is given by

$$v_F = \left. \frac{\varepsilon'(\Lambda)}{2\pi\sigma(\Lambda)} \right|_{\Lambda = \Lambda_0}, \tag{21}$$

and the ''dressed'' energy and the density of singlet pairs are found from Eqs. (16) and (12), respectively. Figure 4 shows the dependence of the total free energy of the electronic and elastic subsystems on the temperature T and the parameter δ that determines the anisotropy of the electron–electron interaction. We see that the inclusion of a small nonzero temperature (in comparison with the characteristic Fermi energy of the low-lying electronic excitations—pairs) does not cause the effect to vanish, i.e., even at nonzero (but quite low) temperatures an anisotropy of the electron–electron interaction will spontaneously arise in the system. As the temperature is raised, however, the value of δ at the minimum of the energy is shifted to lower values.

CONCLUSION

We have investigated the influence of uniform displacements of the lattice of a three-dimensional crystal in which the motion and interaction of the electrons along one direction are much larger than along the other crystallographic directions. We have shown that distortion alters the crystalline electric fields of the ligands. This, in turn, leads to a change in the influence of the crystalline fields on the orbital moments of the correlated electrons in the selected chain, which gives rise to spontaneous anisotropy of the scalar (charge) electron–electron interaction and (owing to the presence of spin–orbit coupling) to magnetic anisotropy in the presence of an interaction of the electron spins. Thus we have predicted an effect wherein charge and magnetic anisotropy arises spontaneously in one-dimensional chains of strongly correlated electrons in three-dimensional crystals with a quasi-one-dimensional character of the electronic properties. We have investigated the influence of variation of the external magnetic field and also the inclusion of a small (in comparison with the characteristic energies of the one-dimensional electrons) nonzero temperature on the change in occupation of the electron bands (depending on the applied electrostatic voltage). We note that this effect has an interesting feature in comparison with the previously studied onset of spontaneous magnetic anisotropy in a quasi-one-dimensional Heisenberg antiferromagnetic insulator (in which all the electrons are localized). Specifically, a spontaneous magnetic anisotropy of the easy plane type arises in the spin chain, whereas in a strongly correlated electron chain a magnetic anisotropy also arises in addition to the charge anisotropy, but here it is of the easy axis type. The reason for this difference is the existence of Fermi seas for (gapless) singlet pairs in the correlated electron chain, i.e., for purely charge excitations that do not affect the total spin of the system. In a spin chain, on the other hand, where all the electrons are localized, there is no such charge mode, and therefore magnetic anisotropy of the easy axis type leads to the onset of a gap in the spectrum of spin excitations. The existence of such a gap prevents the weak influence of the crystalline field of the ligands from causing instability of the type discussed here. We note that the effect investigated in this paper is similar in nature to the well-known cooperative Jahn–Teller effect.

*E-mail: dmitry@almor.kharkov.ua
**E-mail: zvyagin@mpipks-dresden.mpg.de

---

[1] D. C. Johnston, J. W. Johnston, D. P. Goshorn, and A. P. Jacobson, Phys. Rev. B **35**, 219 (1987); Z. Hiroi, M. Azuma, M. Takano, and Y. Bando, J. Solid State Chem. **95**, 230 (1990); M. Azuma, Z. Hiroi, M. Takano, K. Ishida, and Y. Kitaoka, Phys. Rev. Lett. **73**, 3463 (1994); Y. Ajiro, T. Asano, T. Inami, H. Aruga-Katori, and T. Goto, J. Phys. Soc. Jpn. **63**, 859 (1994); G. Chamboussant, P. A. Crowell, L. P. Levy, O. Piovesana, A. Madouri, and D. Mailly, Phys. Rev. B **55**, 3046 (1997); S. A. Carter, B. Batlogg, R. J. Cava, J. J. Krajewski, W. F. Peck , Jr., and T. M. Rice, Phys. Rev. Lett. **77**, 1378 (1996); G. Chamboussant, Y. Fagot-Revurat, M.-H. Julien, M. E. Hanson, C. Berthier, M. Horvatić, L. P. Levy, and O. Piovesana, Phys. Rev. Lett. **80**, 2713 (1998); W. Shiramura, K. Takatsu, B. Kurniawan, H. Tanaka, H. Uekusa, Y. Ohashi, K. Takizawa, H. Mitamura, and T. Goto, J. Phys. Soc. Jpn. **67**, 1548 (1998).

[2] V. E. Korepin, N. M. Bogoliubov, and A. G. Izergin, *Quantum Inverse Scattering Method and Correlation Functions*, Cambridge University Press, Cambridge (1993).

[3] A. E. Borovik and A. A. Zvyagin, Fiz. Tverd. Tela (Leningrad) **33**, 1587 (1991) [Sov. Phys. Solid State **33**, 894 (1991)].

[4] D. M. Apal'kov and A. A. Zvyagin, Fiz. Nizk. Temp. **24**, 844 (1998) [Low Temp. Phys. **24**, 633 (1998)].

[5] P. Jordan and E. Wigner, Z. Phys. **47**, 631 (1928).

[6] P. Pincus, Solid State Commun. **22**, 1971 (1971); G. Beni and P. Pincus, J. Chem. Phys. **57**, 3531 (1972); A. M. Kosevich and V. I. Khokhlov, Solid State Commun. **11**, 461 (1972); J. Y. Dubois and J. P. Carton, J. Phys. (France) **35**, 371 (1974); Y. Lépine and A. Caillé, J. Chem. Phys. **67**, 5598 (1977); C. Tannous and A. Caillé, Can. J. Phys. **57**, 508 (1979); Y. Lépine and A. Caillé, J. Chem. Phys. **71**, 3728 (1979); Y. Lépine, Phys. Rev. B **24**, 5242 (1981).

[7] M. Hase, I. Terasaki, and K. Uchinokura, Phys. Rev. Lett. **70**, 3651 (1993); M. Isobe and Y. Ueda, J. Phys. Soc. Jpn. **65**, 1178 (1996); M. Isobe and Y. Ueda, Techn. Rept. of ISSP A3253 (1997).

[8] F. C. Zhang and T. M. Rice, Phys. Rev. B **37**, 3759 (1988).

[9] C. K. Lai, J. Math. Phys. **15**, 167 (1974).

[10] P. Shlottmann, Phys. Rev. B **36**, 5177 (1987).

[11] B. Sutherland, Phys. Rev. B **12**, 3795 (1975).

[12] F. H. L. Essler and V. E. Korepin, Phys. Rev. B **46**, 9147 (1992).

[13] R. Z. Bariev, Phys. Rev. B **49**, 1474 (1994).

[14] P.-A. Bares, G. Blatter, and M. Ogata, Phys. Rev. B **44**, 130 (1991).

Translated by Steve Torstveit

LATTICE DYNAMICS

Thermodynamics of an atomic monolayer with diatomic substitutional impurities

M. I. Poltavskaya and K. A. Chishko*

B. I. Verkin Physicotechnical Institute for Low Temperature Physics, National Academy of Sciences of Ukraine, Lenin prospect, 47, 61164 Kharkov, Ukraine

(Submitted October 22, 1999)
Fiz. Nizk. Temp. **26**, 394–403 (April 2000)

The low-temperature thermodynamics of a two-dimensional monatomic crystalline matrix containing a diatomic molecular impurity is investigated theoretically. Typical examples of this type of system are monatomic layers of rare gases (Ne, Ar, Kr, Xe) with included molecules of the type N_2 and O_2. Another example is a hydrogen film, which is a mixture of ortho and para components. Expressions are obtained which describe the crystalline field for a diatomic impurity with allowance for both the contribution of the atoms of the 2D matrix and the field created by the atoms of the substrate. Thus the effective crystalline field is a complicated function of the orientation of the diatomic rotator. In particular, the equilibrium orientation of the rotator depends substantially on the relative amplitudes of the crystalline fields of the matrix and substrate. For example, if the attraction exerted by the substrate is dominant, then the rotator in the equilibrium state will be oriented perpendicular to the layer, and in the opposite case the equilibrium orientation of the rotator will correspond to one of its positions in the plane of the layer. In these two cases the spectra of rotational states of the diatomic impurities and, hence, the thermodynamic characteristics of the system are substantially different. The temperature dependence of the impurity specific heat of the system exhibits a low-temperature peak, the position of which corresponds to temperatures $T \sim B/2$ (B is the rotational constant of the impurity) for rotators lying in the plane of the layer, and $T \sim \sqrt{KB}$ (K is the amplitude of the crystalline field) for rotators perpendicular to the layer. Such behavior of the system is in principle amenable to experimental observation. [S1063-777X(00)01104-X]

1. INTRODUCTION

Research on molecular cryocrystals and solid solutions based on them is an extremely vast area of present-day solid-state physics. These systems are of interest first because their properties are in most cases reflect manifestations of various quantum effects which are not amenable to observation in classical crystals at high temperatures. In particular, the thermodynamics of molecular cryocrystals (solidified rare gases, O_2, N_2, CH_4, etc. and their solutions) are entirely determined by the character of the short-range van der Waals forces of intermolecular coupling. Thus analysis of the features in the thermodynamic functions of these systems will make it possible to draw definite conclusions as to the nature of the intermolecular interaction in them.

The thermodynamic properties of three-dimensional cryocrystals are at present the most thoroughly investigated.[1,2] The thermodynamics of two-dimensional (2D) systems of this kind remain little studied as yet. The reason for this lies in the difficulties of doing suitable experiments on 2D samples. What has been well studied for 2D crystals are the structural characteristics, the phase diagrams, and certain details of the melting and crystallization processes.[3–6] In the last few years some new experimental capabilities for studying 2D films at ultralow temperatures have appeared, but they have been applied almost exclusively to ^{3}He layers on graphite[7–11] and to combined systems consisting of several layers of hydrogen and helium.[12] The study of the thermodynamics of two-dimensional layers based on other rare gases (in particular, in the presence of molecular impurities in them) is clearly of interest also.

In this paper we wish to call attention to certain interesting features in the low-temperature specific heat of 2D monatomic matrices containing diatomic impurities. We obtain expressions describing the crystalline field for a diatomic impurity with allowance for both the contribution of the atoms of the 2D matrix and the field produced by atoms of the substrate. The effective crystalline field is a complicated function of the orientation of the diatomic rotator. We calculate the spectra of rotational states of diatomic impurities and find the specific heat of the system for various relationships between the contributions of the substrate and matrix to the total crystalline potential that determines the spectrum of impurity excitations.

2. CRYSTALLINE POTENTIAL FOR A DIATOMIC IMPURITY IN A MONATOMIC LAYER

Let us consider a monatomic layer of rare gas atoms with molecules of a homonuclear diatomic substitutional impurity (symmetric rotator). The atoms in the layer form a close-packed planar structure in which each atom of the matrix is surrounded by six neighbors, located a distance a from one another. We restrict discussion to the case of rather weak solutions, when the impurities in the layer are surrounded only by host atoms of the matrix and the inter-impurity interaction can be neglected. Here, however, it is necessary to take into account the interaction of the impurity with the substrate, which we take to be a close-packed system of atoms also lying a distance a apart, but the potential energy of their interaction with the impurity is different from that for the interaction of the impurity with the atoms of the matrix. The distance between layer and substrate we take to be $c/2=\beta a$, where the parameter β is equal to $\sqrt{2/3}$ in the case of an ideal hcp structure, but here we will not impose any special limitations on β. We choose the coordinate system in such a way that the layer of rare gas atoms lies in the $z=0$ plane, and the rotator lies at the origin of the coordinate system. In this case the nearest neighbor of the diatomic rotator has the coordinates $\pm a(1,0,0)$, $\pm a(\pm(1/2),(\sqrt{3}/2,0)$ (neighbors in the layer) and $a(\pm(1/2),(1/2\sqrt{3}),-\beta)$, $a(0,-(1/\sqrt{3}),-\beta)$ (neighbors in the substrate). We note that the z axis is a threefold symmetry axis in the system.

The scheme of the calculation must include a determination of the crystalline potential for a substitutional impurity and a solution of the Schrödinger equation with this potential for finding the spectrum of rotational states of the defect. The total crystalline field produced by the atoms surrounding an impurity is written in the form

$$U(\mathbf{r})=\sum_{\alpha=1,2} U_\alpha, \tag{1}$$

where U_1 is the field of the neighboring atoms in the layer, and U_2 is the field of the substrate atoms. In what follows we shall use the subscripts 1 and 2 to denote quantities pertaining to the atoms of the layer and substrate, respectively.

Since our analysis pertains to molecular systems, we limit consideration to power-law potentials (specifically, the Lennard-Jones potential). This restriction is not of fundamental importance, and the calculations below could also be done for exponential potentials of the Buckingham type. In the nearest-neighbor approximation the crystalline potential for an impurity can be obtained by expanding the sum of the atom–atom potentials of the environment in powers of the parameter $\xi=r/a$, where $\mathbf{r}$ is the radius vector of an atom of the matrix (or of the substrate), drawn from the site at which the impurity is located,

$$U_\alpha=4\varepsilon_\alpha[\sigma_\alpha^{12}u_{12}^{(\alpha)}(r)-\sigma_\alpha^6u_6^{(\alpha)}(r)],$$

where ε_α and σ_α are the parameters of the Lennard-Jones potential,[13] and the $u_{2\nu}^{(\alpha)}(r)$ $(2\nu=6,12)$ have the form

$$u_{2\nu}^{(\alpha)}(r)=\sum_{i=1}^{z_\alpha}|\mathbf{r}-\mathbf{R}_i|^{-2\nu}=\sum_{i=1}^{z_\alpha}R_i^{-2\nu}(1+\xi_i^2-2\xi_i\cos\chi_i)^{-\nu}, \tag{2}$$

z_1 and z_2 are the numbers of neighbors in the layer and substrate, respectively, the summation in (2) is over the coordinates $\mathbf{R}_i$ of the neighbors, χ_i is the angle between the radius vectors $\mathbf{r}$ and $\mathbf{R}_i$. Expression (2) can be transformed to[14]

$$(1+\xi_i^2-2\xi_i\cos\chi_i)^{-\nu}=\sum_{m=0}^{\infty}F_m^{(\nu)}(\xi_i)\cos^m(\chi_i), \tag{3}$$

where

$$F_m^{(\nu)}(\xi)=\frac{(2\xi)^m(\nu+m-1)!}{m!(\nu-1)!(1+\xi^2)^{\nu+m}}.$$

A calculation of the function $F_m^{(\nu)}(\xi)$ is given in the Appendix.

Using expressions (1) and (3) and doing the summation over impurity atoms, we obtain the crystalline potential for a homonuclear diatomic impurity, in a spherical coordinate system in which the angle θ is measured from the axis perpendicular to the layer and the angle φ from the center of one of the atoms of the layer:

$$U=\frac{1}{a^2\nu}\sum_{m=0}^{\infty}F_m^{(\nu)}(\xi_1)\Phi_m^{(1)}(\theta,\varphi)+\left(\frac{b}{a}\right)^{(2\nu)}\sum_{m=0}^{\infty}F_m^{(\nu)}(\xi_2)\Phi_m^{(2)}(\theta,\varphi), \tag{4}$$

where

$$\xi_1=d/a,\quad \xi_2=bd/a,\quad b=(1/3+\beta^2)^{-1/2};$$

$2d$ is the internuclear distance in the molecule, and

$$\Phi_m^{(\alpha)}(\theta,\varphi)=\sum_{i=1}^{z_\alpha}\cos^m(\chi_i).$$

Let us write out the first few functions $\Phi_m^{(1)}$, $\Phi_m^{(2)}$:

$$\Phi_0^{(1)}=6;\quad \Phi_2^{(1)}=3\sin^2\theta;\quad \Phi_4^{(1)}=\frac{9}{4}\sin^4\theta;$$

$$\Phi_6^{(1)}=\frac{3}{16}[10+\cos 6\varphi]\sin^4\theta.$$

All the functions $\Phi_m^{(1)}$ with odd m are equal to zero. Continuing, we have

$$\Phi_0^{(2)}=3;\quad \Phi_1^{(2)}=-3b\beta\cos\theta;$$

$$\Phi_2^{(2)}=b^2\left[3\beta^2\cos^2\theta+\frac{1}{2}\sin^2\theta\right];$$

$$\Phi_3^{(2)}=-3b^3\left[\beta^3\cos^3\theta+\frac{1}{2}\beta\cos\theta\sin^2\theta-\frac{1}{12\sqrt{3}}\sin^3\theta\sin 3\varphi\right];$$

$$\Phi_4^{(2)}=b^4\left[3\beta^4\cos^4\theta+3\beta^2\sin^2\theta\cos^2\theta-\frac{\beta}{\sqrt{3}}\cos\theta\sin^3\theta\sin\beta\varphi+\frac{1}{8}\sin^4\theta\right];$$

$$\Phi_5^{(2)}=-5b^5\Bigg[\frac{3}{5}\beta^5\cos^5\theta+\beta^3\cos^3\theta\sin^2\theta-\frac{1}{2\sqrt{3}}\beta^2\cos^2\theta\sin^3\theta\sin 3\varphi+\frac{1}{8}\beta\cos\theta\sin^4\theta-\frac{1}{48\sqrt{3}}\sin^5\theta\sin 3\varphi\Bigg];$$

$$\Phi_6^{(2)}=b^6\Bigg[3\beta^6\cos^6\theta+\frac{15}{2}\beta^4\cos^4\theta\sin^2\theta-\frac{5}{\sqrt{3}}\beta^3\cos^3\theta\sin^3\theta\sin 3\varphi+\frac{15}{8}\beta^2\cos^2\theta\sin^4\theta-\frac{5}{8\sqrt{3}}\beta\sin^5\theta\cos\theta\sin 3\varphi+\sin^6\theta\left(\frac{1}{144}\sin^2 3\varphi+\frac{1}{32}\right)\Bigg].$$

Up to terms of order $(d/a)^6$ the desired potential has the form

$$\begin{aligned}U(\theta,\varphi)=\;&\mathcal{K}_1\sin^2\theta+\mathcal{K}_2\sin^2\theta(1+v_1\sin^2\theta\\&+v_2\sin\theta\cos\theta\sin 3\varphi)\\&+\mathcal{K}_3\sin^2\theta[1+v_3\sin^2\theta+(w_1\\&+w_2\sin^2\theta)\sin\theta\cos\theta\sin 3\varphi)\\&+(w_3\cos 6\varphi+w_4)\sin^4\theta].\end{aligned}\tag{5}$$

Here we have introduced the following notation:

$$\mathcal{K}_1=6V_2^{(1)}-b^2(6\beta^2-1)V_2^{(2)};$$

$$\mathcal{K}_2=-6b^4(2\beta^4-\beta^2)V_4^{(2)};$$

$$\mathcal{K}_3=-6b^6\left(3\beta^6-\frac{5}{2}\beta^4\right)V_6^{(2)};$$

$$v_1=\frac{1}{\mathcal{K}_2}\left[\frac{9}{2}V_4^{(1)}+b^4\left(6\beta^4-6\beta^2+\frac{1}{4}\right)V_4^{(2)}\right];$$

$$v_2=-\frac{2b^4\beta}{\sqrt{2}\mathcal{K}_2}V_4^{(2)};$$

$$v_3=\frac{6b^6}{\mathcal{K}_3}\left(3\beta^6-5\beta^4+\frac{5}{8}\beta^2\right)V_6^{(2)};$$

$$w_1=-\frac{10b^6\beta^3}{\sqrt{3}\mathcal{K}_3}V_6^{(2)};$$

$$w_2=\frac{5b^6}{\sqrt{3}\mathcal{K}_3}(2\beta^3-\beta/4)V_6^{(2)};$$

$$w_3=\frac{1}{\mathcal{K}_3}\left(\frac{3}{8}V_6^{(1)}-\frac{b^6}{144}V_6^{(2)}\right);$$

$$w_4=\frac{1}{\mathcal{K}_3}\left[\frac{15}{4}V_6^{(1)}-b^6\left(6\beta^6-15\beta^4+\frac{15}{4}\beta^2-\frac{5}{72}\right)V_6^{(2)}\right],$$

where

$$V_i^{(1)}=4\varepsilon_1\left[\left(\frac{\sigma_1}{a}\right)^{12}F_i^{(6)}(\xi_1)-\left(\frac{\sigma_1}{a}\right)^6F_i^{(3)}(\xi_1)\right];\tag{6}$$

$$V_i^{(2)}=4\varepsilon_2\left[\left(\frac{\sigma_2 b}{a}\right)^{12}F_i^{(6)}(\xi_2)-\left(\frac{\sigma_2 b}{a}\right)^6F_i^{(3)}(\xi_2)\right],\tag{7}$$

and the index i is the order of the corresponding term in the expansion in powers of d/a.

Expression (5) is an expansion of the crystalline potential in powers of the parameter d/a. The first term in (5) is of order $(d/a)^2$ and gives the main contribution to the potential; the second and third terms are of order $(d/a)^4$ and $(d/a)^6$, respectively. The absence of odd-power terms in the expansion is due to the fact that we are considering only homonuclear impurities, for which the crystalline field has a center of inversion and, consequently, an interchange of the atoms in the molecular rotator (replacing d by $-d$) must not alter the form of the expression for the potential. Dependence on the angle φ arises in the second and third terms in (5); the terms containing $\sin 3\varphi$ are due to the influence of the substrate, while the presence of terms containing $\cos 6\varphi$ is due to both the substrate and the contribution of neighbors in the layer. We note that in writing the potential for an impurity in a three-dimensional crystal,[14] where there are identical atoms situated symmetrically in the upper and lower layers, the terms of fourth and sixth orders of smallness, which are proportional to $\sin 3\varphi$, vanish, and dependence on φ remains only in the sixth-order term, which contains a cofactor $\cos 6\varphi$.

The signs of the individual terms in the potential (5) are determined by the relative modulus and sign of the parameters (6) and (7) in terms of which the coefficients $\mathcal{K}$, v, and w are expressed. The parameters (6) and (7) depend in a complicated way on both the parameters σ and ε of the Lennard-Jones potential and on the lattice parameters a and β. These last, in turn, depend on the distribution of the potential minima on the substrate, so that ultimately their values can differ appreciably from those for a massive crystal. Thus the amplitude and sign of the crystalline fields in which the diatomic rotator moves can be different depending on the particular structure of the system.

Finally, we make note of the fact that the potential in this Section has been written out to terms of order $(d/a)^6$. This was done for a reason. Even though our main task in the next Section will be to calculate the rotational spectrum of the impurity to leading order in d/a, the terms $\propto(d/a)^6$ in the potential (5) will be needed for making estimates pertaining to the two-dimensional plane rotator regime (see Sec. 3). In addition, the given representation will enable us to illustrate all the symmetry-related features of the potential structure.

3. SPECTRUM OF ROTATIONAL STATES OF AN IMPURITY MOLECULE

The rotational states of an impurity molecule are found as the solutions of the Schrödinger equation with the potential (5):

$$\left[-\Delta_{\theta,\varphi}+\frac{1}{B}U(\theta,\varphi)\right]\psi_{lm}(\theta,\varphi)=\varepsilon_{lm}\psi_{lm}(\theta,\varphi), \tag{8}$$

where $\Delta_{\theta,\varphi}$ is the angular part of the Laplacian operator, $B=\hbar^2/2I$ is the rotational constant, I is the moment of inertia of the molecule, $\varepsilon_{lm}=E_{lm}/B$, E_{lm} is the energy of the rotational state, which is classified by the quantum numbers l and m (in the case of a free rotator these numbers correspond to the values of the square and z projection of the total angular momentum of the impurity molecule). Since the potential (5) has a rather complicated form, a solution of equation (8) can be obtained in the general case only by numerical methods.

Let us begin by discussing the construction of certain approximate solutions which will enable us to describe the properties of the system of interest analytically and to elucidate its main behavioral features. We will thereby get a qualitative physical picture of the phenomenon, the details of which can be filled in later as necessary.

For constructing approximate solutions of Eq. (8) it is natural to limit the number of terms in the crystalline potential (5). As the main approximation let us consider the solution obtained with the first term of potential (5):

$$\mathcal{U}(\theta)=K\sin^2\theta, \tag{9}$$

where $K\simeq\mathcal{K}_1$ is the crystalline-field constant. In accordance with the remarks made at the end of the previous Section, we cannot draw any preliminary conclusions as to the sign of K from general arguments. For this reason we need to consider both cases $K>0$ and $K<0$. It is perfectly obvious that these cases correspond to two physically different situations. For $K>0$ the rotator in its equilibrium position is oriented perpendicular to the layer. In this case the weakly excited states of the impurity are oscillations in an isotropic two-dimensional parabolic well (librational motion). For $K<0$ the impurity in its equilibrium position lies in the plane of the layer, and its behavior at low temperatures should be analogous to the motion of a plane rotator whose angular momentum precesses around the z axis. Thus we can expect that the thermodynamic characteristics of the impurity subsystem in the low-temperature limit will be substantially different in the two cases.

However, there is an important circumstance that must be considered. Whereas in the case $K>0$ (oscillator) the properties of the system are determined solely by the character of the dependence of the potential on the angle θ, while the dependence on the angle φ is unimportant, in the case $K<0$ (plane rotator) the situation is extremely nontrivial and requires a special allowance for the dependence of the potential on φ. The problems arising in this connection will be discussed separately at the end of this Section.

Thus we shall solve the Schrödinger equation

$$\left[-\Delta_{\theta,\varphi}+\frac{K}{B}\sin^2\theta\right]\Psi_{lm}(\theta,\varphi)=\varepsilon_{lm}\Psi_{lm}(\theta,\varphi). \tag{10}$$

Since the potential in Eq. (10) does not depend on φ, we shall seek the solution in the form

$$\Psi_{lm}=\Psi_{lm}(\theta)e^{im\varphi},$$

where m is a quantum number having the usual meaning of the projection of the angular momentum on the z axis. The function $\Psi_{lm}(\theta)$ satisfies the equation

$$-\frac{d}{dx}(1-x^2)\frac{d\Psi_{lm}}{dx}+\frac{m^2}{1-x^2}\times\Psi_{lm}\pm p^2(1-x^2)\Psi_{lm}=\varepsilon_{lm}\Psi_{lm}, \tag{11}$$

where $x=\cos\theta$, $p=\sqrt{|K|/B}$, and the sign in front of p^2 in (11) is the same as the sign of K. The eigenfunctions of equation (11) with the plus or minus sign are oblate or prolate spheroidal harmonics, respectively.[15,16] Since the potential (9) is an even function, the solutions of equation (11) are classified according to parity, i.e., even and odd states correspond to even and odd values of the parameter $l-m$.[15] The ground state ε_{00} is nondegenerate, as are all states with $m=0$, while all the remaining states with $l\geqslant 1$ are twofold degenerate ($m\leqslant l$).

In the general case the solutions of equation (11) are represented in the form of expansions in associated Legendre polynomials.[15] In many physically interesting cases, however, the properties of the systems are such that the rotational constant B of the impurity is rather small and the crystalline field is appreciable, so that the parameter $|K|/B\gg 1$ (as an example we cite solutions of the type Ar–N_2, for which a typical value is $K/B\sim 20$).[2] In such a case the spectrum can be obtained analytically with the use of asymptotic methods.[15] Since, as we shall see, the corresponding asymptotic expressions provide a rather accurate reflection of the position of the lowest levels in the system, there is reason to assume that they can be used to obtain an entirely adequate description of the thermodynamics of the impurity subsystem at low temperatures. For this reason we shall restrict our investigation in this paper to systems for which $p^2\gg 1$.

The subsequent analysis must be done separately for the cases of positive and negative values of the crystalline-field constant K.

Let us start with the case $K>0$, for which we use the known asymptotic representation of the spectrum:[15]

$$\varepsilon_{lm}=2ps-\frac{1}{2}(s^2+1-m^2), \tag{12}$$

where $s=2n+m+1$, and

$$n=\begin{cases}(l-m)/2 & l-m\ \text{even},\\ (l-m-1)/2 & l-m\ \text{odd}.\end{cases} \tag{13}$$

In writing Eq. (12) we have kept only the two leading terms of the expansion, dropping terms $\sim 1/p$ and higher. In addition, we have neglected the exponentially small terms $[\sim p^{2+1}\exp(-2p)]$ of the asymptotic series. It should be stressed that the expansion parameter here is actually the ratio s/p (Refs. 15 and 16), so that representation (12) is valid, essentially, for the low-lying levels with $l\leqslant 3$. Since we are interested primarily in the low-temperature behavior of the system, only these levels will be taken into account below. In the analysis below the classification of states according to parity will also be important, since, depending on the isotopic modification, the impurity molecule can have even or odd total spin, and this, in turn, will affect the form of the partition function of the system.[17] An example of the different thermodynamic behavior of cryosolutions for different isotopes of an impurity is provided by the systems $^{14}N_2$–Ar(Kr) and $^{15}N_2$–Ar(Kr).[18] Thus we separate the systems of even levels

$$\varepsilon_{00}^{g}=2p-1;\quad \varepsilon_{11}^{g}=4p-2,$$
$$\varepsilon_{20}^{g}=6p-5;\quad \varepsilon_{22}^{g}=6p-3 \tag{14}$$

and odd levels

$$\varepsilon_{10}^{u}=2p-1;\quad \varepsilon_{21}^{u}=4p-2,$$
$$\varepsilon_{30}^{u}=6p-5;\quad \varepsilon_{32}^{u}=6p-3 \tag{15}$$

which have different relative values of the degeneracy g_g and g_u. As we see from Eq. (12), for $p\to\infty$ the impurity will behave as a harmonic oscillator, as we have said.

In the case $K<0$ the asymptotic spectrum (here we again drop terms of order $1/p$ and higher) has the form[15]

$$\varepsilon_{lm}=-p^2+p-\frac{3}{4}+\left(2p-\frac{1}{2}\right)(l-m)-\frac{1}{2}(l-m)^2+m^2. \tag{16}$$

Here the small parameter of the expansion is actually the ratio $[2(l-m)+1]/p$, so that in this case the analysis is restricted to levels with $l\leqslant 3$. Thus we have the even levels

$$\varepsilon_{00}^{g}=-p^2+p-3/4;\quad \varepsilon_{11}^{g}=-p^2+p+1/4;$$
$$\varepsilon_{22}^{g}=-p^2+p+13/4 \tag{17}$$

and odd levels

$$\varepsilon_{10}^{u}=-p^2+3p-7/4;\quad \varepsilon_{21}^{u}=-p^2+3p-3/4. \tag{18}$$

As expected, for $p\to\infty$ the spectrum (16) agrees, to within a constant, with the spectrum of the free plane rotator.[19]

Notice that the case $K<0$ requires the more-detailed analysis. This case corresponds to the motion of the rotator about the equatorial plane $\theta=\pi/2$ through the potential relief formed by terms and cofactors that depend on θ (these form the ‘‘groove’’ in which the ‘‘dumbbell,’’ rotating with respect to φ, executes librations with respect to θ). On the other hand, in its displacement along the ‘‘groove’’ the impurity moves in a field that depends on φ. This dependence is determined by the terms which were previously dropped from the expansion of the potential (5). These terms can turn out to be important in the case when they give rise to levels in the system that fall within the energy interval corresponding to the lower levels for the motion with respect to θ [see Eqs. (16)–(18)] and thereby (together with the spectrum (16) given above) determine the low-temperature thermodynamics of the system.

Let us now give a few estimates relevant to the analysis of the situation. We shall assume that the motion occurs in a narrow enough interval of angles $\theta=\pi/2+\gamma$ $(\gamma\ll 1)$ that one can use only the terms of zero order in γ for its description. Thus the motion is governed by the Schrödinger equation

$$\left[-\frac{\partial^2}{\partial\gamma^2}-\frac{\partial^2}{\partial\varphi^2}+\sigma_0\cos 6\varphi\right]\Psi(\gamma,\varphi)=\varepsilon\Psi(\gamma,\varphi), \tag{19}$$

in which

$$\sigma_0=\mathcal{K}_3 w_3/B, \tag{20}$$

and the potential depends only on the single variable φ. Here the variable γ formally belongs to the interval $[-\pi/2;\pi/2]$. The variables in Eq. (19) separate; after the γ-dependent part is separated off in the obvious way, we obtain a Mathieu equation for determining the motion along φ:

$$-\frac{\partial^2\Psi(\varphi)}{\partial\varphi^2}+(n^2-\varepsilon+\sigma_0\cos 6\varphi)\psi(\varphi)=0,$$

where n is a separation constant $(n=0,1,\ldots)$. The first five levels have the values

$$(\varepsilon_0^{g}-n^2)/9=-q^2/2;(\varepsilon_1^{g}-n^2)/9=1+q-q^2/8;$$
$$(\varepsilon_2^{g}-n^2)/9=4+5q^2/12 \tag{21}$$

(even levels) and

$$(\varepsilon_1^{u}-n^2)/9=1-q-q^2/8;$$
$$(\varepsilon_2^{u}-n^2)/9=4-q^2/12 \tag{22}$$

(odd levels), where $q=\sigma_0/18$. All the levels with $n\neq 0$ are twofold degenerate.

We call attention to the fact that $q\ll 1$, as numerical estimates for specific systems show (e.g., for an N_2 impurity in argon one has $q\sim 10^{-3}$). Thus the terms in (21) and (22) that depend on q can be omitted for making estimates. With this accuracy we obtain a spectrum in which the lowest-lying levels have the form $\varepsilon\sim n^2$. This result is due specifically to the bounded motion with respect to the angle θ and agrees with (17) and (18) to good enough accuracy. For this reason it is clear that for $K<0$ the position of the lowest levels in the spectrum and, hence, the low-temperature thermodynamics will be determined primarily by the dependence of the potential on the variable θ. This, in particular, means that, to the asymptotic accuracy adopted here, we can use the spectrum described by expressions (17) and (18).

4. SPECIFIC HEAT OF THE IMPURITY SUBSYSTEM

The partition function and thermodynamic potentials of the system can be obtained in the standard way with the use of the excitation spectra given in the previous Section. The partition function of a diatomic impurity can be written[17]

$$Z=g_gZ_g+g_uZ_u, \tag{23}$$

where Z_g and Z_u are the contributions of the even and odd states, respectively. Since we are primarily interested here in a qualitative picture of the phenomena, we limit discussion to the case when the spin of the nuclei of the rotator is equal to unity. In this case $g_g=2/3$ and $g_u=1/3$.

The internal energy of the impurity subsystem per molecule is given by

$$E=T^2\frac{\partial\ln Z}{\partial T}.$$

Accordingly, the impurity specific heat per molecule is

$$C_v=\left(\frac{\partial E}{\partial T}\right)_v.$$

Let us first discuss the analytical asymptotic expressions. For the case $K>0$ we get

$$C_v=\Theta^{-2}\left[2(2p-1)^2\exp\left(-\frac{2p-1}{\Theta}\right)+(4p-4)^2\exp\left(-\frac{4p-4}{\Theta}\right)\right], \tag{24}$$

where $\Theta=T/B$ is the dimensionless temperature. Formula (24) represents the first two terms in the expansion of the specific heat in powers of the small parameter $\exp(-2p/\Theta)\ll 1$. In the case $K<0$ the specific heat has the form

$$C_v=\tilde{Z}^{-1}\Theta^{-2}\left\{2g_g\left[\exp\left(-\frac{1}{\Theta}\right)+16\exp\left(-\frac{4}{\Theta}\right)\right]+g_u\left[(2p-1)^2\exp\left(-\frac{2p-1}{\Theta}\right)+8p^2\exp\left(-\frac{2p}{\Theta}\right)\right]\right\}-\left(\frac{E}{B\Theta}\right)^2, \tag{25}$$

where

$$\tilde{Z}=g_g\left\{1+2\left[\exp\left(-\frac{1}{\Theta}\right)+\exp\left(-\frac{4}{\Theta}\right)\right]\right\}+g_u\left[\exp\left(-\frac{2p-1}{\Theta}\right)+2\exp\left(-\frac{2p}{\Theta}\right)\right];$$

$$\frac{E}{B}=\tilde{Z}^{-1}\left\{2g_g\left[\exp\left(-\frac{1}{\Theta}\right)+4\exp\left(-\frac{4}{\Theta}\right)\right]+g_u\left[(2p-1)\exp\left(-\frac{2p-1}{\Theta}\right)+4p\exp\left(-\frac{2p}{\Theta}\right)\right]\right\}.$$

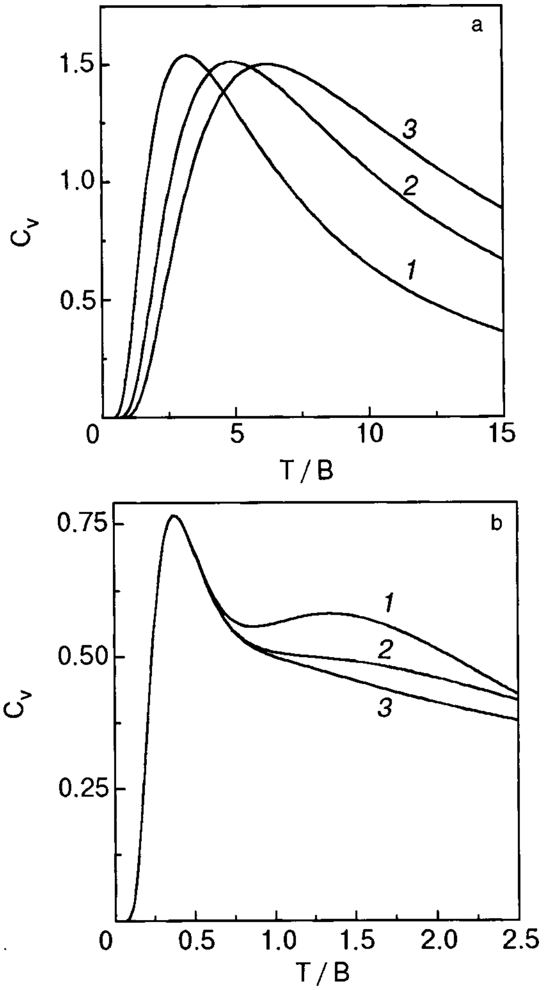

FIG. 1. Temperature dependence of the impurity specific heat for the cases $K>0$ (a) and $K<0$ (b) for various values of the crystalline-field amplitude p^2: 10 (*1*), 20 (*2*), and 30 (*3*). The dimensionless specific heat is expressed per impurity molecule.

Figure 1a shows the temperature dependence of the impurity specific heat for the case $K>0$ (librational regime) for three values of the crystalline-field amplitude, $p^2=10$, 20, 30. The maximum of the specific heat is found at a temperature $T\sim B(\sqrt{K/B}-1/2)$. As the intensity of the crystalline field is increased (with increasing K) the maximum of the specific heat is shifted to higher temperatures and decreases slightly in amplitude. As $T\rightarrow\infty$ the purely oscillator specific heat should approach the equipartition law ($C_v\rightarrow 2$), but at high temperatures the distribution from the second term in (12) comes into play, and the specific heat curve turns downward, approaching the dependence it would have in the case of a hindered three-dimensional rotator (the energy becomes comparable to the well depth). However, since we are interested in the low-temperature features of the specific heat, we shall not discuss the high-temperature part of the calculated function.

Figure 1b shows the temperature dependence of the impurity specific heat for the case $K<0$ (hindered plane rotator), which has a pronounced low-temperature peak at $T\sim B/2$, the position of which does not depend on the amplitude of the crystalline field. We should point out that the calculation, which is based on taking only the lowest several levels into account, is valid for temperatures that are not too high. Nevertheless, in the region of greatest interest to us, i.e., around the low-temperature peak of the specific heat, the results obtained with the use of the analytical asymptotic expressions give a qualitatively correct physical picture of the phenomenon under discussion.

The foregoing analysis shows that the subsystem of diatomic molecular rotators in a two-dimensional monatomic cryomatrix exhibits pronounced anomalies of the specific heat in the low-temperature region. The position of the low-temperature peak of the specific heat and the dependence of this peak on the value of the crystalline-field constant are different for different relationships between the interaction parameters of the impurity with the substrate and with host atoms of the film. Thus one expects that the experimental observation and study of the effects described above can yield useful information about the details of this interaction.

APPENDIX 1

The expression $(1+\xi^2-2\xi\cos\chi)^{-\nu}$ is the generating function for the ultraspherical polynomials [the Gegenbauer polynomials $C_n^{(\nu)}(x)$]:[16]

$$(1+\xi^2-2\xi\cos\chi)^{-\nu}=\sum_{n=0}^{\infty}C_n^{(\nu)}(\cos\chi)\xi^n, \tag{A1}$$

where

$$C_n^{(\nu)}(x)=\frac{1}{\Gamma(\nu)}\sum_{m=0}^{[n/2]}(-1)^m\frac{\Gamma(\nu+n-m)}{m!(n-2m)!}(2x)^{n-2m}. \tag{A2}$$

The square brackets in the upper limit of the summation represent the operation of taking the integer part of the number. For convenience in the calculations we shall henceforth assume that ν is an integer.

If $n=2N$, we transform the polynomial $C_n^{(\nu)}(x)$ to

$$C_{2N}^{(\nu)}(x)=\frac{1}{\Gamma(\nu)}\sum_{m=0}^{N}(-1)^m\frac{\Gamma(\nu+2N-m)}{m!(2(N-m))!}(2x)^{2(N-m)},$$

and make the change of variable $p=N-m$:

$$C_{2N}^{(\nu)}=\frac{(-1)^N}{\Gamma(\nu)}\sum_{p=0}^{N}(-1)^p\frac{\Gamma(\nu+N+p)}{(N-p)!(2p)!}(2x)^{2p}. \tag{A3}$$

Similarly, for $n=2N+1$ we obtain

$$C_{2N+1}^{(\nu)}=\frac{(-1)^N}{\Gamma(\nu)}\sum_{p=0}^{N}(-1)^p\frac{\Gamma(\nu+N+p+1)}{(N-p)!(2p+1)!}(2x)^{2p+1}. \tag{A4}$$

We substitute expressions (A3) and (A4) into (A1):

$$\begin{aligned}
&(1+\xi^2-2\xi\cos\chi)^{-\nu}\\
&=\sum_{n=0}^{\infty}[C_{2n}^{(\nu)}(\cos\chi)\xi^{2n}+C_{2n+1}^{(\nu)}(\cos\chi)\xi^{2n+1}]\\
&=\sum_{n=0}^{\infty}\Bigg[\xi^{2n}\frac{(-1)^n}{\Gamma(\nu)}\sum_{p=0}^{n}(-1)^p\frac{\Gamma(\nu+n+p)}{(n-p)!(2p)!}(2\cos\chi)^{2p}\\
&+\xi^{2n+1}\frac{(-1)^n}{\Gamma(\nu)}\sum_{p=0}^{n}(-1)^p\frac{\Gamma(\nu+n+p+1)}{(n-p)!(2p+1)!}\\
&\times(2\cos\chi)^{2p+1}\Bigg].
\end{aligned}$$

In the last expression we interchange the order of the summation and make the change of variable $m=n-p$. As a result, we obtain

$$(1+\xi^2-2\xi\cos\chi)^{-\nu}=\sum_{p=0}^{\infty}F_p^{(\nu)}(\xi)(\cos\chi)^p, \tag{A5}$$

where

$$F_p^{(\nu)}(\xi)=\frac{(2\xi)^p}{\Gamma(\nu)p!}\sum_{m=0}^{\infty}(-1)^m\frac{\Gamma(\nu+m+p)}{m!}\xi^{2m}. \tag{A6}$$

In order to obtain a simpler expression for the function F_p^ν, we consider the following sum:

$$\begin{aligned}
&\sum_{m=0}^{\infty}(-1)^m\frac{\Gamma(K+m)}{m!}z^m\\
&=\left(\frac{\partial}{\partial z}\right)^{K-1}z^{K-1}\sum_{m=0}^{\infty}(-1)^m z^m=\left(\frac{\partial}{\partial z}\right)^{K-1}\frac{z^{K-1}}{z+1}\\
&=\sum_{j=0}^{K-1}\binom{K-1}{j}\left(\frac{\partial}{\partial z}\right)^{j}\frac{1}{z+1}\left(\frac{\partial}{\partial z}\right)^{K-1-j}z^{K-1}\\
&=\frac{(K-1)!}{(z+1)^K}\sum_{j=0}^{K-1}\binom{K-1}{j}(-1)^j(z+1)^{K-1-j}z^j\\
&=\frac{\Gamma(K)}{(z+1)^K}.
\end{aligned}$$

Thus

$$\sum_{m=0}^{\infty}(-1)^m\frac{\Gamma(K+m)}{m!}z^m=\frac{\Gamma(K)}{(z+1)^K}, \tag{A7}$$

where $\binom{i}{j}$ is the binomial coefficient and $\Gamma(n)$ is the gamma function. We now substitute (A7) into formula (A6) and finally obtain

$$\begin{aligned}
F_p^{(\nu)}(\xi)&=\frac{\Gamma(\nu+p)}{\Gamma(\nu)\Gamma(p+1)}\frac{(2\xi)^p}{(1+\xi^2)^{\nu+p}}\\
&=\frac{(\nu+p-1)!}{(\nu-1)!p!}\frac{(2\xi)^p}{(1+\xi^2)^{\nu+p}}.
\end{aligned} \tag{A8}$$

[*] E-mail: chishko@ilt.kharkov.ua

---

[1] M. L. Klein and J. A. Venables (eds.), *Rare Gas Solids*, Academic Press, New York (1977).

[2] V. G. Manzhelii and Yu. A. Freiman (eds.), *Physics of Cryocrystals*, AIP Press, New York (1997).

[3] J. G. Dash, Fiz. Nizk. Temp. **1**, 839 (1975) [Sov. J. Low Temp. Phys. **1**, 401 (1975)].

[4] K. J. Standburg, Rev. Mod. Phys. **60**, 161 (1988).

[5] M. H. W. Chan, A. D. Migone, K. D. Miner, and Z. R. Li, Phys. Rev. B **30**, 2681 (1984).

[6] R. D. Etters and B. Kuchta, J. Low Temp. Phys. **111**, 272 (1998).

[7] D. S. Greywall, Phys. Rev. B **41**, 1842 (1990).

[8] M. Siqueira, J. Niéki, B. Cowan, and J. Saunders, Phys. Rev. Lett. **78**, 2600 (1997).

[9] K. Ishida, M. Morishita, K. Yawata, and H. Fukuyama, Phys. Rev. Lett. **79**, 3451 (1997).

[10] C. Bauerle, J. Bossy, Yu. M. Bunkov, A. S. Chen, and H. Gogfrin, J. Low Temp. Phys. **110**, 345 (1998).

[11] M. Roger, C. Bauerle, Yu. M. Bunkov, A. S. Chen, and H. Gogfrin, Phys. Rev. Lett. **80**, 1308 (1998).

[12] O. E. Vilches, R. C. Ramos, Jr., and D. A. Ritter, Czech. J. Phys. **46**, Suppl. S1, 397 (1996).

[13] C. Kittel, *Introduction to Solid State Physics*, 5th ed. [Wiley, New York (1976); Nauka, Moscow (1978)].

[14] K. A. Chishko, Fiz. Nizk. Temp. **13**, 296 (1987) [Sov. J. Low Temp. Phys. **13**, 168 (1987)].

[15] I. V. Komarov, L. I. Ponomarev, S. Yu. Slavyanov, *Spheroidal Functions* [in Russian], Nauka, Moscow (1976).

[16] M. Abramowitz and I. A. Stegun (eds.), *Handbook of Mathematical Functions* [Dover New York (1965); Nauka, Moscow (1979)].

[17] L. D. Landau and E. M. Lifshitz, *Statistical Physics*, 2nd ed. [Pergamon Press, Oxford (1969); Nauka, Moscow (1964)].

[18] T. N. Antsygina, K. A. Chishko, and V. A. Slusarev, Phys. Rev. B **55**, 3548 (1997).

[19] S. Flügge, *Practical Quantum Mechanics* [Springer-Verlag, Berlin (1971); Mir, Moscow (1974)].

Translated by Steve Torstveit

LOW TEMPERATURE PHYSICS VOLUME 26, NUMBER 4 APRIL 2000

Structure and thermal expansion of the low-temperature phase of SF_6

A. P. Isakina* and A. I. Prokhvatilov

B. I. Verkin Phyysicotechnical Institute for Low Temperature Physics, National Academy of Sciences of Ukraine, Lenin prospect, 47, 61164 Kharkov, Ukraine

J. Rodríguez-Carvajal

Laboratory Leon Brillouin, CEA Saclay, 91191 Gif-sur-Yvette Cedex, France

(Submitted November 12, 1999; revised December 6, 1999)
Fiz. Nizk. Temp. **26**, 404–414 (April 2000)

Powder x-ray and neutron diffraction studies of the crystalline structure, lattice parameters, and thermal expansion coefficients of sulfur hexafluoride SF_6 are performed in the temperature range 1.64–110 K. It is shown that the low-temperature phase (at $T<94.3$ K) is monoclinic, space group $C2/m(C_{2k}^3)$, with $Z=6$, in which 1/3 of the SF_6 molecules occupy the positions of higher symmetry $(2/m)$ and 2/3 of the molecules the lower one (m). As follows from the analysis of the structural results obtained, the availability of two types of molecular local symmetry positions is responsible for the anisotropic character of molecular rotation and the presence of features on the temperature dependences of the structural and thermodynamic properties of SF_6 crystals in the low-temperature phase, especially near T_c of the orientational phase transition. A detailed comparison the present results with the known data in the literature is carried out. © *2000 American Institute of Physics.* [S1063-777X(00)01204-4]

INTRODUCTION

Sulfur hexafluoride SF_6 crystallizes into a cubic bcc lattice of space symmetry $Im3m(O_h^9)$ at 222.4 K. As the temperature is decreased, there occurs a polymorphic transformation at 94.5 K which results in further orientational ordering of the molecules and a decrease of the crystal symmetry. The orientational structure of the high-temperature phase (β phase) has been studied by x-ray,[1,2] neutron diffraction,[3] and electron diffraction[4–6] techniques. It is found that in the vicinity of the phase transition the molecular S-F bonds are mainly oriented along the {100} direction of the bcc lattice. But the orientational motion of the molecules in this phase is characterized, particularly at high temperatures, by high librations (the deviation of the S-F bonds from the direction along the lattice axes may be as much as 20°) and fast reorientations, resulting in a high degree of dynamic disorder. As follows from Refs. 7 and 8, the disorder results from the fundamental difference in the interaction with the first- and second-nearest neighbors, producing a frustration of the orientational structure of the high-temperature phase of SF_6.[9]

The data on crystal structure of the low-temperature phase of SF_6 are quite contradictory. The results given in Refs. 3, 4, 6, 10, and 11 even suggest that the orientational ordering in SF_6 occurs by stages and is followed by the formation of an intermediate, partially ordered phase. According to the electron diffraction data[4,5] obtained on the films, this phase is a hexagonal one of rhombohedral symmetry $P3m1(D_{3d}^3)$ at temperatures from 50 to 94 K. At $T<50$ K a slight phase distortion to a base-centered monoclinic lattice was also observed. The intermediate rhombohedral phase was also obtained by molecular-dynamics (MD) simulations;[10,11] in this structure only 2/3 of the molecules are orientationally ordered. At the same time, neutron powder experiments[7,8,12] have demonstrated the existence of only one low-temperature phase, with a triclinic lattice $P\overline{1}(Z=3)$. The neutron diffraction studies by Cockcroft and Fitch[13] (1988) favor the view that there is no second phase transition at $T\approx 50$ K. According to their data, the low-temperature phase of SF_6 has a monoclinic lattice of space group $C2/m(C_{2h}^3)$, with six molecules per unit cell.

In that context, we reasoned that a reexamination of the low-temperature experiments using combined high-resolution neutron and x-ray diffraction studies of SF_6 should be performed to elucidate conclusively the structure of the low-temperature phase and to obtain the data still unavailable, on vibrational anharmonicity and the dynamics of molecular rotational motion. The solution of the latter problems has been made possible by our x-ray dilatometric measurements of the linear and volume expansion coefficients within the 4.2–94 K temperature range and analysis of the thermodynamic characteristics.

EXPERIMENTAL PROCEDURE

The neutron powder studies were carried out at the Laboratory Leon Brillouin (LLB), Saclay (France), on a G42 high-resolution spectrometer using radiation at wavelengths of 1.979 Å and 2.596 Å (from the (115) and (004) planes, respectively, of the Ge monochromator) at several temperatures in the range 1.64–110 K. The angular resolution of the spectrometer was discussed in detail in Ref. 14. The samples were prepared by condensing 99.99% pure SF_6 gas in a closed vessel at liquid-nitrogen temperature. In this process a snowlike mass was formed which was then used to fill the cylindrical specimen chamber. Thereafter the chamber was quickly placed into a helium cryostat vessel, which was mounted on the spectrometer and preliminarily cooled down to 1.5 K. The minimum temperature of the neutron powder

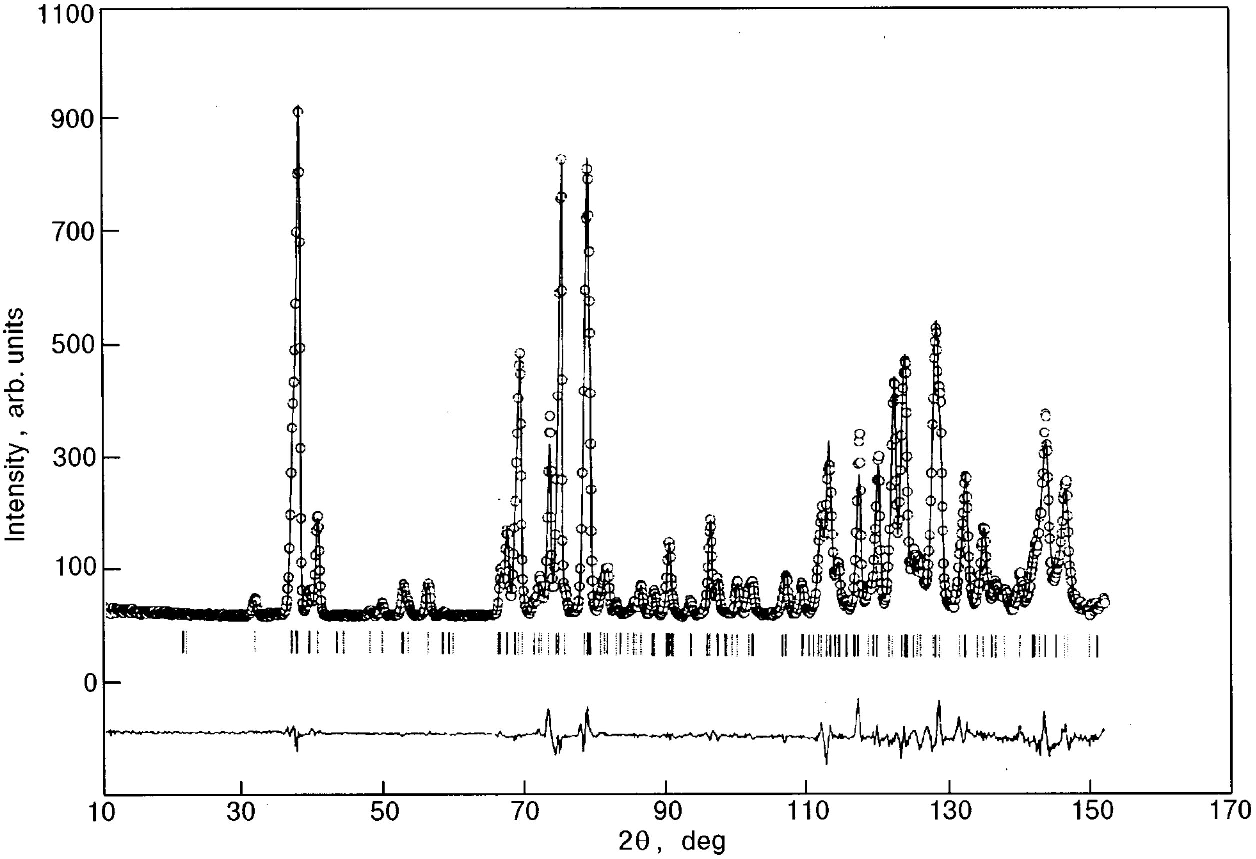

FIG. 1. Observed, calculated, and difference profiles for α-SF_6 neutron powder diffraction pattern at 1.64 K ($\lambda = 2.59$ Å). Vertical bars indicate the calculated reflection positions.

measurements was 1.64 K. The sample temperature at each point was stabilized with an accuracy of ±0.01 K. The experiments made it possible to collect and analyze the neutron diffraction data in the reflection angle range from 2Θ to 158 ($Q_{\max}=6.3\,\text{Å}^{-1}$) with a 0.02° step size scan.

The x-ray measurements were made at the Institute for Low Temperature Physics and Engineering (Kharkov) on a special helium cryostat mounted on a standard DRON-4 x-ray powder diffractometer using Co radiation of a wavelength of 1.79021 Å. The cryostat used enabled variation of the temperature of the samples in the interval 4.2–300 K and stabilization of the temperature values to within ±0.05 K. The samples were obtained by condensation of SF_6 gas of purity 99.98% on a flat copper substrate cooled to 125 K in the cryostat. The samples were then annealed at 140 K to eliminate stresses and to reduce the number of defects. It was found that the condensation of SF_6 gas onto a lower-temperature substrate produces severely stressed samples, the annealing of which is followed by intense recrystallization and generation of coarse-grained samples, resulting in a lower reliability of the polycrystal x-ray data. The reflections of the analytically pure copper covering the specimen chamber substrate were a modified intrinsic reference for precision estimation of the lattice parameters. The lattice parameters were estimated by the mean-square method at separate temperatures (4.5, 60, and 78 K) with an error of no more than 0.02%. To estimate the parameters, the whole set of experimental x-ray reflections (about 40 reflections) observed in the angular range $2\Theta = 20-91°$ was used. The temperature dependence of the lattice parameters in the interval between the above reference points was investigated by measuring the angular positions of the ten most intense reflections. The regions of a possible low-temperature phase transition ($40\,\text{K} < T < 60\,\text{K}$) and the well-known high-temperature one (at 94.3 K) were studied with a temperature step of 1–2 K, and the intermediate region with a step of 5 K.

RESULTS

Structure. Our neutron and x-ray diffraction data on the low-temperature phase demonstrate that in the whole temperature range of 1.64 to 94 K the crystal structure of SF_6 undergoes no essential modifications which might be attributed to the second phase transition that, as speculated in Refs. 4 and 5, may occur at ~50 K. To obtain more-convincing evidence, we analyzed the temperature dependences of the half-width and intensity of the most pronounced x-ray reflections. If a phase transition did occur, one might expect visible anomalies in the temperature dependences of the x-ray reflection widths or intensities, but the experiments revealed no anomalies. The additional high-symmetry phases observed in Refs. 4 and 5 are most likely nonequilibrium and resulted from either the specific features of the technique of sample preparation or from size effects in the thin films. The authors of Ref. 9 also consider that massive equilibrium samples have no intermediate phase of hexagonal symmetry, and the two stages of orientational ordering of molecules observed in Ref. 4 owe their origin to the

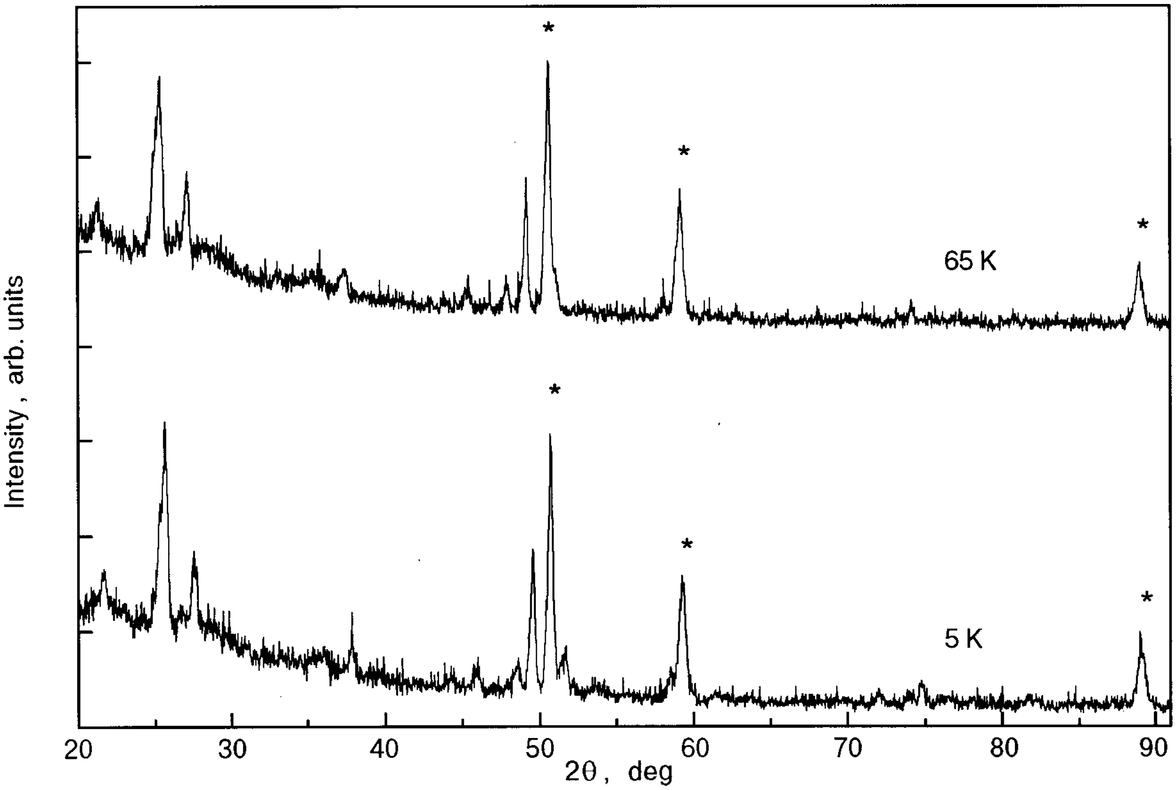

FIG. 2. X-ray powder diffraction pattern of α-SF_6 at 5 and 65 K ($\lambda = 1.79021$ Å). Asterisks mark the reference (pure Cu) reflections.

effect of the surface on the kinetics of phase transitions in the thin films of SF_6. Thus our experiments provide support for the neutron-diffraction[13] and calorimetric[15] results on the unique solid-solid phase transition which occurs at $T = 94.3$ K.

Of all the experimental data on the structure of the low-temperature phase, we consider the results given in Ref. 13 to be the most comprehensive and reliables. The diffraction pattern observed in our neutron-diffraction experiments is qualitatively similar to that shown in Ref. 13. For purposes of comparison, Figs. 1 and 2 show a neutron ($T = 1.64$ K) diffraction pattern and x-ray diffraction patterns for two temperatures (5 and 65 K). Since the natures of neutron and x-ray diffraction scattering by crystals are dissimilar, the latter method gives a poorer diffraction pattern. We managed to take only the most pronounced reflections, and a number of doublets and multiplets remained unseparated. Therefore, to index correctly the x-ray reflections, we invoked a visual similarity of the diffraction patterns shown in Figs. 1 and 2. The set of reflections taken is adequately indexed with the assumption of the monoclinic cell proposed in Ref. 13. Using the neutron-diffraction data for 1.64 K, we obtained the following lattice parameters: $a = 13.803$ Å, $b = 8.139$ Å, $c = 4.749$ Å, $\beta' = 95.586°$, which are in good agreement within the limits of experimental error with the data of Ref. 13 for $T = 5$ K and our x-ray data for $T = 4.5$ K. Recall that the x-ray lattice parameters were found by averaging over the whole set of reflections in a diffraction angle range up to $2\Theta = 91°$ by the method of least squares and by refining the true reflection angles as compared to the reference. The x-ray lattice parameters at 4.5 K were as follows: $a = 13.813$ Å, $b = 8.144$ Å, $c = 4.752$ Å, $\beta' = 95.59°$.

The Rietveld analysis of the collected neutron data performed with the use of the FULLPROF code[14] substantiated the suppositions made in Ref. 13, according to which the low-temperature monoclinic phase structure of SF_6 belongs to the symmetry space group $C2m(C_{2h}^3)$ with $Z = 6$. At the first stage of the structural model refinement, isotropic thermal factors with the coefficients B equal to 0.94 and 2.21 Å^2 for the S and F atoms, respectively, were applied. These values were obtained by using the data on the Debye temperature and on the mean-square displacements of molecules in the high-temperature phase.[2] The ultimate Rietveld refinement of the structure at 1.64 K was also made with the inclusion of an absorption correction and anisotropic thermal factors.

Unlike the authors of Ref. 13, we were already with an isotropic approach and obtained successful good agreement between the calculated and measured neutron scattering spectra (see Fig. 1) with a reliability structure factor of $R = 3.94\%$ at 1.64 K and, besides, with the intramolecular bonds of the SF_6 octahedrons remaining undistorted. The molecules held the shape of a regular octahedron with an S-F bond length of 1.56 Å. Besides, the peak-width parameters U, V, W (0.1872, -0.3105, 0.4807 (deg)^2, respectively) resulted in no broadening of the calculated reflection profiles compared to the experimental ones. Table I lists the improved parameters of the SF_6 structural model for refined isotropic thermal factors at temperatures 1.64 and 75 K. A 3D image of the structure obtained is shown schematically in Fig. 3. It should be noted that according to the structure data (Table I) the SF_6 molecules occupy two types of positions in the monoclinic lattice, with dramatically different point sym-

TABLE I. The refined structural parameters from neutron scattering data for a powder sample of SF_6 at 1.64 and 75 K. Space group $C2/m(C_{2h}^3)$, $Z=6$. x, y, z are the relative coordinates of the atoms.

Parameter	$T=1.64$ K	$T=75$ K
Cell constants		
a, Å	13.8028	13.9410
b, Å	8.1392	8.1946
c, Å	4.7494	4.7969
β′, deg	95.586	95.172
Half-width parameters, $(\deg)^2$		
U	0.1872(1)	0.1559(1)
V	−0.3105(3)	−0.3913(3)
W	0.4807(1)	0.5320(8)
R-Bragg factor, %	3.94	5.27

Atom	Site symmetry	Occupation	x	y	z	x	y	z
S_1	$2/m$	0.25	0	0	0	0	0	0
F_1	m	0.5	0.0686	0	0.2815	0.0686	0	0.2752
F_2	1	1	0.0641	0.1355	−0.1221	0.0628	0.1344	−0.1238
S_2	m	0.5	0.6684	0	0.5844	0.6685	0	0.5906
F_3	m	0.5	0.7470	0	0.3693	0.7464	0	0.3771
F_4	m	0.5	0.5897	0	0.7995	0.5907	0	0.8041
F_5	1	1	0.7264	−0.1356	0.7616	0.7260	−0.1344	0.7649
F_6	1	1	0.6103	−0.1356	0.4072	0.6114	−0.1344	0.4163

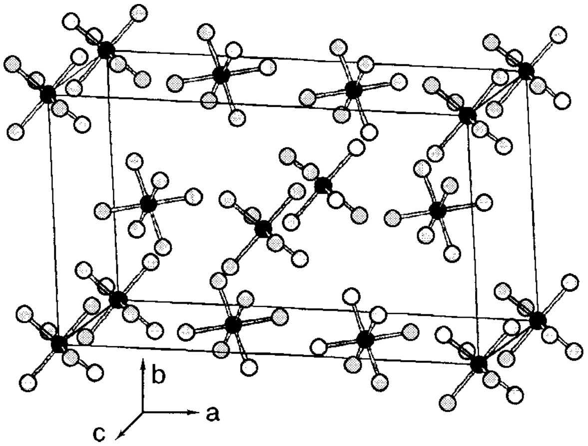

FIG. 3. Monoclinic structure (space group $C2/m$, $Z=6$) of the low-temperature phase of SF_6.

metry. As the projection of the structure on the monoclinic plane (a, c) shows (Fig. 4), one-third of the molecules, with the S atoms in the (0,0,0) position, have the highest local symmetry $2/m$ possible in the space group under consideration. Hence, with increase in temperature the intensity and amplitudes of rotational motion of these molecules is likely to be higher than that for the remaining 2/3 of the molecules, in the position (x,0,z) with a lower local symmetry m. It will be shown below that the presence of these two types of molecules in the structure has the determining influence on the thermodynamic properties of the low-temperature phase of sulfur hexafluoride.

The structural model and the thermal factors B were refined in the isotropic approximation using neutron diffraction data for each temperature studied. As a result, information was derived which describes the temperature variation of the effective isotropic thermal factor B of the molecules occupying the two different positions. These results are shown in Fig. 5. At low temperatures ($T<40$ K) the values of the coefficients B are very low and practically similar for molecules having different local symmetries. Above 40 K the one-third of the molecules which are at the sites of the higher point symmetry $2/m$ have larger B values, and we observe a more intensive growth of these values with temperature as compared to the molecules at the sites of symmetry m. This behavior of $B(T)$ indicates that rising temperature leads to considerable enhancement of the rotational motion of the molecules at the $2/m$ positions. It is possible that the rotational motion becomes nearly free in the vicinity of T_c. This assumption is supported by our analysis of the thermodynamic characteristics of the low-temperature phase. The presence of two types of such molecules in the α-SF_6 crystals may be one of the reasons for the appearance of the intermediate metastable phase in specially prepared samples. For example, this may cause the formation of a rhombohedral symmetry phase in thin SF_6 films in the range 50 K-T_c (Refs. 4 and 5). Using the data of Ref. 13, we have calculated the effective values of the isotropic B factor at 5 and 60 K. Along with the data directly measured at 115 K,[13] our calculated results are systematically higher both in the low- and high-temperature phases (see Fig. 5). Also of interest is the fact that when using the data of Ref. 13, anomalously high B factors appear even at helium temperatures. These values correspond to our present results at 40 K. The probable reason for the observed systematic discrepancy of $B(T)$ may be the difference in the purity and structural perfection of the samples used in these two studies.

Lattice parameters. For the purpose of obtaining data on the thermal expansion of α-SF_6, we measured in detail the variations with temperature of the angular positions of the

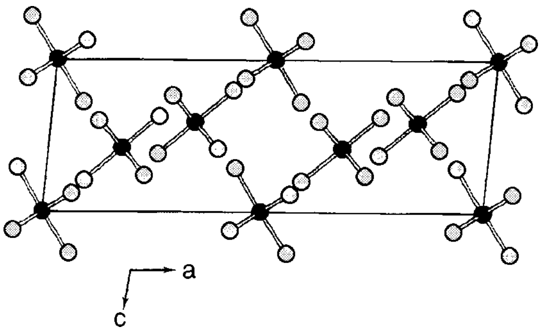

FIG. 4. Unit cell projection of α-SF_6 on the monoclinic plane (a, c).

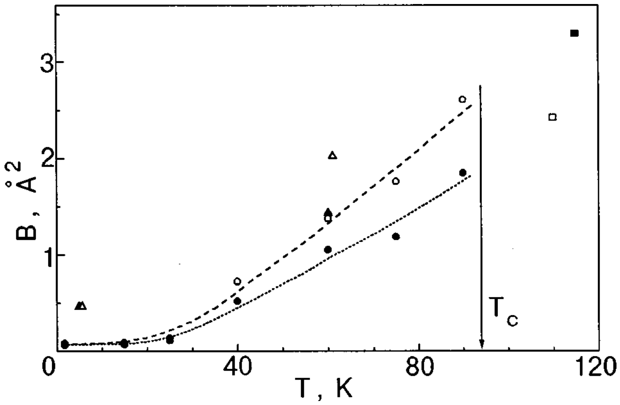

FIG. 5. Temperature change of the isotropic thermal coefficient *B*: ○, ●-the data for molecules at local symmetry positions 2/*m* and *m* in the low-temperature phase, respectively; △, ▲-the same data calculated with the use of the experimental data of Ref. 13; □ and ■-our previous data from Refs. 2 and 13 for the high-temperature phase. T_c is the temperature of the solid-solid phase transition.

most intense reflections in the x-ray diffraction experiments. That made it possible to determine reliably the temperature dependences of the lattice parameters and to estimate the thermal expansion coefficients from them. We found that our x-ray and neutron diffraction data on the lattice parameters agree satisfactorily with each other over the whole temperature existence region of the low-temperature phase and that they also allow us to estimate their consistency with the results given in Ref. 13. The temperature variations of the lattice parameters and the monoclinic angle are shown in Fig. 6, and those of the molar volume and its jump at the phase transition are illustrated in Fig. 7 together with the available data from the literature. The observed slight disagreement of the lattice parameters with the data given in Ref. 13 may be attributed to two reasons. The authors of Ref. 13 employed a SF_6 gas of insufficiently high purity −99.9% (we used 99.99% pure gas), resulting, as a rule, in considerable (and in some cases gigantic) anomalies of the physical properties at low temperatures and producing an appreciable effect on the dynamics of the crystal lattices.[23] On the other hand, contrary to the present x-ray and neutron diffraction measurements, the experiments in Ref. 13 were performed on a sample that was not free (the sample was grown in a glass ampoule at high temperatures, cooled to 77 K, and then quenched quickly down to liquid-helium temperature), and hence, the sample might have had high stresses of the first kind.

Extrapolation of the temperature dependence of the lattice volume to the phase transition temperature (94.3 K) results in the value $V_m = 55.68\,\mathrm{cm}^3/\mathrm{mol}$, which nearly agrees with the value $V_m = 56.0\,\mathrm{cm}^3/\mathrm{mol}$ obtained by substracting the volume change at the transition ($\Delta V_m = 2.1\,\mathrm{cm}^3/\mathrm{mol}$ by the estimates in Ref. 24) from the high-temperature phase volume.[2] The value of the jump in volume measured within a narrow temperature range of 94 to 94.5 K in the vicinity of the phase transition turns out to be somewhat higher than that expected from the estimation by the Clausius-Clayperon equation in Ref. 24 and amounts to 2.57 $\mathrm{cm}^3/\mathrm{mol}$ (approximately 4.4%), but this value is lower than the change in density at the transition (6%) obtained in the pycnometric

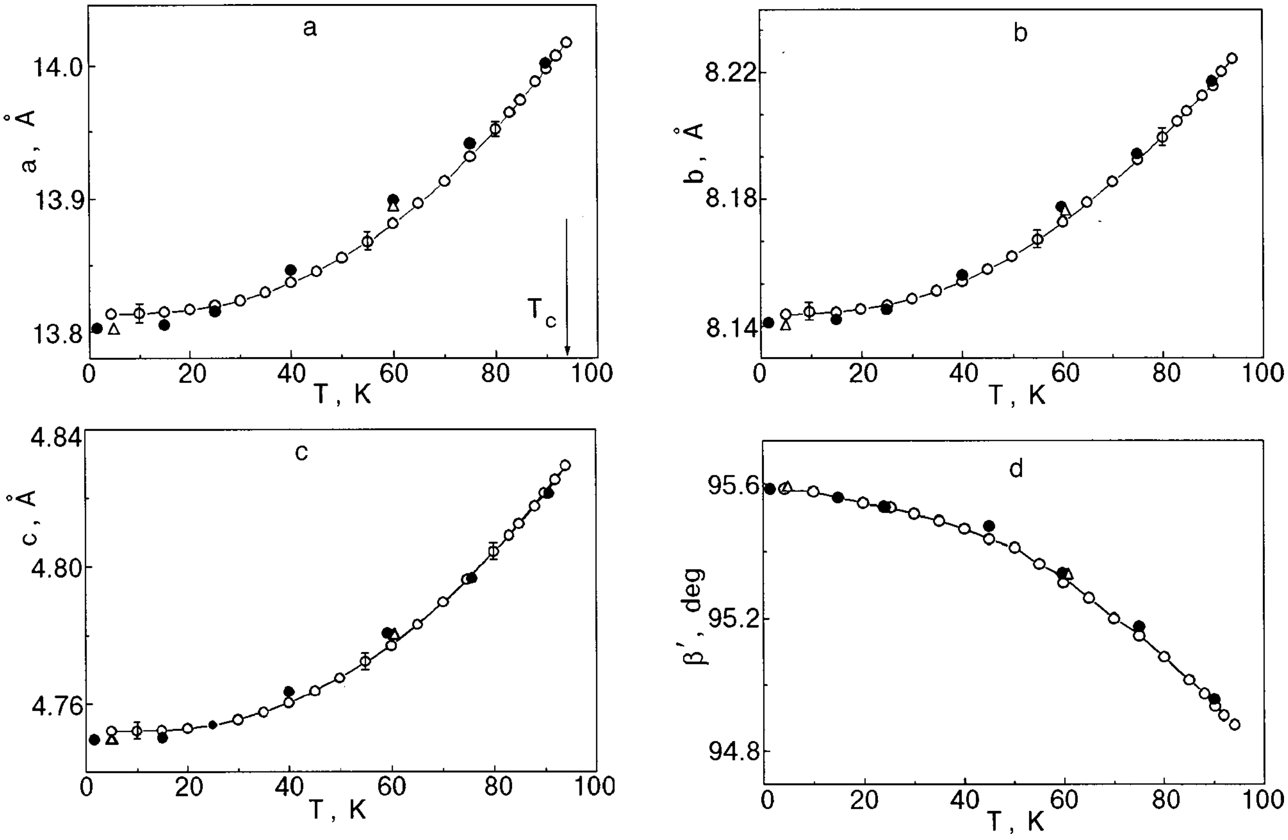

FIG. 6. Temperature dependences of *a* (a), *b* (b), *c* (c), β' (d), the lattice parameters of monoclinic phase of SF_6: ○, ●-the data obtained in present work by x-ray and neutron methods, respectively; Δ corresponds to the results obtained in Ref. 13. T_c is the temperature of the solid-solid phase transition.

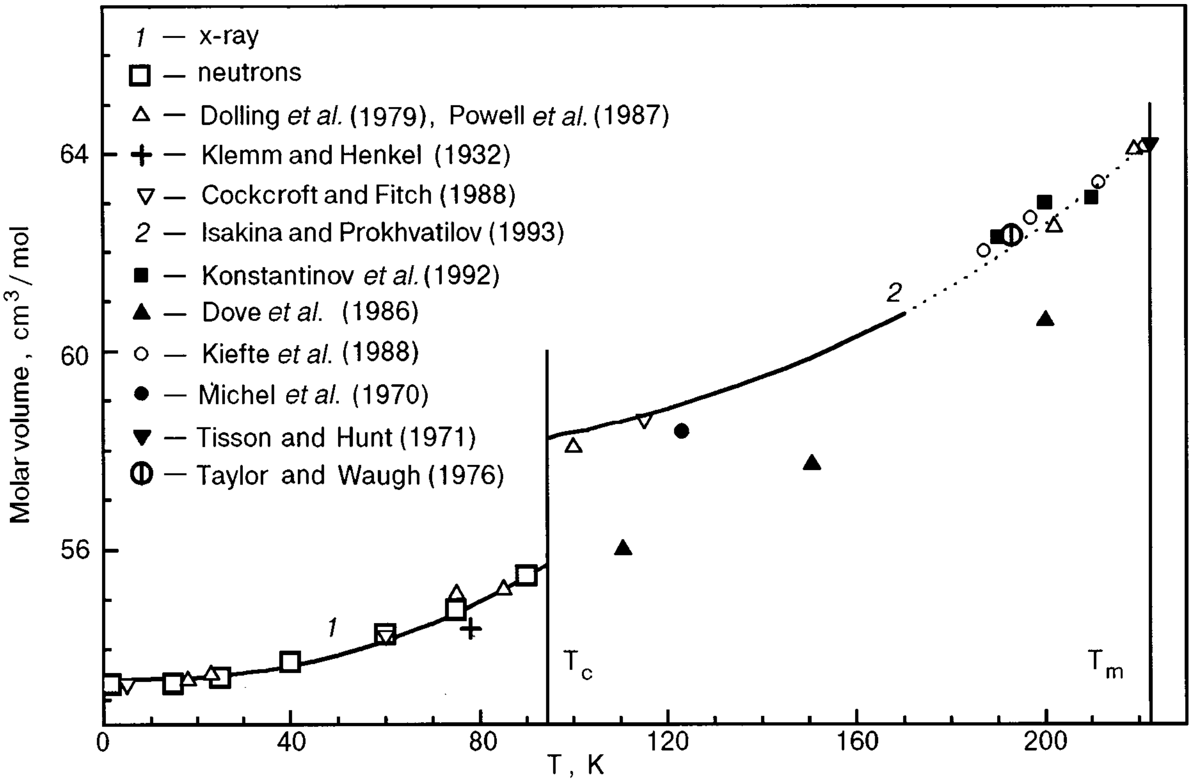

FIG. 7. Temperature dependences of the molar volume of SF_6 in the low- and high-temperature phases: 1 and □ show the data obtained in present work; 2 was obtained in Ref. 2, ● in Ref. 1, △ in Refs. 3, 16, ∇ in Ref. 13, + in Ref. 17, ■ in Ref. 18, ▲ in Ref. 19, ○ in Ref. 20, ∇ in Ref. 21, ϕ in Ref. 22. T_c and T_m correspond to the temperatures of phase transition and melting point, respectively.

measurements reported in Ref. 17. As is evident from Fig. 7, our temperature dependence of the molar volume is in good agreement with all of the experimental and theoretical estimates except for the data of Ref. 19, which appear to be much lower. The last fact seems to be responsible for the increased value of the change in density at the transition in Ref. 19.

Thermodynamic properties. The temperature dependences of the linear expansion coefficients, illustrating the character of expansion anisotropy in α-SF_6, are shown in Fig. 8. Our attention is engaged by the fact that, beginning just with 50 K, the temperature dependences of the linear α_a, α_c and volume β expansion coefficients become more pronounced. As will be shown below, this behavior is mainly dictated by the variations in the dynamics of molecular rotational motion in the monoclinic lattice at this temperature. The numerical values of the lattice parameters and molar volume, together with the thermal expansion coefficients, are listed in Table II.

The solid-solid phase transition and the peculiarities of physical properties of SF_6 crystals, as of other molecular cryocrystals, are a consequence of variations in the rotational subsystem. Observation and identification of these variations can be done by the method of separating the contributions of the phonon and rotational subsystems to the lattice dynamics.[26] The data on the thermal expansion coefficients enabled us to apply this method, along with published data[15] on the heat capacity at constant pressure C_P, to recognize and to analyze the rotational component of the heat capacity at constant volume $C_{\rm rot}$.

With allowance made for all type of vibrations in the lattice and their mutual independence being assumed, the heat capacity of a molecular crystal can be given as a sum of contributions from the translational and rotational subsystems and a contribution due to the intramolecular vibrations of the atoms:

$$C_V = C_{\rm tr} + C_{\rm rot} + C_{\rm in}. \qquad (1)$$

The heat capacity at constant volume, C_V, is difficult to measure. In practice, it is calculated, when data on the thermal expansion and compressibility are available, from the values of the heat capacity at constant pressure, C_P, by using the known thermodynamic relation

$$C_P - C_V = \beta^2 VT/\chi_T. \qquad (2)$$

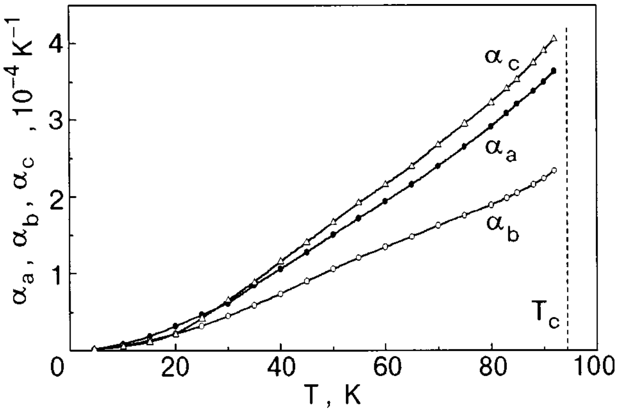

FIG. 8. Linear thermal expansion coefficients versus temperature. T_c is the temperature of the solid-solid phase transition.

TABLE II. Experimental x-ray (a) and neutron (b) values of the lattice parameters (a,b,c,β'), molar volume (V_m), density (ρ), linear ($\alpha_a,\alpha_b,\alpha_c$), and volume ($\beta$) thermal expansion coefficients.

T, K	a, Å	b, Å	c, Å	β', deg	V_m, cm^3/mol	ρ, g/cm^3	α_a	α_b	α_c	β
							10^{-4} K^{-1}			
a)										
4.5	13.813	8.144	4.752	95.59	53.40	2.735	⋯	⋯	⋯	⋯
10	13.814	8.144	4.752	95.58	53.41	2.735	0.08	0.06	0.05	0.19
15	13.815	8.145	4.752	95.56	53.42	2.734	0.18	0.13	0.11	0.42
20	13.818	8.146	4.753	95.54	53.44	2.733	0.32	0.22	0.21	0.75
25	13.820	8.147	4.754	95.53	53.47	2.732	0.47	0.32	0.42	1.21
30	13.824	8.149	4.755	95.51	53.52	2.729	0.54	0.45	0.66	1.65
35	13.830	8.151	4.758	95.49	53.58	2.726	0.85	0.59	0.89	2.33
40	13.837	8.154	4.760	95.46	53.66	2.722	1.06	0.74	1.16	3.00
45	13.846	8.158	4.764	95.43	53.76	2.717	1.28	0.90	1.43	3.74
50	13.856	8.162	4.768	95.40	53.88	2.711	1.51	1.06	1.68	4.43
55	13.868	8.167	4.772	95.36	54.01	2.704	1.72	1.21	1.92	5.05
60	13.882	8.173	4.777	95.32	54.16	2.697	1.94	1.35	2.16	5.66
65	13.897	8.179	4.783	95.26	54.34	2.688	2.16	1.48	2.40	6.25
70	13.913	8.185	4.790	95.20	54.52	2.679	2.40	1.63	2.68	6.87
75	13.932	8.192	4.797	95.15	54.73	2.669	2.65	1.76	2.95	7.54
80	13.952	8.200	4.804	95.08	54.95	2.658	2.91	1.89	3.23	8.18
83	13.965	8.205	4.809	95.04	55.09	2.651	3.09	1.98	3.41	8.62
85	13.974	8.208	4.813	95.01	55.19	2.649	3.21	2.05	3.53	8.91
88	13.988	8.213	4.818	94.97	55.34	2.639	3.38	2.16	3.75	9.36
90	13.998	8.217	4.821	94.94	5.45	2.634	3.50	2.24	3.91	9.68
92	14.008	8.220	4.825	94.91	55.56	2.629	3.64	2.34	4.06	10.02
94	14.017	8.224	4.829	94.88	55.67	2.623	⋯	⋯	⋯	⋯
b)										
1.64	13.8028	8.1392	4.7494	95.586	53.301	2.7401				
15	13.8053	8.1399	4.7500	95.560	53.323	2.7390				
25	13.8165	8.1446	4.7539	95.530	53.438	2.7331				
40	13.8463	8.1561	4.7633	95.475	53.748	2.7173				
60	13.8976	8.1772	4.7805	95.330	54.294	2.6900				
75	13.9410	8.1946	4.7969	95.172	54.780	2.6662				
90	14.0024	8.2174	4.8210	94.952	55.468	2.6330				

The calculations of C_V for the low-temperature phase of SF$_6$ were made difficult by the lack of data on the compressibility χ_T. The compressibility of SF$_6$ was studied in Ref. 24 by the piston displacement method in the 81–190 K temperature and 0–20 kbar pressure ranges. But in the above paper primary attention was given to the P-T diagram and the phase transition characteristics. A numerical value of the isothermal compressibility was cited only for the high-temperature phase at $T=182$ K ($\chi_T=2.93\cdot 10^5$ cm^2/kg). In a previous paper,[2] in order to estimate compressibility everywhere over the existence region of the high-temperature phase (95–220 K) we used the data on the elastic constant obtained from an investigation of the Brillouin light scattering in SF$_6$ single crystals.[20] In the present paper these results, with allowance for their variations at the phase transition due to the large change in volume, were extrapolated to the existence region of the low-temperature phase. Moreover, it was assumed that at low temperatures the linear, though rather weak, dependence of the compressibility still persists. The temperature dependences of the heat capacity C_V thus calculated are shown in Fig. 9. The numerical values of the other thermodynamic characteristics of the low-temperature phase of SF$_6$ are also listed in Table III.

The heat capacity C_{in} was calculated from the characteristic temperatures $\Theta_i=h\nu_i/k$ in the Einstein model approximation with the use of the intramolecular vibrational frequencies ν_i cited in Ref. 27. The contribution of translational vibrations to the heat capacity was calculated in the Debye approximation with a characteristic temperature $\Theta_D=65$ K obtained from an analysis of the low-temperature part of the heat capacity.[15] As is evident from Fig. 9, the temperature dependence of C_{tr} decreases distinctly even at $T>30$ K, and in the vicinity of the phase transition temperature the heat

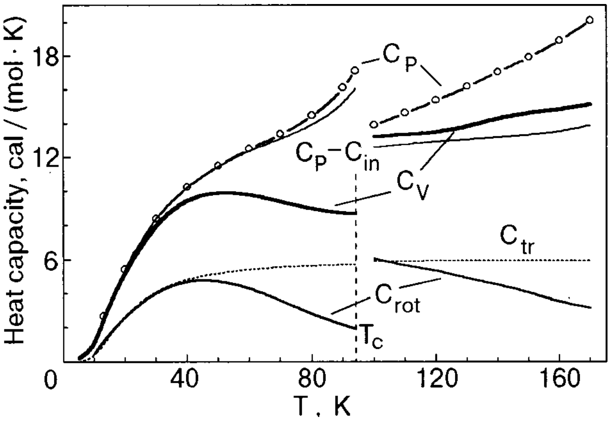

FIG. 9. Temperature dependence of the heat capacity contributions in α-SF$_6$: ○ show the data [14] on the heat capacity at constant pressure, C_P, while C_V, C_{in}, C_{tr}, and C_{rot} correspond to the calculated curves for the heat capacity at constant volume and for the intramolecular, translational, and rotational components of the heat capacity, respectively.

TABLE III. Adiabatic compressibility (χ_S), Grüneisen constant (γ), heat capacity at constant pressure (C_P) and constant volume (C_V), and the intramolecular ($C_{\rm in}$), lattice ($C_{\rm tr}$) and librational ($C_{\rm rot}$) components of the heat capacity of sulfur hexafluoride in the low-temperature phase.

T, K	χ_S, 10^{-11} cm^2/dyn	γ	C_P (Ref. 14)	C_V	$C_{\rm in}$	$C_{\rm tr}$	$C_{\rm rot}$
			cal/(mol·K)				
13	0.676	2.39	2.68	2.68	10^{-7}	1.05	1.66
20	0.685	2.58	5.41	5.39	10^{-6}	2.69	2.75
30	0.698	3.59	8.41	8.26	10^{-4}	4.09	4.18
40	0.712	5.25	10.26	9.65	10^{-3}	4.83	4.82
50	0.730	6.77	11.52	10.02	0.032	5.19	4.80
60	0.748	7.84	12.51	9.88	0.109	5.41	4.36
70	0.769	8.71	13.39	9.44	0.271	5.55	3.61
80	0.788	9.40	14.49	8.97	0.530	5.64	2.80
90	0.812	9.78	16.15	8.78	0.894	5.71	2.18
94	0.822	9.81	17.14	8.75	1.067	5.73	1.95

capacity values almost approach the high-temperature limit $3R=5.97$ cal/(mol·K).

The heat capacity of a librational subsystem $C_{\rm rot}=C_V-C_{\rm tr}-C_{\rm in}$ exhibits an extraordinary temperature dependence (Fig. 9). Considering that the low-temperature phase of SF_6 is completely orientationally ordered, for a system of three-dimensional rotators (librators) one may expect that the heat capacity $C_{\rm rot}$ will increase monotonically with temperature and, within the limit of free spherical rotation of molecules, may be close to $3R$ like the phonon heat capacity. Instead, one observes a reduction in the rotational component at $T>50$ K. Such behavior is usually observed only at rather high (pre-melting) temperatures for cryocrystals and may be a result of our not taking into account the anharmonicity of the angular and translational vibrations of the molecules.[26] A noticeable anharmonicity of the translational vibrations is unlikely at such low temperatures ($T<0.5T_{\rm tr}$, where $T_{\rm tr}$ is the triple-point temperature). Therefore, the reduction in the heat capacity is most likely due to the unhindering of the molecular rotational motion of one-third of the molecules in the α-SF_6 lattice to an almost free rotation, as is also confirmed by the data given in Ref. 28. For the above molecules the heat capacity value may not exceed $(3/2)R/3$. Then for the vibrational subsystem in which two-thirds of the molecules execute librational motion and one-third rotate freely, the total heat capacity in the vicinity of the phase transition can't exceed $2.5R$, in agreement with the results of our calculations (Fig. 9). Thus, the reduction in $C_{\rm rot}$ observed at $T>50$ K may be accounted for as being due to two sources. First, the heat capacity of the rotational subsystem decreases appreciably because of the unhindering of the molecular rotation from the strongly correlated motion to an almost free one. Secondly, the rotational anharmonicities are strongly enhanced as the phase transition point is approached. A similar behavior of the rotational heat capacity has also been observed[2] in the high-temperature phase of SF_6 (see Fig. 9). The numerical values of the thermodynamic characteristics are listed in Table III.

The Grüneisen constants, which are a measure of the lattice vibrational anharmonicity and its change with increase in temperature, presuppose, in the quasi-harmonic approximation, a homogeneous distortion of the spectrum with variation in volume and are given by the relation

$$\gamma_i=-d\ln\omega_i/d\ln V, \tag{3}$$

where ω_i are the lattice vibration frequencies and V is the crystal volume. From the Grüneisen law there follows a simple thermodynamic relation for calculation of the Grüneisen constants (parameters), which relates the fundamental thermodynamic characteristics of the material:

$$\gamma=\beta V/\chi_T C_V. \tag{4}$$

For most cryocrystals at low temperatures, where the effect of the librational subsystem is insignificant, the values of γ are within the range 2.2–2.9 (Ref. 26). Also within this range are the values of the Grüneisen parameters for the high-temperature phase of SF_6 obtained in Ref. 2. The librational component of γ which defines the anharmonicities in the librational subsystem is usually somewhat lower and equals 1.6–1.8 (Ref. 26). In our work we did not separate the lattice and librational contributions to the Grüneisen parameters because there are no experimental data on the temperature and volume dependences of the librational vibration spectrum.

The Grüneisen parameters calculated by Eq. (4) are shown in Fig. 10 along with the data for the high-temperature phase. Mention should be made of the unexpectedly considerable change in γ at the phase transition and the high values of the constants γ for the low-temperature phase as compared to the data for the cryocrystals known to us.

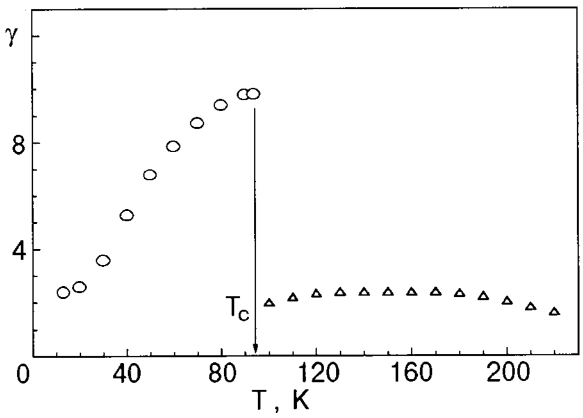

FIG. 10. Grüneisen parameters for the low- and high-temperature phases of SF_6: ○ show the data of the present work, △ were obtained in Ref. 2.

The rapid increase in γ as the phase transition temperature T_c is approached may be responsible for the fact that the anharmonicity of the librations and the orientational disordering of the SF_6 molecules have a more distinct influence on the thermal expansion coefficients of the crystal than on its heat capacity, as follows from Eq. (4) and the experimental dependence of the volume expansion coefficient β (see Table II).

Attention should be paid to the fact that the analysis of the low-temperature heat capacity at $T<20\,\mathrm{K}$ resulted in comparable phonon and librational contributions (within the limits of error). This result is physically unwarranted and may be a consequence of too-high experimental values[15] of C_P at the lowest temperatures of their estimation and also due to the lack of measurements of the heat capacity at temperatures below 13 K. The too-high values of the low-temperature heat capacity may have resulted from impurities in the samples. As mentioned above, even insignificant amounts of impurities (less than 0.01%) have an appreciable effect on the absolute values and behavior of the heat capacity of simple molecular crystals, particularly at low temperatures [23]. The lack of data on the heat capacity at $T<13\,\mathrm{K}$ makes it difficult to estimate a low-temperature value of the zero Debye temperature Θ_0. We believe, however, that no fundamental error has been made because the calculations were performed with $\Theta_0=65\,\mathrm{K}$, somewhat higher, as it should be, than the reliable value of the high-temperature Debye temperature, equal to $\Theta_\infty=62\,\mathrm{K}$.[2] If the calculations of C_{tr} were performed with higher values of Θ_0, we would obtain entirely unreasonable results—at $T<20\,\mathrm{K}$ the librational contribution to the heat capacity would be much higher than the translational one.

In conclusion, the results of a thermodynamic analysis of heat capacity are consistent with the data on the crystal structure of α-SF_6 given in Ref. 13 and in the present paper as well as with the theoretical deductions in Refs. 10 and 11. These results also support the assumption[28] that the peculiarities in the temperature dependences of the NMR linewidth and second moment observed in the 45–50 K temperature range are due not to the two-phase state of the samples used but to the fact that the SF_6 molecules occupy two types of positions in the lattice of the low-temperature phase and that these positions differ considerably in symmetry, which determines their rotational mobility. According to the data given in Ref. 28 the molecular orientation barriers in the two lattice positions differ by a factor of 1.5 and are equal to 1.94 and 2.8 kcal/mol for the high-and low-symmetry states, respectively. Gaining more-comprehensive information on the dynamics of rotational molecular motion in α-SF_6 will require supplementary investigation of the vibrational spectra by Raman and infrared spectroscopy techniques, sound velocity measurements, and careful study of the heat capacity, particularly at the lowest temperatures and on high purity samples.

The authors would like to thank the Office of the Laboratory Leon Brillouin of CEA Saclay, France, for support of this neutron diffraction research under experimental Grant No. 4142-1996.

*E-mail: isakina@ilt.kharkov.ua

---

[1] J. Michel, M. Drifford, and P. Rigny, J. Chem. Phys. **67**, 31 (1970).
[2] A. P. Isakina and A. I. Prokhvatilov, Fiz. Nizk. Temp. **19**, 201 (1993) [Low Temp. Phys. **19**, 142 (1993)].
[3] G. Dolling, B. M. Powell, and V. F. Sears, Mol. Phys. **37**, 1859 (1979).
[4] R. Raynard, G. J. Tatlock, and J. A. Venables, Acta Crystallogr. **38**, 1896 (1982).
[5] R. Raynard and J. A. Venables, Ultramicroscopy **23**, 433 (1987).
[6] L. S. Bartell, E. J. Valente, and J. C. Caillat, J. Phys. C **91**, 2498 (1987).
[7] M. T. Dove and G. S. Pawley, J. Phys. C: Solid State Physics **16**, 5969 (1983).
[8] M. T. Dove and G. S. Pawley, J. Phys. C: Solid State Physics **17**, 6531 (1984).
[9] B. M. Powell and G. Dolling, Can. J. Phys. **66**, 897 (1988).
[10] G. S. Pawley and G. W. Thomas, Phys. Rev. Lett. **48**, 410 (1982).
[11] G. S. Pawley and M. T. Dove, Chem. Phys. Lett. **99**, 45 (1983).
[12] L. S. Bartell, J. C. Caillat, and B. M. Powell, Science **236**, 1463 (1987).
[13] J. K. Cockcroft and A. N. Fitch, Z. Kristallogr. **184**, 123 (1988).
[14] J. Rodriguez-Carvajal, *Proceedings of the Satellite Meeting of the XVth Congress of International Union of Crystallography* (1986), p. 127.
[15] A. Eucken and F. Schroder, Z. Physik. Chemie **A41**, 307 (1938).
[16] B. M. Powell, M. Dove, G. S. Pawley, and L. S. Bartell, Mol. Phys. **62**, 865 (1987).
[17] W. K. Klemm and P. Henkel, Z. Anorg. Chem. **207**, 73 (1932).
[18] V. A. Konstantinov, V. G. Manzhelii, and S. A. Smirnov, Fiz. Nizk. Temp. **18**, 1190 (1992) [Sov. J. Low Temp. Phys. **18**, 902 (1992)].
[19] M. T. Dove, D. Fincham, and R. E. Hubbard, J. Mol. Graphics **4**, 79 (1986).
[20] H. Kiefte, R. Renney, and M. J. Clouter, J. Chem. Phys. **88**, 5846 (1988).
[21] J. K. Tisson and F. L. Hunt, J. Chem. Phys. **54**, 1256 (1971).
[22] J. C. Taylor and A. B. Waugh, J. Solid State Chem. **18**, 241 (1976).
[23] V. G. Manzhelii and Yu. A. Freiman (eds.), Physics of Cryocrystals, AIP Press, New York (1996).
[24] J. W. Stewart, J. Chem. Phys. **36**, 400 (1962).
[25] B. M. Powell and G. Dolling, Mol. Cryst. Liq. Cryst. **52**, 27 (1979).
[26] B. I. Verkin and A. F. Prikhot'ko (eds.), *Cryocrystals* [in Russian], Naukova Dumka, Kiev (1983).
[27] K. S. Krasnov, V. S. Timoshin, T. E. Danflova, and S. B. Khondozhko, in *Molecular Constants for Inorganic Compounds,* [in Russian], Khimiya, Leningrad (1968).
[28] S. K. Garg, J. Chem. Phys. **66**, 2517 (1977).

This article was published in English in the original Russian journal. Repoduced here with stylistic changes by the Translation Consultant.